

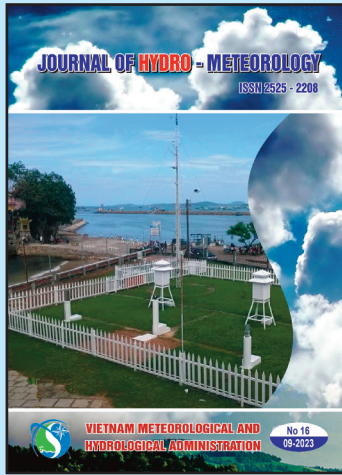
JOURNAL OF **HYDRO** - METEOROLOGY

ISSN 2525 - 2208



**VIETNAM METEOROLOGICAL AND
HYDROLOGICAL ADMINISTRATION**

No 16
09-2023



Acting Editor-in-Chief

Assoc. Prof. Dr. Doan Quang Tri

- | | |
|--------------------------------------|-----------------------------------|
| 1. Prof. Dr. Tran Hong Thai | 13. Assoc.Prof.Dr. Doan Quang Tri |
| 2. Prof. Dr. Tran Thuc | 14. Assoc.Prof.Dr. Mai Van Khiem |
| 3. Prof. Dr. Mai Trong Nhuan | 15. Assoc.Prof.Dr. Nguyen Ba Thuy |
| 4. Prof. Dr. Phan Van Tan | 16. Dr. Tong Ngoc Thanh |
| 5. Prof. Dr. Nguyen Ky Phung | 17. Dr. Dinh Thai Hung |
| 6. Prof. Dr. Phan Dinh Tuan | 18. Dr. Vo Van Hoa |
| 7. Prof. Dr. Nguyen Kim Loi | 19. TS. Nguyen Dac Dong |
| 8. Assoc. Prof. Dr. Nguyen Van Thang | 20. Prof. Dr. Kazuo Saito |
| 9. Assoc.Prof.Dr. Duong Van Kham | 21. Prof. Dr. Jun Matsumoto |
| 10. Assoc.Prof.Dr. Duong Hong Son | 22. Prof. Dr. Jaecheol Nam |
| 11. Dr. Hoang Duc Cuong | 23. Dr. Keunyoung Song |
| 12. Dr. Bach Quang Dung | 24. Dr. Lars Robert Hole |
| | 25. Dr. Sooyoul Kim |

Publishing licence

No: 166/GP-BTTTT - Ministry of Information and Communication dated 17/04/2018

Editorial office

No 8 Phao Dai Lang, Dong Da, Ha Noi
Tel: 024.39364963
Email: tapchikttv@gmail.com

Engraving and printing

Vietnam Agriculture Investment Company Limited
Tel: 0243.5624399

JOURNAL OF HYDRO-METEOROLOGY

Volume 16 - 09/2023

TABLE OF CONTENT

- 1 **Kim, T.T.; Diem, P.T.M.; Huy, N.D.Q.; Tai, P.A.; Phung, N.K.; Phung, N.K.; Bay, N.T.** A riverbank failure model: A case study for the segment of Tien River flowing through Sadec, Vietnam
- 23 **Duong, N.H.; Huyen, N.T.; Son, P.V.; Viet, T.T.; Ha, N.D.** Proposed procedure of survey and model application for forecasting flow landslide susceptibility and hazards – A case study in Tam Chung commune, Thanh Hoa Province
- 38 **Kim, T.T.; Huy, D.N.; Huy, N.D.Q.; Phuoc, N.V.; Phung, N.K.; Bay, N.T.** The barotropic simulation of coastal current in Soc Trang derived from a hydraulic model in curvilinear coordinates
- 56 **Lang, T.T.; Tan, L.V.; Tu, T.T.K.; Tuan, N.V.** Evaluation of the current status of wastewater management and treatment from super-intensive whiteleg (*Penaeus vannamei*) shrimp ponds in Ben Tre Province
- 65 **Phong, D.H.** Flood risk assessment from high tide based on principal component analysis (PCA) of Sentinel-1 satellite images sequence for Ho Chi Minh City.
- 77 **Khanh, N.T.; Tuan, N.H.; Nu, H.T.T.; Van, C.T.** Application of 2D hydro-dynamic model to simulate the suspended sediment on the Tien river, Cao Lanh district, Dong Thap Province
- 89 **Thao, N.T.P.; Minh, T.P.; Anh, M.D.** Assessment of current water quality status in clam areas in Thai Binh Province and proposal for measures to improve efficiency
- 100 **Lam, D.V.; Toan, V.D.; Phuong, T.M.** Residual and ecological risk assessment of Chlorpyrifos in coffee growing soil areas: A case study in Lam Ha district, Lam Dong Province

Research Article

A riverbank failure model: A case study for the segment of Tien River flowing through Sadec, Vietnam

Kim Tran Thi¹, Diem Phung Thi My¹, Huy Nguyen Dam Quoc², Tai Pham Anh^{3,4}, Phung Nguyen Ky¹, Bay Nguyen Thi^{3,4*}

¹ Ho Chi Minh City University of Natural resources and Environment, 236B Le Van Sy Street, Ward 1, Tan Binh District, Ho Chi Minh City; ttkim@hcmunre.edu.vn; diemptm@hcmunre.edu.vn; kyphungng@gmail.com

² Institute of Coastal and Offshore Engineering, Vietnam, 658 Vo Van Kiet, Ward 1, District 5, Ho Chi Minh City, Vietnam; damquochuy71@gmail.com

³ University of Technology Ho Chi Minh City, Vietnam, 268 Ly Thuong Kiet Street, Ward 14, District 10, Ho Chi Minh City; phamanhtai0410@gmail.com; ntbay@hcmut.edu.vn

⁴ Vietnam National University Ho Chi Minh City, Linh Trung Ward, Thu Duc District, Ho Chi Minh City, Vietnam; phamanhtai0410@gmail.com; ntbay@hcmut.edu.vn

*Correspondence: ntbay@hcmut.edu.vn; Tel.: +84–902698585

Received: 14 April 2023; Accepted: 31 May 2023; Published: 25 September 2023

Abstract: Riverbank erosion is a common occurrence in rivers worldwide, leading to significant impacts on shoreline protection and the lives of people residing in affected areas. Scientists, experts, and engineers have devoted considerable attention to study this phenomenon to better understand and predict the damage caused by riverbank failures. In the paper, we propose a mathematical model that combines bottom erosion and riverbank failure mechanisms. The model incorporates high-performance GPUs (Graphics Processing Units) to enhance its computational efficiency and capability. It utilizes a set of equations, such as the Reynolds equations, sediment transport equations, and bed load continuity equation, to simulate the dynamics of flow, sediment transport, and changes in the riverbed. Additionally, the model incorporates the calculation of riverbank failure using the rotational failure mechanism and determines the factor of safety (FS) to assess the stability of riverbanks and the bank failure (BW). If the FS value is less than 1, it indicates that the bank is prone to failure, and such instances are recorded. To evaluate the model's reliability, a case study is conducted on a specific segment of the Tien River in Sa Dec City, Dong Thap Province. This model serves as a crucial tool for socioeconomic planning and implementing effective measures to prevent and mitigate the impacts of riverbank failure in the local area.

Keywords: Bed erosion; Factor of safety; Rotational failure; River instability; Riverbank failure.

1. Introduction

The morphological development of river systems is the most common issue that occurs in all rivers around the world. There are numerous studies investigating the evolution of morphology in river systems that are disrupted by natural and artificial factors such as dam construction, channel modifications, land use changes, volcanic eruptions, etc. [1–9]. To adequately describe and predict the geomorphic responses in a fluvial system, four components of channel change should be considered: direction, magnitude, time rate, and

spatial extent. Direction refers to the direction of change, such as erosion or deposition, while magnitude relates to the size or scale of the change. Time rate refers to the speed at which changes occur, and spatial extent pertains to the area over which changes occur [10–11]. These four components are interdependent and influence each other in complex ways. For instance, the direction of change can affect the spatial extent, while the magnitude of change can impact the time rate. Therefore, it is essential to consider all four components together to develop a comprehensive understanding of channel change in a fluvial system. This understanding can then be used to make accurate predictions about future changes, such as the effects of environmental or human-induced disturbances [9–10, 12–14].

The equilibrium concept or relaxed state associated with the tendency for responses to disturbance explains the complexity of intrinsic and extrinsic mechanisms in the fluvial systems and their response [12, 15–16]. Therefore, this precludes the development of empirical or experimental approaches coupled with physical-mathematical modeling, which are expected to simulate and predict the morphological responses of fluvial systems to intrinsic and extrinsic disturbances [17].

For the 2D hydrodynamic, sediment transport, and river morphology models, several widely applied and developed models exist worldwide. Some notable examples include:

MIKE model: Developed by DHI in Denmark, this integrated model offers various tools and performs well in addressing river erosion problems [18]. Delft model (DELFT2D): Developed by Deltares in the Netherlands, this model is widely used for hydrodynamic simulations [19]. TELEMAC model: Initially developed in 1987 by Electricité de France (EDF) in collaboration with multiple research organizations, this model is widely used for hydraulic simulations [20]. SMS (Surface Water Modeling System): Developed by the Waterways Experiment Station (WES) and the Army Corps of Engineers in the United States, this model combines hydrodynamics and sediment transport simulations [21]. CCHE2D model: Developed by the author [22], this model has the capability to simulate two-dimensional hydrodynamic characteristics. SUTRENCH-2D model: Developed by the author [23], this model simulates sediment transport and bed variations under combined flow conditions. FLUVIAL 12 model: Developed by the author [24], this model is used for river flow and sediment transport simulations. Besides the mentioned models, there are also other software packages available, such as USTARS, developed by the author [25], etc. In addition, there are also several widely used software packages developed and applied in Vietnam, such as: F28 model: Developed by Le Song Giang, this is a 2D model (similar to MIKE FLOOD) that combines 1D river flow and 2D floodplain flow. It allows for the simulation of flow dynamics in both river channels and floodplains [26]; TREM model: Developed by the author [27], based on the corresponding 2D flow model by Nagata from Kyoto University, Japan. This model simulates 2D river channel deformation in a non-orthogonal curvilinear coordinate system, allowing for the determination of velocity distribution and riverbed changes in both longitudinal and transverse directions; HYDIST-GPUs model: Developed by the author [28], HYDIST-GPUs is a model capable of simulating 2D flow, sediment transport, and river morphology changes, etc.

These existing models are based on the principles of dynamic equations and continuity equations integrated in the vertical direction. However, there are still limitations in the integration of bank failure calculations within the existing software packages.

A recent approach to studying riverbank failure is using a simple dynamic risk model with time-varying covariates to develop an early warning model for bank failures, then testing the out-of-sample predictive accuracy of this model against a simpler model - the periodic probit model, such as used by US banking regulatory agencies [29]. To understand the mechanism of sudden riverbank failure, previous studies have attempted to integrate soil erosion processes and changes in riverbank geometry into the analysis of riverbank stability [30–31].

The author [32] developed a mathematical model to calculate simple bank erosion, which is integrated into the 2D Saint-Venant-Exner morphodynamic model (in the TELEMAC 2D model). The computational grid is built on a structured triangular grid and a finite element algorithm. The slope of each element in the grid is compared with the slope of the bank material. Elements with too steep slopes are determined so that the lost mass above the axis equals the increased mass below, thus ensuring mass balance. The model performance is evaluated using data from smoke tube experiments in the laboratory and the scale model of the Old Rhine.

Furthermore, the author [33] conducted a numerical modeling and field monitoring integrated study at six specific research sites in the United Kingdom. In this study, stability analysis was based on the safety factor. Pore water pressure data was calculated at each time step in the simulation and combined with observed geotechnical data to adjust the mechanical effects of roots and vegetation cover. Similarly, the author [34] conducted a stability analysis for the waste dump slope of the WCL Makardhokara-2 open cast mine in Umred, Nagpur district, Maharashtra, India. In this study, slope stability analysis was performed using seven specific finite slope stability methods including Morgenstern's method, Spencer's method, Sarma's method, Bishop's method, Janbu's method, and the conventional method using GeoSlope software for the waste dump slope in the Makardhokara area.

In this study, we propose a simple mathematical model that combines hydrodynamic, sediment transport, river morphology effects and stability analysis of riverbanks. The HYDIST-GPUs model incorporates high-performance GPUs (Graphics Processing Units) to enhance its computational capabilities. It utilizes the Reynolds equations, sediment transport equations, and bed load continuity equation to simulate various aspects of the river system, including flow behavior, sediment transport processes, and changes in the riverbed. By leveraging the power of GPUs, the model can achieve faster and more efficient calculations, enabling more detailed and accurate simulations of the river dynamics. These equations are solved numerically to determine the stability tendency and track the behavior of suspended or deposited materials [28]. Additionally, cross-sections are extracted using the rotational failure mechanism and the factor of safety (FS) to assess the stability of riverbanks and the likelihood of failure (RF module). To validate the model's accuracy, a case study is conducted on a specific segment of the Hau River in Chau Phu district, An Giang Province. The results obtained from this case study demonstrate a remarkable agreement between the calculations derived from our model and the observed measurements, indicating the model's capability to accurately predict the stability and sediment dynamics of the riverbanks.

2. Materials and Methods

2.1. Study area

The study area is the section of the Tien River passing through Sa Dec city, Dong Thap province, as illustrated in Figure 1. The section of the Tien River that flows through Sa Dec city is a typical example of a meandering river, where bank erosion has been occurring continuously over the past few decades at a rate of up to 30 meters per year, and sometimes reaching 50 meters per year [6]. The total length of the eroded bank is up to 10 kilometers and it has eroded more than 3 kilometers into the land. The bank erosion has destroyed many important structures in Dong Thap province, including roads, hospitals, schools, and government offices [6].

2.2. Material

The bathymetry data used in the model is derived from the measurements conducted in 2017 and water level (Z), discharge (Q) and suspended sediment (C) at ST5 (from June 6,

2018, to June 13, 2018) (Figure 1) as part of the project titled “Development of bank erosion numerical model basing on HPC in connection with hydraulic model and to apply for some river reaches of the Mekong River” under grant No. NĐT.28.KR/17.

The hourly water level measurements (Z) at Cao Lanh station and discharge measurements (Q) at My Thuan station from 00:00 on May 15, 2014, to 23:00 on December 31, 2017, were collected from the Southern Region Hydro-Meteorological Centre as boundary conditions for the model.

The hourly suspended sediment concentration (C) at the boundaries is extracted from the Mike 11 model of the project titled “Development of bank erosion numerical model basing on HPC in connection with hydraulic model and to apply for some river reaches of the Mekong River” under grant No. NĐT.28.KR/17.

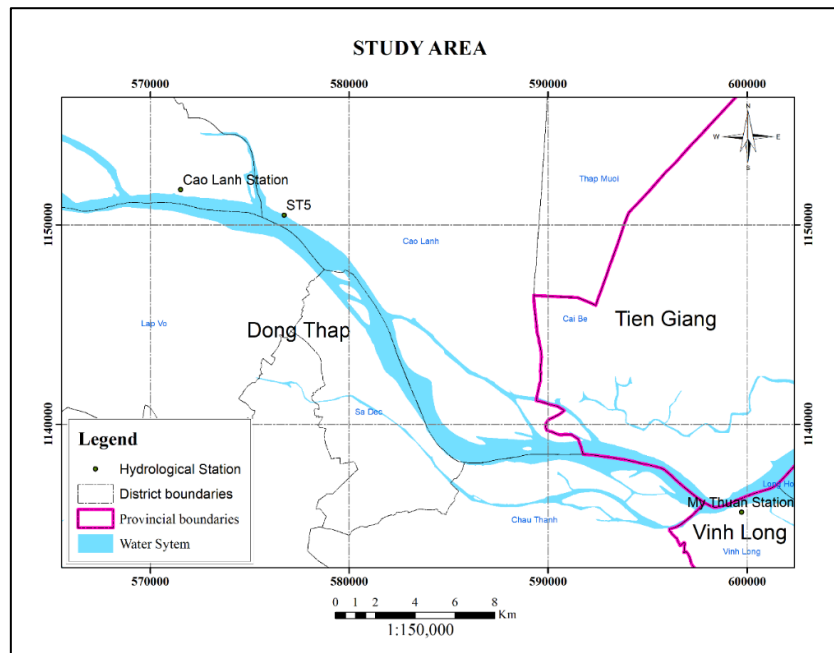


Figure 1. The section of the Tien River passes through Sa Dec city, Dong Thap province.

2.3. Method

A simple mathematical model that combines hydrodynamic, sediment transport, river morphology effects, and stability analysis of riverbanks is the HYDIST-GPUs model, which includes the integration of the RF module. The HYDIST-GPUs model is based on a set of equations, including the Reynolds equations, sediment transport equations, and bed load continuity equation [28].

2.3.1. Governing equations of the HYDIST-GPUs model

Reynolds equations:

$$\frac{\partial u}{\partial t} + u \frac{\partial u}{\partial x} + v \frac{\partial u}{\partial y} - fv = -g \frac{\partial \zeta}{\partial x} + \frac{\tau_{Sx,wind} - \tau_{Sx,w}}{\rho(h + \zeta)} - \frac{\tau_{bx}}{\rho(h + \zeta)} + A\nabla^2 \bar{u} \quad (1)$$

$$\frac{\partial v}{\partial t} + u \frac{\partial v}{\partial x} + v \frac{\partial v}{\partial y} + fu = -g \frac{\partial \zeta}{\partial y} + \frac{\tau_{Sy,wind} - \tau_{Sy,w}}{\rho(h + \zeta)} - \frac{\tau_{by}}{\rho(h + \zeta)} + A\nabla^2 \bar{v} \quad (2)$$

$$\frac{\partial \zeta}{\partial t} + \frac{\partial [(h + \zeta)u]}{\partial x} + \frac{\partial [(h + \zeta)v]}{\partial y} = 0 \quad (3)$$

where the “zero level” is set at the still water surface (Figure 2); u, v are depth-averaged horizontal velocity components in x, y direction respectively; h is static depth from the still

water surface to the bed and ζ is the water level. To simplify the simulation process for the river, we neglect the Coriolis force f and wind stress $(\tau_{Sx,wind}, \tau_{Sy,wind})$ as well as wave stress $(\tau_{Sx,w}, \tau_{Sy,w})$ in both x, y directions [28].

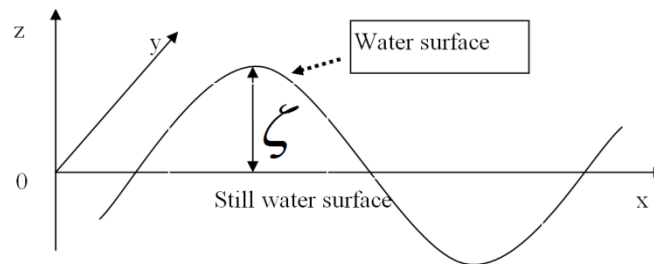


Figure 2. Initial static level.

Sediment transport equations

Due to two types of suspension: bed load and suspended load, we define the bed load having a thickness of a and at the elevation of z , hence: $-h < z < -h + a$.

The suspended load is defined in the water and at the elevation of z , where $-h + a < z < \zeta$. The minimum experimental value of a can be $0.01 H$ [35]. So, the depth-averaged mass balance equation for suspended sediment will be described as follows:

$$\frac{\partial C}{\partial t} + \gamma_v \left(u \frac{\partial C}{\partial x} + v \frac{\partial C}{\partial y} \right) = \frac{1}{H} \frac{\partial}{\partial x} \left(HK_x \frac{\partial C}{\partial x} \right) + \frac{1}{H} \frac{\partial}{\partial y} \left(HK_y \frac{\partial C}{\partial y} \right) + \frac{S}{H} \quad (4)$$

where H is the relative depth (m), and defined by static depth h and fluctuation ζ (Figure 2), $H = h + \zeta$. The quantity S describes deposition or erosion of grain ($\text{kg/m}^2\text{s}$), and can be calculated by Van Rijn’s empirical equations [35].

The bed load continuity equation can be described as the following equation.

$$\frac{\partial h}{\partial t} = \frac{1}{1 - \epsilon_p} \left[S + \frac{\partial}{\partial x} \left(HK_x \frac{\partial C}{\partial x} \right) + \frac{\partial}{\partial y} \left(HK_y \frac{\partial C}{\partial y} \right) + \frac{\partial q_{bx}}{\partial x} + \frac{\partial q_{by}}{\partial y} \right] \quad (5)$$

where q_{bx}, q_{by} , standing for the rate of bed load transport in x, y directions ($\text{m}^2/\text{s/m}$), can be determined by experimental formula [35].

$$q_b = 0.053((S - 1)g)^{0.5} d_m^{1.5} T^{2.1} D_*^{-0.3} \frac{(u, v)}{\sqrt{u^2 + v^2}} \quad (6)$$

where $q_b = (q_{bx}, q_{by})$.

3.2.2. Riverbank failure mechanism and factor of safety – RF module

The riverbank failure will be calculated on the rotational failure [36–37]. The mechanism of sliding motion illustrated in Figure 3 is explained by the fact that bank materials move to two directions: downward and outward along circular slip surface, and this is common on cohesive banks with slopes less than 60° . After failure, the upper slope of the slipped block is typically tilted inward toward the bank. Rotational failures are commonly a result of scour at the base of the bank and/or high pore-water pressure within the bank material. Normally, they will occur during rapid drawdown following high flow events.

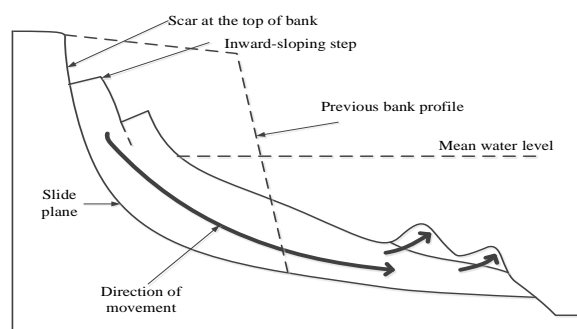


Figure 3. Mechanism of rotational failure (from Environment Agency [38]).

The critical threshold of riverbank stability can be quantified by the FS. An FS < 1 is indicative of instability and the bank failure. If FS = 1, these forces are exactly balanced. As FS increases beyond unity, the slope becomes more stable.

To determine FS, it is necessary to calculate the total forces and total moment forces acting on the sliding mass in both horizontal and vertical directions. The components used to determine the forces and moment forces include known components and unknown components. However, there are fewer known components compared to unknown components. In the model, the following assumptions are accepted:

Neglecting the interaction forces between slices when separating them into individual slices: The model uses two methods: (i) the Fellenius method (neglecting the interaction forces between slices $E = X = 0$) [39]; (ii) the Bishop method (neglecting the vertical component $X = 0$) [40].

The interaction path-locus of the point of application of the interaction force: The model uses the general Janbu method and the simplified Janbu method [41].

The inclination angle of the interaction force: The model uses the Spencer and the General Limit Equilibrium (GLE) methods [42].

These assumptions are made to simplify the analysis and calculation process. While they may introduce some limitations, they allow for the estimation of the factor of safety and provide valuable insights into the stability of the analyzed slope.

The FS includes two independent factor of safety equations; one with respect to moment equilibrium and the other with respect to horizontal force equilibrium.

When only moment equilibrium (F_m) is satisfied, the factor of safety equation is:

$$F_m = \frac{\sum(c'\beta R + (N - u\beta)R \tan\phi)}{\sum W_x - \sum Nf + \sum kW_e \pm \sum Dd \pm \sum Aa} \quad (7)$$

The factor of safety equation with respect to horizontal force equilibrium (F_f) is:

$$F_f = \frac{\sum(c'\beta \cos\alpha + (N - u\beta) \tan\phi \cos\alpha)}{\sum N \sin\alpha + \sum kW_e - \sum D \cos\omega \pm \sum A} \quad (8)$$

where F_m is the moment equilibrium factor of safety; F_f is the force equilibrium factor of safety; W is the slice weight with width b and height h [kN]; N is the slice base normal force [kN]; D is the concentrated point load [kN]; kW is the horizontal seismic load acting through the center of gravity of each slide [kN]; R is the radius of the circular slide (or the arm of the shear force moves for any shape of the slide) [m]; A is the resultant force of water pressure acting on the bank [kN]; f is the distance from center of rotation to direction of normal force N [m]; x is the horizontal distance from center of gravity of each slide to center of rotation or center of moment [m]; e is the vertical distance from the center of each slide to the center of rotation or center of moment [m]; d is the perpendicular distance from load line to center of rotation or center of moment [m]; a is the perpendicular distance from the external water force to the center of rotation or center of moment [m]; ω is the angle of inclination of the force direction relative to the horizontal (determined in the same direction); α is the angle between the tangent at the base and the horizontal [degrees]. Sign convention: when the slip angle is in the same direction as the overall slide of the figure, α is positive and vice versa; ϕ is the effective angle of friction [degree]; u is the pore-water pressure [kPa]; c' is the effective cohesion [kPa]; β is the length of the sliding arc of the earth column [m].

The normal force at the base of the soil column is determined by summing the vertical forces acting on each soil column. To do this, we need to know the weight forces of each soil column ((9), as well as the other vertical forces acting on them.

$$N = \frac{W + (X_R - X_L) - \frac{c'\beta \sin\alpha + u\beta \sin\alpha \tan\phi}{F} + D \sin\omega}{\cos\alpha + \frac{\sin\alpha \tan\phi}{F}} \quad (9)$$

where: In the moment factor of safety equation, F is equal to F_m when N is substituted, indicating the moment resistance. On the other hand, in the force factor of safety equation, F is equal to F_f when N is substituted, representing the force resistance.

3.2.3. Simulation process

The integration of the riverbank failure module with the HYDIST-GPUs model, referred to as HYDIST-GPUs-RF, involves a sequence of steps in the simulation process. The steps are outlined as follows:

a) Discretization of the riverbank section

The section of the riverbank where there is a risk of erosion (simulated from the model) will be discretized into smaller segments by cross-sectional perpendicular to the riverbank. For each cross-section, the model will calculate the safety factor FS to identify the segments of the bank that are prone to erosion. Figure 4 illustrates the process of discretizing the riverbank section for the purpose of simulating bank erosion.

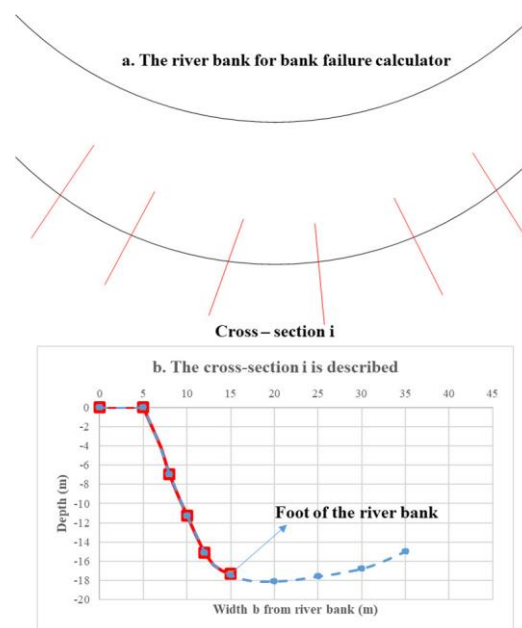


Figure 4. The process of discretizing the riverbank section for the purpose of simulating bank erosion.

The density of the cross-sections along the riverbank segment depends on the level of erosion risk, and in cases where there is low risk of erosion, the cross-sections will be spaced further apart. After calculating the safety factor of each cross-section, the degree of erosion will be calculated to determine the extent of bank collapse at that cross-section. The degree of erosion at any location between two cross-sections in the calculation area will be interpolated between the two cross-sections (using a linear interpolation method in the model).

b) Simulating the bank failure

After calculating the safety factor FS for each cross-section, if $FS \geq FS_{critical}$, then the bank slope at that cross-section is stable (not eroding), but if $FS < FS_{critical}$, then the bank slope at that cross-section is unstable and will erode. At this point, the direction of the bank slope will collapse inward with a width of BW . The value of BW (predicted width of bank collapse) at the i -th cross-section is compared with Δ ($\Delta = \sqrt{(\Delta x)^2 + (\Delta y)^2}$) to update the grid cell adjacent to the bank position at cross-section i , if $BW < \Delta$, then the characteristics of the bank cell are still preserved, and the hydraulic-erosion model continues to use the old topography for calculations until $BW \geq \Delta$. At this point, the bank cell will collapse and be converted into a fluid cell in the hydrodynamic flow problem. The comparison between BW and Δ is detailed in Table 1.

Table 1. Cases in which the bank plots are collapsed in the vertical direction i.

Cases	The number of cell–bank subsidence
$0 < BW < \Delta$	No falling
$\Delta \leq BW < 2\Delta$	1 cell
$2\Delta \leq BW < 3\Delta$	2 cells
$3\Delta \leq BW < 4\Delta$	
...	These cases are the same as above

For the positions of the bank cells located between two calculated cross sections i and $i+1$, the model also examines similarly to determine whether to convert those cells into liquefied cells or keep them as they are using the method above, with BW at each position determined by linear interpolation from the BW of cross sections i and $i+1$.

c) Bathymetry update

The section of land that has collapsed will slide down to the foot of the bank, causing changes in the depth values at this location (the top of the bank, the slope of the bank, and the foot of the bank). These changes need to be calculated to update the depth map for the next calculation of the dynamic hydraulics and sedimentation problem. The bank cells and slope cells will have a decreased bed elevation (increased depth). At the foot of the bank, sediment will be deposited, causing the bed elevation to increase (decreased depth). The extent of the bed elevation changes for each cell is calculated such that the volume of soil loss is equal to the volume of sediment deposited at the foot of the bank. Choose a cross-sectional view to explain this calculation. The cross-sectional view has been discretized into grid cells with the same size as the flow field discretization. Figure 5 depicts a cross-sectional view of a riverbank after discretization, with grid cells of size Δx .

The simulation results will give the parameters of the sliding arc radius and the center position O , from which the starting and ending points of the sliding arc can be determined to find the positions of the grid cells that need to be updated for the bottom topography (such as cells 2 to 6 in Figure 5).

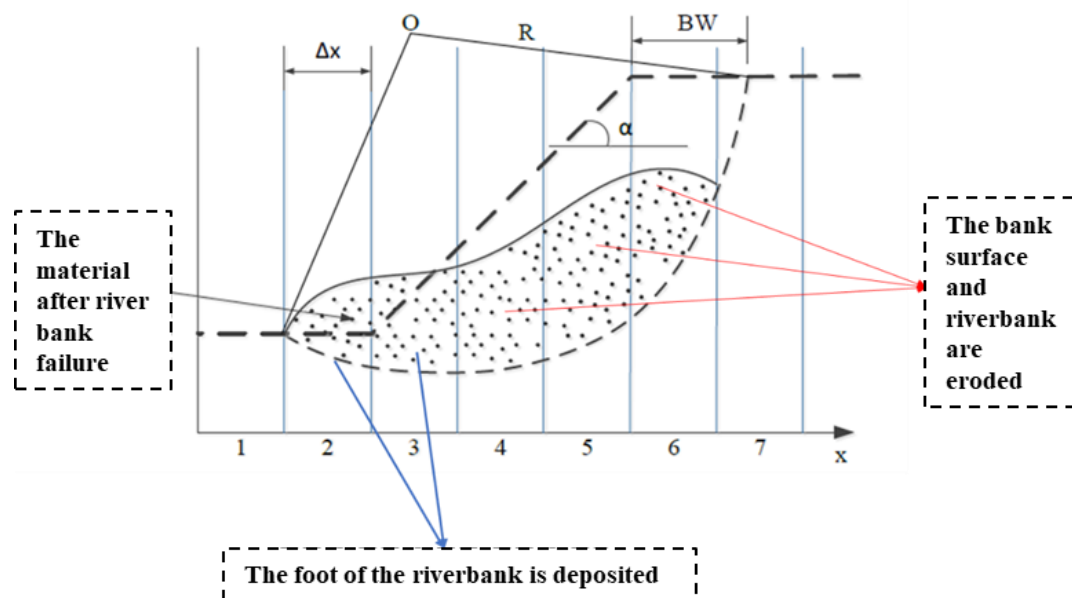


Figure 5. Riverbank cross-section before and after subsidence.

d) F_s safety factor

The general calculation scheme for bank erosion in the HYDIST-GPUs-RF model is presented in detail in Figure 6a, in which the steps for the safety factor in the bank erosion model are specifically presented in Figure 6b. When $F_m = F_f$, the factor of safety is calculated

as $FS = F_m$ or F_f . The sequence for calculating the safety factor F_s will be programmed using Python (suitable for GPUs) as the RF module to perform automatic calculations [28]. Then, the RF module will be integrated with the HYDIST-GPUs model to calculate the hydrodynamic process.

The diagram below illustrates the calculation process using two methods, Sarma and GLE. It is easy to see that the only difference between the two methods is the formula for the relationship between shear force (X) and normal force (E). Shear force and normal force at each cross-section on both sides will be distinguished by the symbols X_L, X_R, E_L , and E_R .

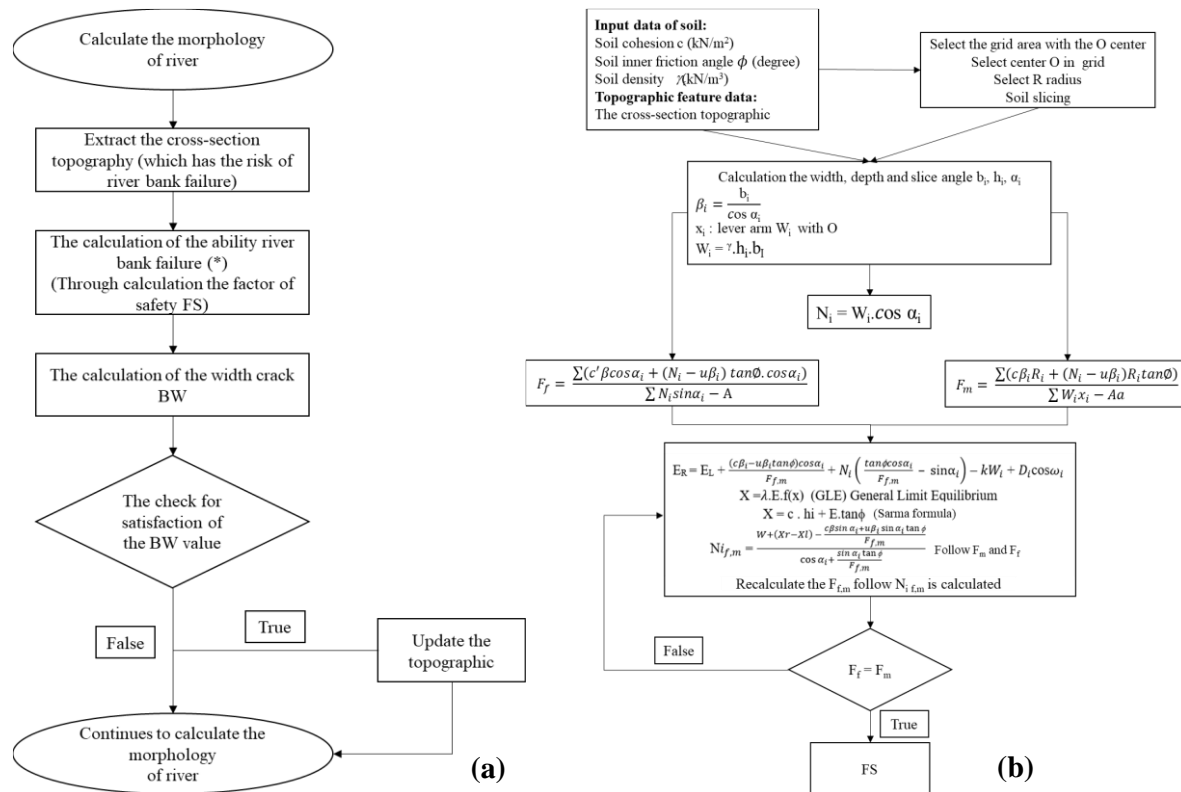


Figure 6. (a) HYDIST-GPUs-RF scheme; (b) FS scheme (*).

3. Results

3.1. Theory solution

The simplest form of the Ordinary factor of safety equation in the absence of any pore-water pressures for a circular slip surface is:

$$FS = \frac{\sum [c\beta + N \tan \phi]}{\sum w \sin \alpha} = \frac{\sum S_{\text{resistance}}}{\sum S_{\text{mobilized}}} \tag{10}$$

where c is the cohesion; N is the base normal ($W \cos \alpha$).

The ordinary factor of safety can be fairly easily computed using a spreadsheet. Using a spreadsheet is of course not necessary when you have HYDIST-GPUs-RF, but doing a simple manual analysis periodically is a useful learning exercise.

Consider the simple problem in Figure 7. There are 14 slices numbered from left to right. The cohesive strength is 5 kPa and the soil friction angle ϕ is 20 degrees.

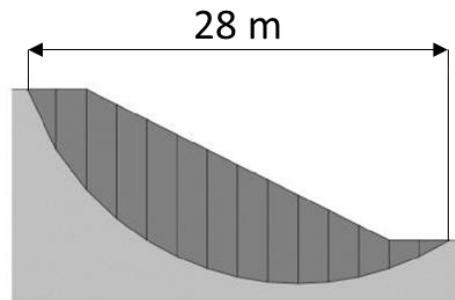


Figure 7. Case for hand-calculations.

Table 2 illustrates how the ordinary factor of safety can be easily calculated. The most difficult part is specifying the slice dimensions.

Table 2. The ordinary factor of safety.

Slice #	Width (m)	Mid-height (m)	Weight (kN)	Alpha (degrees)	β (m)
1	2	2.3	86.9	64.7	4.42
2	2	5.4	217.8	52.9	3.32
3	2	7.2	287	43.7	2.77
4	2	7.8	313.2	35.8	2.46
5	2	8.1	323.3	28.5	2.28
6	2	8	320.9	21.8	2.15
7	2	7.7	307.7	15.4	2.07
8	2	7.1	285.1	9.2	2.03
9	2	6.3	253.7	3	2
10	2	5.3	213.7	-3	2
11	2	4.1	165.1	-9.2	2.03
12	2	2.7	107.7	-15.4	2.07
13	2	1.5	60.9	-21.8	2.15
14	2	0.6	23.3	-28.5	2.28

The factor of safety can be computed to be:

$$FS = \frac{\sum [c\beta + N \tan \phi]}{\sum w \sin \alpha} = \frac{1116.75}{947.93} = 1.18 \tag{11}$$

HYDIST-GPUs-RF gives the same factor of safety as shown in Figure 8.

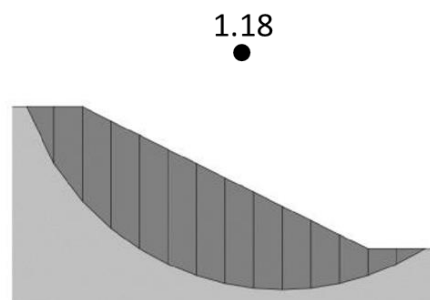


Figure 8. HYDIST-GPUs-RF computed ordinary factor of safety.

3.2. A case study for riverbank stability and riverbed erosion of Tien River (flowing Sa Dec city)

The occurrence of river bank erosion in Sa Dec has had severe consequences on bank protection structures and the lives of the local population. The erosion of riverbanks has compromised the effectiveness of protective measures, such as levees, revetments, or other bank defenses, that are crucial for safeguarding the area against the erosive forces of the river [43–44]. This erosion has resulted in the loss of land, damage to infrastructure, and potential threats to residential areas and livelihoods. The local community is directly affected by the negative impacts, including increased vulnerability to flooding, loss of agricultural land, and potential displacement of residents. Addressing and mitigating the impacts of river bank erosion in Sa Dec is of utmost importance to protect both the physical infrastructure and the well-being of the people living in the area.

In 2013, to prevent bank erosion, protect and stabilize the living environment for local residents, as well as contribute to the socio-economic development of the region, the provincial People's Committee built a system of revetments consisting of 7 sections, stretching about 4.5 kilometers from Cai Doi stream to Ong Tuan stream. The sedimentation and erosion processes in this area are relatively balanced. The concave bank on the right of the Tien River belongs to Ward 10 in Sa Dec city and An Hiep commune in Chau Thanh district, where bank erosion has been particularly strong. Although a system of revetments had been constructed in Ward 10 - Sa Dec, the distance between the revetments was not reasonable, so bank erosion still occurred at the foot of the revetments and in the areas between them. In March 2015, a serious bank erosion incident occurred at revetment section 7, causing many households to be urgently evacuated. Moreover, due to limited funding, only a section of the revetment system was constructed, while bank erosion in the area behind the revetment system in An Hiep commune - Chau Thanh district continues to occur continuously.

3.2.1. Mesh in HYDIST-GPUs

The research area is the section of the Tien River passing through Sa Dec city, divided into a grid of 484 rows and 629 columns, with a spacing of $dx = dy = 20$ m (Figure 9).

Number of rows = 484; Number of columns = 629; Total number of grid elements is $304,436 = 484 \times 629$; Maximum depth of the grid is $h = 40.96$ m.

Spatial step of the grid in the x-direction is $\Delta x = 20$ m, in the y-direction is $\Delta y = 20$ m, and the time step is $\Delta t = 2$ s.

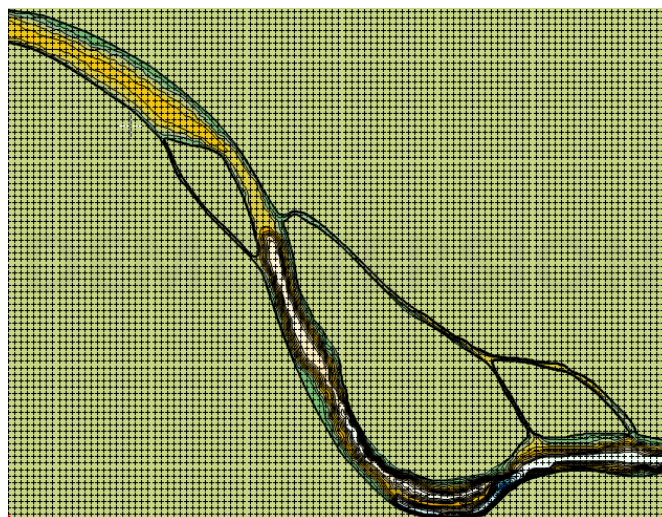


Figure 9. The depth map of the Tien River flowing Sa Dec with a 20-meter spacing.

3.2.2. Initial conditions and boundaries

For hydraulic model:

(1) Initial conditions: In the model, if we start the calculation from $t_0 = 0$, the hydraulic problem is initialized with a steady-state condition throughout the domain. In the case where the problem is continued from a specific time $t = t_1$, the initial conditions will be the velocity fields $u, v(x, y)$ at time t_1 across the entire computational domain.

(2) Boundary conditions:

Open boundaries: The first open boundary (B1) is determined by the measured water level value Z at the Cao Lanh station, which is shifted 8 hours ahead in the downstream direction.

The second open boundary (B2) is determined by the measured discharge value Q at the My Thuan station.

Both open boundaries are considered from 00:00 on May 15, 2014, to 23:00 on December 31, 2017.

Land boundaries: $u_n = 0$.

For sediment transport model:

(1) Initial conditions:

In the model, if the calculation starts from $t_0 = 0$, the sediment transport problem is initialized with a constant background concentration. In the case where the problem is continued from a specific time $t = t_1$, the initial condition will be the sediment concentration $C(x, y)$ at time t_1 throughout the computational domain.

(2) Boundary conditions:

Open boundaries: The suspended sediment concentration (C) at the boundaries is extracted from the Mike 11 model. However, the right boundary of the model does not utilize the characteristics of suspended sediment because this is where the water flows out of the computational domain. At this boundary, the model has used the method of characteristic lines to track the deposition of suspended sediment along the outflow. Both open boundaries are calculated from 15:00 on May 15, 2014, to 19:00 on December 31, 2014.

Land boundaries: $\frac{\partial C}{\partial n} = 0$, the variable “n” represents the normal direction perpendicular to the bank.

3.2.3. Calibration and validation

Calibration and validation of the hydraulic model

The results of discharge and water level calculations from the model at My Thuan in June 2014 compared to the accurately measured values are quite good. The NSE and R^2 values for water level calibration are high (0.98 and 0.96), indicating a good fit. Similarly, the NSE and R^2 values for discharge calibration are 0.97 and 0.93, respectively, indicating a good fit as well. It should be emphasized that the Sa Dec section, from the upper to lower reach, is a relatively

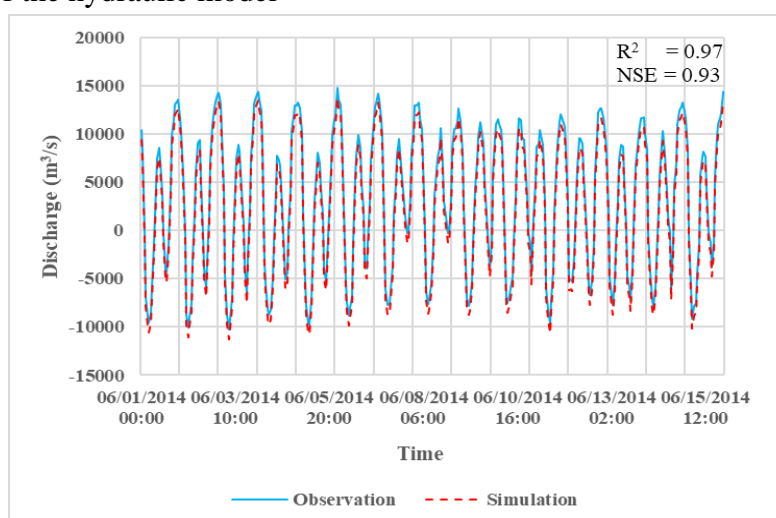


Figure 10. The calibration results of the discharge between the measured and calculated data from June 1, 2014, to June 15, 2014.

short section where flow is well-conserved, which contributes to the good flow calibration results (Figures 10–11).

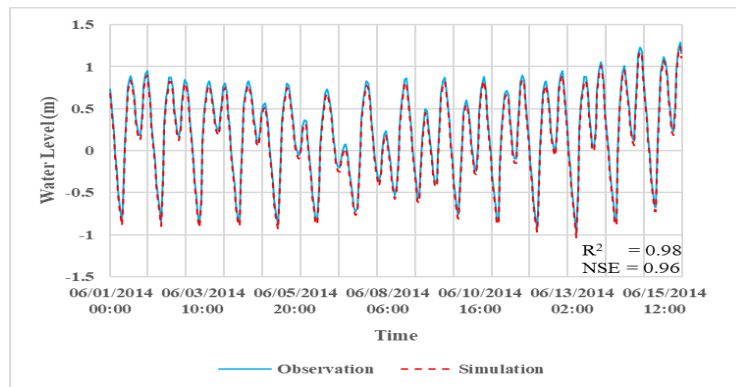


Figure 11. The calibration results of the water level between the measured and calculated data from June 1, 2014, to June 15, 2014.

To validate the hydraulic model, the calibrated parameter set mentioned above is used, and the calculation time is adjusted. The validation period is from 10:00 on June 6, 2018, to 10:00 on June 13, 2018. The water level and discharge data measured at the ST5 measurement stations during the supplementary survey are utilized (Refer to the location of ST5 in Figure 1).

The computed NSE and R^2 values at ST5 for water level are 0.9 and 0.89, respectively, while for discharge, they are 0.89 and 0.85. The comparison results at ST5 from June 6, 2018, to June 13, 2018, are presented in Figures 12-13.

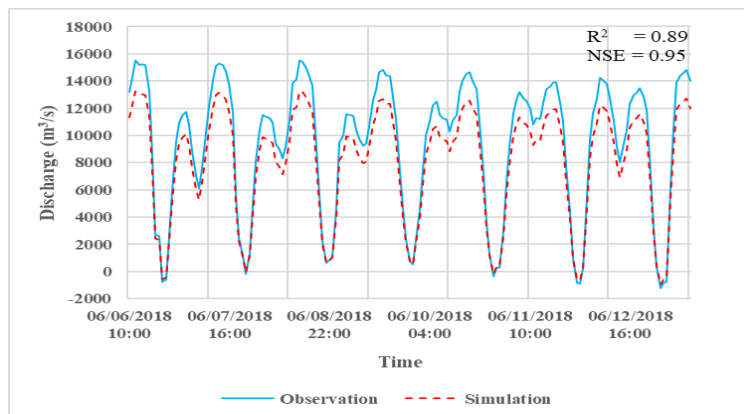


Figure 12. The comparison results between the measured and computed discharge at station ST5 from June 6, 2018, to June 13, 2018.

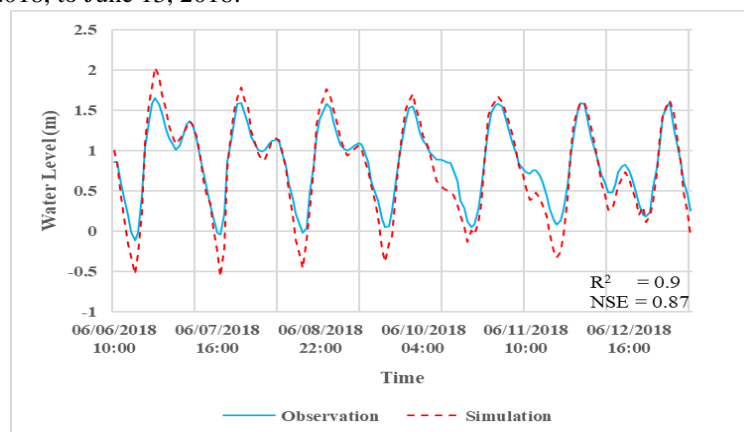


Figure 13. The comparison results between the measured and computed water level at station ST5 from June 6, 2018, to June 13, 2018.

Calibration and validation of the sediment transport model

The sediment deposition calibration process was carried out in June 2014. The results showed that the NSE and R^2 values for sediment deposition calibration were 0.74 and 0.89, respectively. Sediment concentration is a common parameter that is difficult to calibrate in sediment transport models, so the achieved calibration results can be considered quite good. The comparison between the calculated and measured sediment deposition for the calibration is presented in Figure 14.

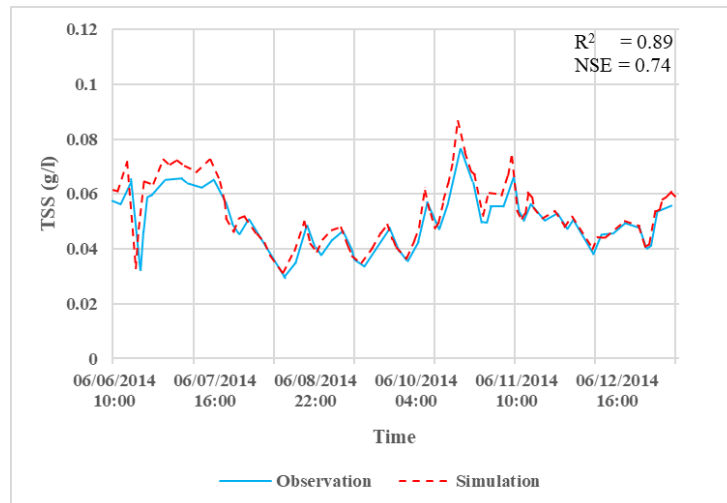


Figure 14. The calibrated results of suspended sediment between measurements and calculations from June 1, 2014, to June 15, 2014.

The parameter sets for the sediment transport model are extracted as shown in Table 3.

Table 3. The parameters in the sediment transport model.

Parameter	Value
Time step (Δt)	2 s
The mean diameter of particles. (D)	0.01 mm
The diameter of particles 90% (D_{90})	0.04 mm
Density (ρ_s)	2600 kg/m ³
Dynamic viscosity coefficient (ν)	1.01x10 ⁻⁶ m ² /s

The maps of the critical stresses of erosion (τ_e) and the critical stresses of deposition (τ_d) in the HYDIST-GPUs model were tested against the Sa Dec region and range from 0.2–0.35 N/m² (τ_e) and 0.03–0.06 N/m² (τ_d) (Figure 15).

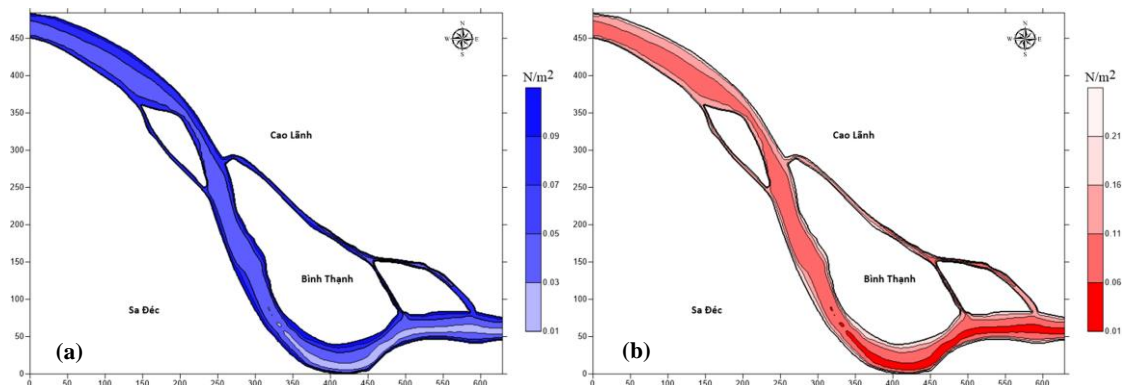


Figure 15. The maps: (a) The critical stresses of deposition τ_d ; (b) The critical stresses of erosion τ_e in the Sa Dec region.

The model validation for sediment transport is conducted from 10:00 on June 6, 2018, to 10:00 on June 13, 2018, based on the suspended sediment concentration at the ST5.

After obtaining the characteristic parameters for the sediment transport model for the entire computational domain, sediment transport calculations are performed until 2018. Subsequently, the computed suspended sediment concentration results from 10:00 on June 6, 2018, to 10:00 on June 13, 2018, at station ST5 are compared with the measured data. The NSE and R^2 values obtained during the validation process are quite good (0.74 for NSE and 0.89 for R^2). The comparison results between the computed and measured sediment transport are presented in Figure 16.

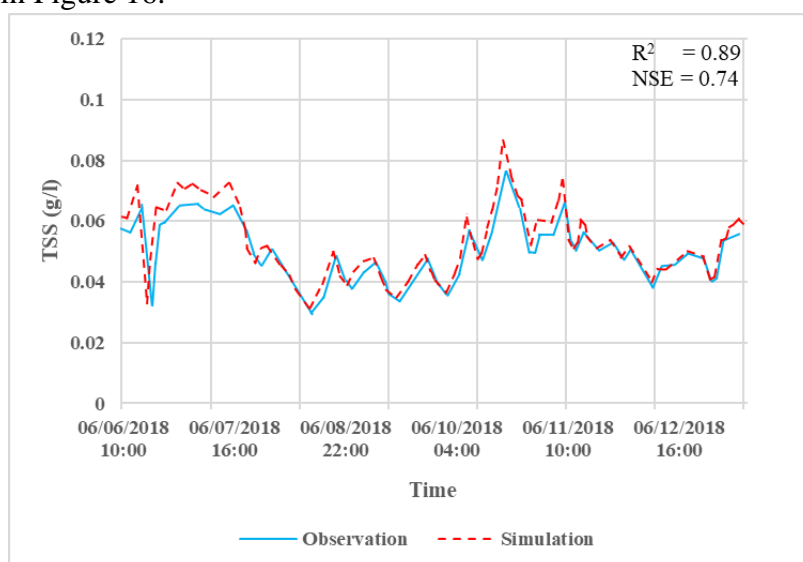


Figure 16. The validation results of sediment transport between the measured and computed data from June 6, 2018, to June 13, 2018.

3.2.4. Calculation of bank failure

The simulation of the bank failure rate of the section of the Tien River flowing through Sa Dec was carried out in 2015 and 2017. The parameter set of the model was established as shown in Table 4.

According to the theory of bank erosion, bank failure is expected to occur when FS value is less than 1. However, based on a study conducted by [45], it was observed that bank erosion starts to happen when the FS value is greater than 1.119. Therefore, for the specific case of Sa Dec, the calculations for bank erosion will consider FS values below 1.119 as indicative of bank erosion occurrence.

Table 4. The parameters of the model for bank erosion in Sa Dec.

Parameter		Value
Parameter settings	Critical FS	1.119
	The maximum distance between 2 points on a cross section (m)	0.23
	The number of points on a calculated cross section	100
	The number of sections for the calculated segment	65
	Tolerance	0.19
Soil parameters	fx Function	sin()
	The effective cohesion c (kN/m ²)	32
	The effective angle of friction ϕ (degree)	30
	Specific gravity of soil γ (kN/m ³)	19

	Parameter	Value
Simulation	The pore–water pressure u (kPa)	15
parameters	The horizontal seismic load kW (kN/m)	15

The simulation results from the bank erosion model in Sa Dec also include: the distribution of the safety factor FS and the width of the corresponding crack width BW for each longitudinal cross section along the riverbank. The bank erosion results are only calculated for the curved section of the riverbank on the side of Sa Dec city, with 65 cross sections as described in Figure 16.

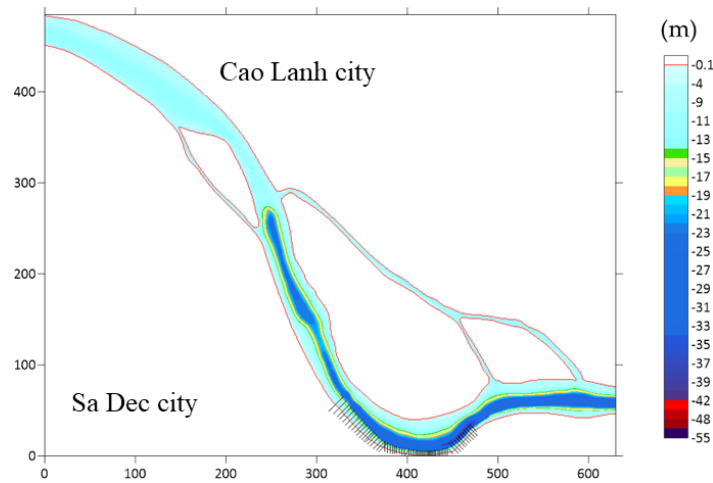


Figure 16. The cross-section of Tien River flowing Sa Dec City.

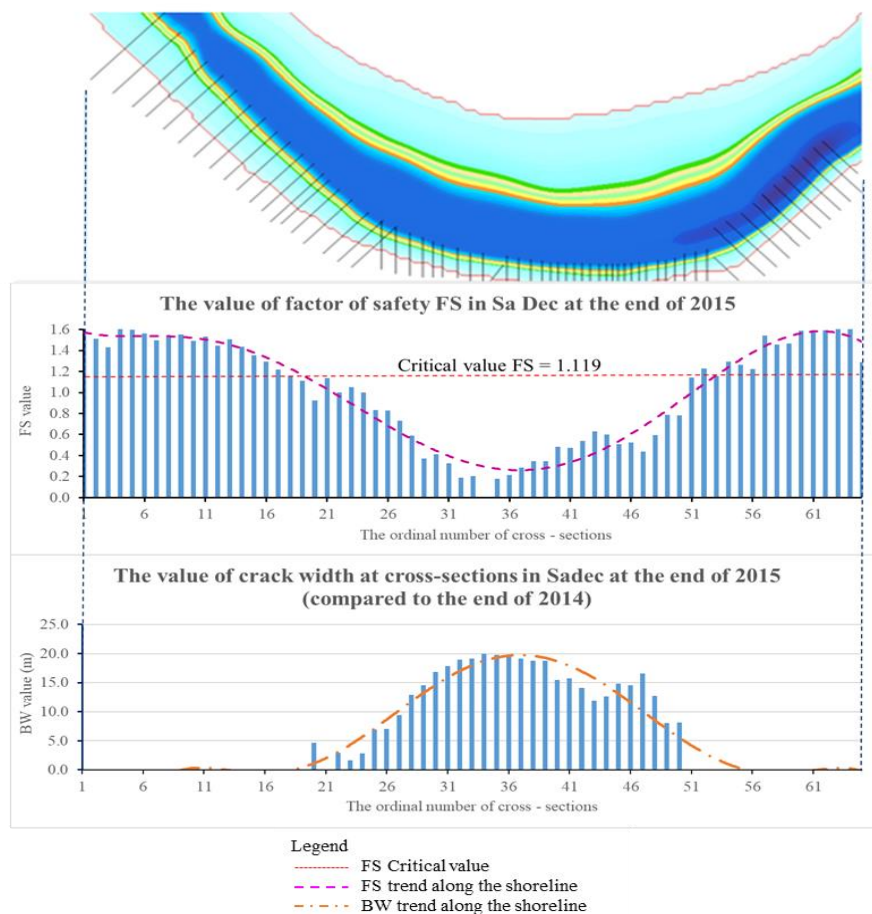


Figure 17. Simulation results of FS and BW coefficients along the riverbank of Sa Dec section in 2015.

The calculation results in 2015 showed that: in the curved section from cross section 19 to cross section 51, the result of $FS = 0.18 \div 1.11$ was less than the limit safety factor (limit $FS = 1.119$) (Figure 17). The sections before and after the curved section were more stable (with FS greater than the limit FS), with calculated FS ranging from 1.12 to 1.58 (Figure 17). In this section, although 7 rock revetments had been built (with a distance of about 50m between two revetments), the erosion process still occurred between two revetments.

The trend of variation of FS and BW along the curved section were also opposite to each other (Figure 18), at cross section 34 (the most curved section of the river), the BW in 2015 reached a value of 20m corresponding to a very low value of FS . Some selected cross sections (26, 34, and 44) in Figure 18 were extracted for further analysis.

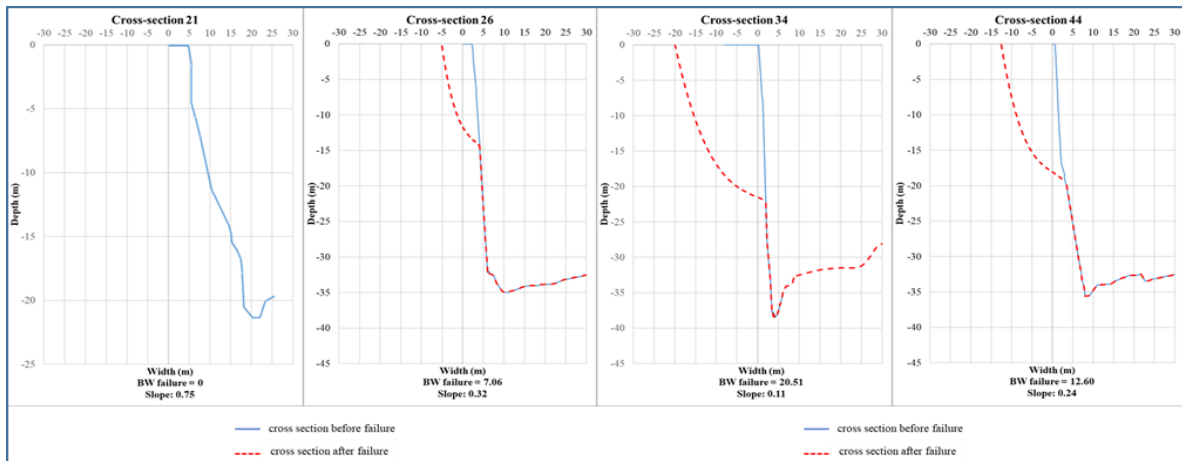


Figure 18. The results of bank erosion at sections 21, 26, 34 and 44 in 2015.

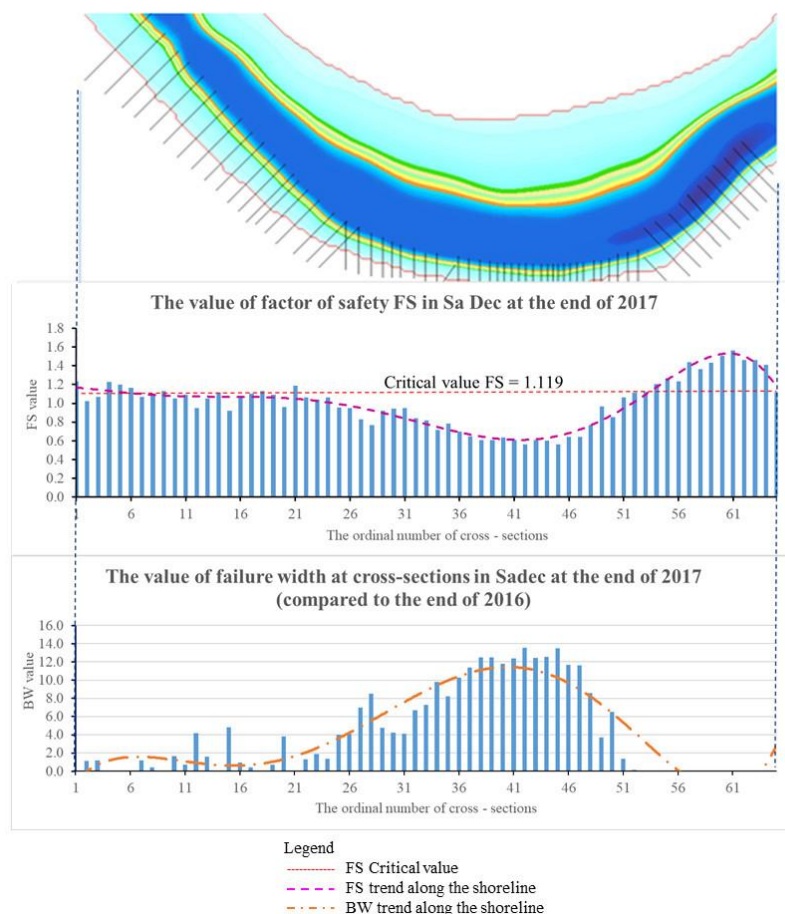


Figure 19. The results of FS and BW coefficients along the riverbank of Sa Dec section in 2017.

By 2017, the riverbank on the Sa Dec side showed a relatively similar trend to that of 2015, with intermittent erosion. The sections after the curved section exhibited higher stability, with FS values exceeding the critical FS. The calculated FS values in these sections ranged from 1.12 to 1.56. However, the sections before the curved section was less stable, as indicated by the FS. Both the FS values before the curved section and in the curved section are less than 1.119. Figure 19 presents the calculation results of FS and BW along the Sa Dec riverbank in 2017. The results indicated that the riverbanks are less stable. Specifically, the section in communes 3,4 Sa Dec (the sections before the curved section) had an FS value lower than 1.119, indicating a high risk of bank failure. The calculation results for the BW at cross-section 26 was approximately 4.14 m, at cross-section 34 was 9.78 m, and at cross-section 44 was 12.6 m (Figure 20).

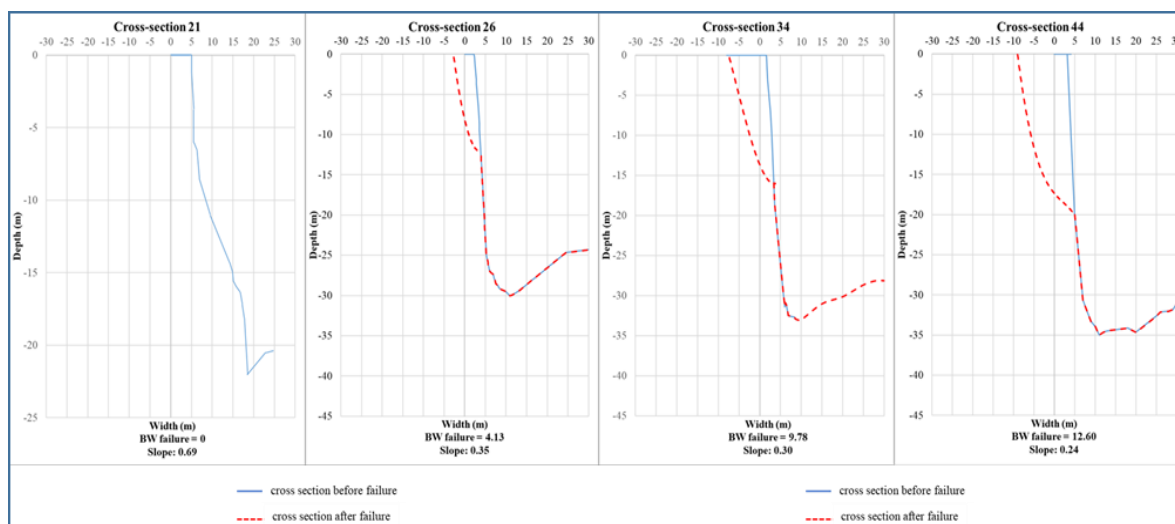


Figure 20. The results of bank erosion at sections 21 and 26 (a) 34 and 44 (b) in 2017.

4. Discussions

The statistics of the slope coefficient and crack width of the cross sections in the two calculation years are presented in Table 5.

Table 5. Statistics of slope coefficient and crack width of cross sections in 2015 and 2017 at some cross-sections (21, 26, 34 and 44).

Cross-sections	21		26		34		44	
Years	2015	2017	2015	2017	2015	2017	2015	2017
Slopes	0.75	0.69	0.32	0.35	0.115	0.3	0.24	0.24
Failure Width (BW m)	0	0	7.1	4.14	20.5	9.78	12.6	12.6

According to the calculation results, it is observed that the potential for bank failure occurs before and in the curved arc sections. The high potential for bank failure occurred between cross-section 34 and cross-section 44, with corresponding BW of 15.5 m and 12.6 m in 2015. By 2017, the BW at these two cross-sections corresponded to 9.78 m and 12.6 m.

The calculated BW at cross-sections 21, 26, 34, and 44 in 2017 was lower than in 2015. At cross-section 26, the bank erosion potential in 2015 was 7.1 m, but by 2017, it decreased to 4.14 m. However, the cross-sections before the curved section show significantly greater signs of instability compared to 2015. These calculated results align well with the forecasted results from the study by Dinh Cong San for commune 3,4, Sa Dec (erosion ranging from 5–8 m) [46].

The Sa Dec riverbank started to erode when the slope of the bank was relatively steep (the slope coefficient of the bank was quite small) as recorded in Table 5, where cross-section 21 was not eroded (FS coefficient here was about 1.11, and the maximum slope coefficient of the bank was accepted at 0.69. Compared to the bank slope coefficient in Tan Chau, the maximum slope of the bank here was steeper. This is also consistent with reality because the cohesion force of the soil in Sa Dec (32 kN/m^2) is larger than that in Tan Chau (24 kN/m^2). In the Sa Dec bank survey, it was found that the vegetation cover was more extensive than on the An Giang bank opposite to Chinh Sach islet. In the model, the cohesion factor of the soil due to plant roots was also included in the cohesion force. The results from the HYDIST-GPUs-RF model for the Tien River section flowing through Sa Dec City indicate that the section with the most significant erosion is located in An Hiep Commune [28]. This is relatively accurate compared to the result obtained from the calculation of the bank line change using remote sensing [6]. The maximum distance between the bank line before and after 10 years (2009–2019) is 279 meters [47].

5. Conclusions

The simulations from the HYDIST-GPUs-RF model are quite consistent with those from the GEOSLOPE software. Slope stability calculations are very detailed and carried out for each cross-section. To save time and effort, the slope calculation is not performed for the entire length of the riverbank. Based on the calculation results of the dynamic hydraulic model, each small section of the bank that is at risk of erosion (i.e. those sections with significant depth loss based on the calculation) will be identified, and only those sections will be included in the HYDIST-GPUs-RF model for slope simulation and then the bathymetry will be updated. However, currently, the sections are not automatically cut. These limitations are expected to be addressed and improved in future developments.

The model was tested on some sections of the Tien River passing through Tan Chau Town in An Giang Province and Sa Dec City. The results of the simulated river morphology in different years are quite consistent with the actual morphology of the area (based on the comparison with remote sensing analysis and observations). The results show that for the geological structure of this section of the Tien River, the stability level of the bank corresponded to a limit factor of safety of 1.119. The model is not only applicable for calculating river morphology in the Mekong Delta region but can also be used to calculate the morphology and erosion of any other river section in Vietnam. However, the parameters in the model need to be adjusted to fit each region. The calculation results also depend heavily on the reliability of the input data. Therefore, to successfully apply the HYDIST-GPUs model in calculating river morphology, the first important step is to conduct a thorough survey, collect long-term (multi-year) and supplementary measurement data for the region.

Author Contributions: Conceptualization, T.T.K., N.T.B.; methodology, T.T.K., P.A.T., N.T.B., N.K.P.; software, T.T.K., N.D.Q.H., P.T.M.D., P.A.T.; validation, P.T.M.D.; formal analysis, T.T.K., P.T.M.D., N.D.Q.H.; investigation, N.T.B., N.K.P.; resources, N.T.B.; data curation, N.D.Q.H., N.T.B.; writing—original draft preparation, T.T.K., N.T.B.; writing—review and editing, T.T.K., N.T.B.; visualization, P.A.T., N.D.Q.H.; supervision, N.K.P., N.T.B.; project administration, N.K.P.; funding acquisition, N.K.P.

Funding: We would like to thank Ho Chi Minh City University of Technology (HCMUT), VNU-HCM, for the support of time and facilities for this study.

Conflicts of Interest: The authors declare no conflict of interest.

References

1. Agnihotri, A.K.; Ohri, A.; Mishra, S. Channel planform dynamics of lower Ramganga River, Ganga basin, GIS and remote sensing analyses. *Geocarto Int.* **2020**, *35*(9), 934–953.

2. Church, M.; Ferguson, R. Morphodynamics: Rivers beyond steady state. *Water Resour. Res.* **2015**, *51*(4), 1883–1897.
3. Das, T.K.; Haldar, S.K.; Gupta, I.D.; Sen, S. River bank erosion induced human displacement and its consequences. *Living Rev. Landscape Res.* **2014**, *8*(3), 1–35.
4. Duc, N.A.; Nguyen, L.T.; Thai, T.H.; Khan, A.; Rautenstrauch, K.; Schmidt, C. Assessing cumulative impacts of the proposed Lower Mekong Basin hydropower cascade on the Mekong River floodplains and Delta—Overview of integrated modeling methods and results. *J. Hydrol.* **2020**, *581*, 122511.
5. Hasanuzzaman, M.; Gayen, A.; Shit, P.K. Channel dynamics and geomorphological adjustments of Kaljani River in Himalayan foothills. *Geocarto Int.* **2022**, *37*(16), 4687–4713.
6. Khoi, D.N.; Dang, T.D.; Pham, L.T.; Loi, P.T.; Thuy, N.T.D.; Phung, N.K.; Bay, N.T. Morphological change assessment from intertidal to river-dominated zones using multiple-satellite imagery: A case study of the Vietnamese Mekong Delta. *Reg. Stud. Mar. Sci.* **2020**, *34*, 101087.
7. Kondolf, G.M.; Schmitt, R.J.; Carling, P.; Darby, S.; Arias, M.; Bizzi, S.; Castelletti, A.; Cochran, T.A.; Gibson, S.; Kumm, M.; Oeuring, C.; Rubin, Z.; Wild, T. Changing sediment budget of the Mekong: Cumulative threats and management strategies for a large river basin. *Sci. Total. Environ.* **2018**, *625*, 114–134.
8. Tran, D.D.; van Halsema, G.; Hellegers, P.J.; Hoang, L.P.; Ludwig, F. Long-term sustainability of the Vietnamese Mekong Delta in question: An economic assessment of water management alternatives. *Agric. Water. Manage.* **2019**, *223*, 105703.
9. Van, B.D.; Kantoush, S.; Sumi, T. Changes to long-term discharge and sediment loads in the Vietnamese Mekong Delta caused by upstream dams. *Geomorphology* **2020**, *353*, 107011.
10. Lane, S.N.; Richards, K.S. Linking river channel form and process: time, space and causality revisited. *Earth Surf. Processes Landforms* **1997**, *22*(3), 249–260.
11. Lawler, D. The importance of high-resolution monitoring in erosion and deposition dynamics studies: examples from estuarine and fluvial systems. *Geomorphology* **2005**, *64*(1–2), 1–23.
12. Wu, B.; Zheng, S.; Thorne, C.R. A general framework for using the rate law to simulate morphological response to disturbance in the fluvial system. *Prog. Phys. Geogr.* **2012**, *36*(5), 575–597.
13. Grant, G.E. (Eds) The geomorphic response of gravel-bed rivers to dams: perspectives and prospects. *Gravel-bed Rivers: Processes, tools, environments*. Wiley Online Library, **2012**, 165–181.
14. Van, M.N.; Dung, N.V.; Hung, N.N.; Kumm, M.; Merz, B.; Apel, H. Future sediment dynamics in the Mekong Delta floodplains: Impacts of hydropower development, climate change and sea level rise. *Global Planet Change* **2015**, *127*, 22–33.
15. Fryirs, K.A. River sensitivity: a lost foundation concept in fluvial geomorphology. *Earth Surf. Processes Landforms* **2017**, *42*(1), 55–70.
16. Fryirs, K.A.; Brierley, G.J. *Geomorphic analysis of river systems: an approach to reading the landscape*: John Wiley & Sons, 2012.
17. Briggs, K.B. *High-frequency acoustic scattering from sediment interface roughness and volume inhomogeneities*: University of Miami, 1994.
18. <https://www.mikepoweredbydhi.com/>.
19. <https://www.tudelft.nl/en/>.
20. Galland, J.C.; Goutal, N.; Hervouet, J.M. TELEMAC: A new numerical model for solving shallow water equations. *Adv. Water Resour.* **1991**, *14*(3), 138–148.

21. Gad, M.A.; Saad, A.; El-Fiky, A.; Khaled, M. Hydrodynamic modeling of sedimentation in the navigation channel of Damietta Harbor in Egypt. *Coastal Eng. J.* **2013**, *55*(2), 350007-1-1350007-31.
22. Zhang, Y. CCHE2D-GUI-graphical user interface for the CCHE2D model user's manual-version 2.2. 2005.
23. Van, Rijn, L.C.; van Rossum, H.; Termes, P. Field verification of 2-D and 3-D suspended-sediment models. *ISH J. Hydraul Eng.* **1990**, *116*(10), 1270–1288.
24. Chang, H.H. Case study of fluvial modeling of river responses to dam removal. *J Hydraul Eng.* **2008**, *134*(3), 295–302.
25. Lee, H.Y.; Hsieh, H.M.; Yang, J.C.; Yang, C.T. Quasi-two-dimensional simulation of scour and deposition in alluvial channels. *J. Hydraul. Eng.* **1997**, *123*(7), 600–609.
26. Le, G.S.; Ho, L.H.; Tran, L.T.; Park, E. F28: A Novel Coupling Strategy for 1D–2D Hydraulic Models for Flood Risk Assessment of the Mekong Delta. Available at SSRN 4358313. 2023, pp. 23.
27. Giang, N.; Izumi, N. (Eds) Application of an integrated morphological model to Red River network. 2nd IAHR Symposium on River, Coastal and Estuarine Morphodynamics, RCEM 2001, 2001.
28. Kim, T.T.; Huong, N.T.M.; Huy, N.D.Q.; Tai, P.A.; Hong, S.; Quan, T.M.; et al. Assessment of the impact of sand mining on bottom morphology in the Mekong River in an Giang Province, Vietnam, using a hydro-morphological model with GPU computing. *Water* **2020**, *12*(10), 2912.
29. Cole, R.A.; Wu, Q. (Eds) Predicting bank failures using a simple dynamic hazard model. 22nd Australasian Finance and Banking Conference, Citeseer, 2009.
30. Rinaldi, M.; Darby, S.E. Modelling river-bank-erosion processes and mass failure mechanisms: progress towards fully coupled simulations. *Earth Surf. Processes* **2007**, *11*, 213–239.
31. Duong, T.T.; Do, M.D. Riverbank stability assessment under river water level changes and hydraulic erosion. *Water* **2019**, *11*(12), 2598.
32. Abderrezzak, K.E.K.; Moran, A.D.; Tassi, P.; Ata, R.; Hervouet, J.M. Modelling river bank erosion using a 2D depth-averaged numerical model of flow and non-cohesive, non-uniform sediment transport. *Adv. Water Resour.* **2016**, *93*, 75–88.
33. Cribb, M.; Darby, S. (Eds) Modelling the Influence of Riparian Vegetation on River Bank Erosion. AGU Fall Meeting Abstracts, 2002.
34. Dahale, P.; Nalgire, T.; Mehta, A.; Hiwase P. Slope stability analysis by GeoSlope. *Triple Helix* **2020**, *10*(01), 71–75.
35. Van Rijn, L.C. Principles of sediment transport in rivers, estuaries and coastal seas 1993.
36. Mishal, U.R.; Khayyun, T.S. Stability analysis of an earth dam using GEO-SLOPE model under different soil conditions. *Eng. Tech. J.* **2018**, *36*(5), 523–532.
37. Arshad, I.; Babar, M.M. Finite element analysis of seepage through an earthen dam by using geo-slope (SEEP/W) software. *Int. J. Res.* **2014**, *1*(8), 616–634.
38. Watson, A.; Basher, L. Stream bank erosion: a review of processes of bank failure, measurement and assessment techniques, and modelling approaches. A report prepared for stakeholders of the Motueka Integrated Catchment Management Programme the Raglan Fine Sediment Study Landcare Research, Hamilton, New Zealand. 2006.
39. Xu, N.; Xia, W.; Zhao, B.; Wu, T. Eds. The improved Simplified Bishop's Method considering the Difference of Inter-slice Shearing Force. Hydraulic Engineering III: Proceedings of the 3rd Technical Conference on Hydraulic Engineering (CHE 2014), Hong Kong, 13–14 December 2014, CRC Press, 2014.

40. Bishop, A.W. The use of the slip circle in the stability analysis of slopes. *Geotechnique* **1955**, *5(1)*, 7–17.
41. Janbu, N. Editor Application of composite slip surface for stability analysis. European Conference on Stability of Earth Slopes Stockholm, Sweden, 1954.
42. Agam, M.; Hashim, M.; Murad, M.; Zabidi, H. (Eds) Slope sensitivity analysis using spencer's method in comparison with general limit equilibrium method. *Procedia Chem.* **2016**, *19*, 651–658.
43. Van, T.N. Editor Coastal erosion, river bank erosion and landslides in the Mekong Delta: Causes, effects and solutions. Geotechnics for Sustainable Infrastructure Development, Springer, 2020.
44. Nguyen, N.A. Why does the river erosion situation become more complicated in the Mekong delta? *VN J. Sci. Technol. Eng.* **2018**, *60(1)*, 73–82.
45. Hung, L.M.; San, D.C. Bank erosion Mekong River. Southern Institute for Water Resources, 2002.
46. Hung, L.M.; Tanaka, H.; Tu, N.T.; Viet, N.T. (Eds) Prediction of river bank erosion in the Lower Mekong River Delta. Vietnam – Japan Estuary Workshop, Hanoi, Vietnam, 2006.
47. Kim, T.T.; Diem, P.T.M.; Trinh, N.N.; Phung, N.K.; Bay, N.T. Riverbank movement of the Mekong River in An Giang and Dong Thap Provinces, Vietnam in the period of 2005–2019. *VN J. Hydrometeorol.* **2020**, *6*, 35–45.

Research Article

Proposed procedure of survey and model application for forecasting flow landslide susceptibility and hazards – A case study in Tam Chung commune, Thanh Hoa province

Nguyen Huy Duong¹, Nguyen Thi Huyen¹, Pham Van Son¹, Tran The Viet², Nguyen Duc Ha^{1*}

¹ Vietnam Institute of Geosciences and Mineral Resources;
nguyenhuyduong112358@gmail.com; huyenkhanh216@gmail.com;
sontdc2007@gmail.com; nh14vn@gmail.com

² Thuy loi University; tranthev@gmail.com

*Corresponding: nh14vn@gmail.com. Tel.: +84–989258025

Received: 12 April 2023; Accepted: 7 June 2023; Published: 25 September 2023

Abstract: In this study, the main aim is to apply SMCE (Spatial Multi-Criteria Evaluation) and Flow-R models to predict flow landslide susceptibility and hazard in Tam Chung commune, Thanh Hoa province (Vietnam). For this, nine factor maps including slope, relief amplitude, elevation, drainage density, engineering geology, groundwater availability, land cover, lineament density, and weathering crust type were collected and prepared for generation of landslide susceptibility map using the weights generated from the SMCE model. Flow-R model was then used to forecast potential hazards related to the movement of flow landslide material. Landslide inventory collected from field survey was used to validate the landslide susceptibility and hazard maps. Results of this study showed that the susceptibility map, generated by applying the SMCE model, showed a high level of accuracy. By integrating detailed field surveys with the Flow-R model, the study identifies areas with low susceptibility to landslides but high vulnerability to material displacement. This study is helpful and supportive for better landslide hazard management in the study area, and facilitating informed decision-making in disaster prevention and mitigation.

Keywords: Flow landslide; Landslide susceptibility; Landslide hazard; SMCE model; Flow-R model.

1. Introduction

Landslides are prevalent natural disasters in mountainous regions, causing significant damage to human lives, infrastructure, properties, the environment, and socio-economic activities. According to United Nations statistics, since the beginning of the 21st century, landslide disasters have claimed the lives of over 50,000 people and caused property damage amounting to billions of dollars [1].

Landslides can occur in most mountainous and hilly regions, resulting from a combination of natural conditions such as geology, topography, and morphology, as well as human activities that alter the landscape, including the construction of buildings, roads, and mineral extraction. However, the occurrence of landslides is often associated with external triggers, with rainfall being the most common activating factor worldwide, including in Vietnam [2–4]. Moreover, a heavy rainfall event can trigger multiple landslide events simultaneously at different locations. With the influence of climate change, the frequency of intense rainfall events is projected to increase, leading to a higher occurrence rate and more severe intensity of landslide disasters [5–7].

Based on the characteristics of the movement, landslides can be classified into different types such as fall, topple, slide, lateral spread, and flow [8]. Among these types, predicting the potential hazards associated with flow landslides presents significant challenges due to their high velocity, unpredictability, large volume, and destructive potential. Flow landslides involve the movement of saturated or semi-fluid material down a slope and can be further classified into debris flows, mudflows, and earthflows, depending on the composition of the flowing material. The complex and dynamic behavior of flow landslides leads to rapid and nonlinear responses to triggering factors, resulting in unpredictable paths and magnitudes. Therefore, when implementing measures for prevention, mitigation, and settlement planning in areas prone to flow landslides, the identification of landslide susceptibility alone is insufficient. It is also crucial to forecast potential hazards in advance [9]. Landslide susceptibility refers to the relative probability of future landsliding, primarily determined by the inherent characteristics of a specific location, while landslide hazard represents the potential occurrence of landslides within a designated area, encompassing both source areas and runout zones [10].

Globally, as well as in Vietnam, landslide susceptibility maps are typically generated at small or medium scales with the objective of identifying areas that are prone to landslides for urban planning purposes and focused detailed investigations [11–15]. These maps are commonly constructed using various methods, such as statistical approaches (e.g., WoE - Weight of Evidence, FR- Frequency Ratio) or expert-based methods (e.g., AHP - Analytic Hierarchy Process, SMCE). Each method has its own advantages, and there is no universally recognized standard method due to the difficulty in comparing different methods with different datasets [16]. However, in situations where data are incomplete or insufficiently detailed, the use of expert opinions is often considered more effective [17].

To forecast potential hazards from flow landslides, numerical models such as LS-RAPID, DAN3D, and Debris 2D are commonly utilized [18–22]. These models have been found to provide high accuracy results but are typically suitable for small-scale applications, such as slopes or small catchments, due to their demanding data, time, and economic requirements. The Flow-R model, on the other hand, is an empirical GIS-based model that has been successfully applied in simulating flow landslide events in various locations worldwide [23–24]. It is one of the few models capable of forecasting flow landslide hazards on a broader scale (e.g., commune, district) without the need for detailed data such as soil analysis, geophysical measurements, etc.

The mountainous provinces of Vietnam are characterized by diverse geological features, steep topography, and high rainfall intensity, resulting in numerous landslide-prone areas. However, economic constraints limit the feasibility of conducting detailed surveys and applying complex material flow simulation models to all highly susceptible landslide zones. This is especially true in sparsely populated areas where warning about the potential impact of material flow is essential but employing complex models may exceed the budget allocated for relocating households. Therefore, in order to effectively support the work of warning and assessing the impact of material flow in the mountainous provinces of Vietnam, it is essential to develop a surveying process and apply appropriate models to provide forecasts of hazards in prioritized regions (residential areas and areas with frequent human activities).

This study introduces a procedure for predicting areas susceptible to and affected by flow landslides, applied, and tested in the Tam Chung commune - a mountainous region prone to flow landslides. The approach combines field surveys with the application of the SMCE and Flow-R models. Initially, susceptibility maps at a medium scale are generated using the SMCE model to identify susceptible areas of landslide occurrence. Subsequently, vulnerable areas deemed relevant to residential and human activities are further investigated in detail and analyzed using the Flow-R model to forecast the flow landslide hazards arising from flow landslide materials.

2. Methodological steps

The proposed procedure for investigating and forecasting high susceptibility areas and potential hazards by flow landslides is illustrated in Figure 1. The procedure involves the following primary steps:

- Data collection and compilation: Gathering and analyzing information on the current status of landslides, as well as relevant data and diagrams of factors influencing the landslide occurrence.
- Field investigation: Surveying locations where debris flow has occurred and constructing small- or medium-scale landslide inventory maps. Identifying common characteristics of past landslide events to determine the associated factors in the study area, to generate spatial factor maps (input for SMCE model) at a small- or medium-scale.
- Applying the SMCE model to construct the landslide susceptibility map (at small- or medium-scale).

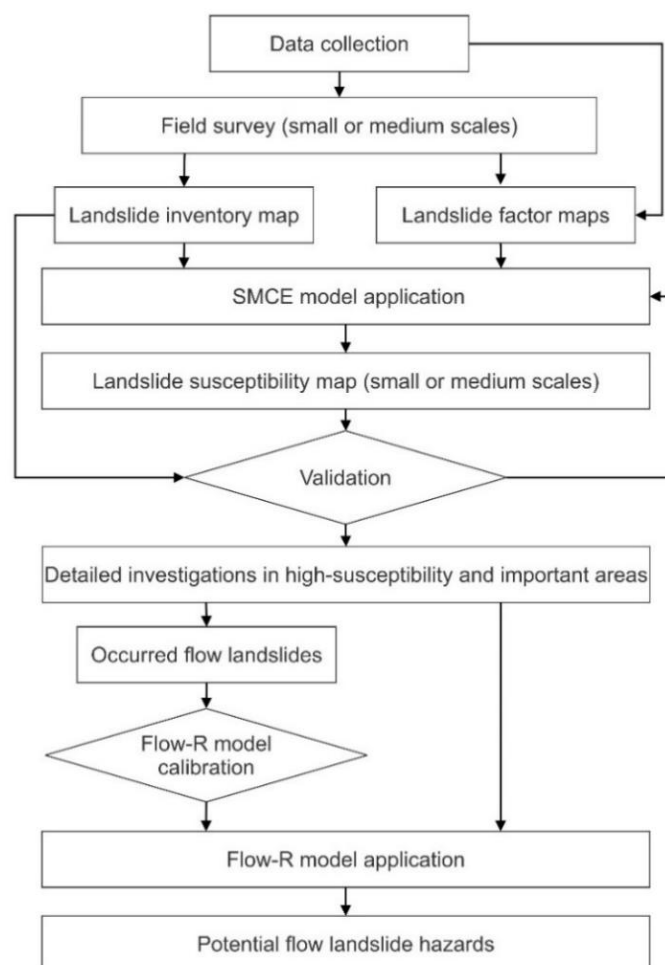


Figure 1. Process diagram of the combined application of field investigation and SMCE and Flow-R models to forecast flow landslide hazards.

To carry out the task of delineating landslide susceptibility areas, the authors propose the adoption of the Spatial Multi-Criteria Evaluation (SMCE) method [25]. The SMCE method is an extension of the AHP coupled with statistical methods. It facilitates multi-criteria analysis (multi-standard evaluation) within a spatial model [26]. This method overcomes the limitations of quantitative evaluation methods that require a large amount of available and detailed data, as well as a comprehensive inventory dataset of landslides.

In the SMCE model, factors contributing to landslide occurrence are represented as spatial maps and evaluated based on expert knowledge [27]. The input data for the method

consist of a set of component maps that serve as representative spatial criteria classified into groups, standardized, and assigned weights. The component map layers are considered primary “criteria”, and the attributes of each component map layer are secondary “criteria”. The sensitivity to landslides of each “criteria” is expressed by weight values, denoted as W . The weight values of W are constrained within the range of 0 to 1, where the total weight value of all primary “criteria” (component map layers) or the total weight value of all secondary “criteria” within each primary “criteria” (attribute layers within each component map layer) equals 1. More detailed information regarding the SCME model can be found in reference [25].

The output data consists of a “composite index map” that represents the simulation results within the model, with areas classified into different landslide susceptibility index (LSI) groups [25].

- Verification and calibration of the susceptibility map with the landslide inventory map.

The susceptibility map derived from the SMCE method will be compared to the existing landslide inventory map in order to evaluate its accuracy. The application of the SMCE model needs to be performed and calibrated until the best verification results are obtained.

- Detailed investigations in high-susceptibility and important areas.

Based on the results of applying the SMCE model, detailed investigations are required for areas with high or very high landslide susceptibility. Depending on the available manpower, budget, and time constraints of each locality, the detailed investigation can be conducted in all high- susceptibility areas or prioritized in significant areas (e.g., densely populated areas, infrastructure, transportation). The objectives of this detailed investigation are: (1) to identify the locations where flow landslides have occurred and (2) to delineate the areas with high potential for future flow landslide occurrences.

- Application of the Flow-R model in the identified flow landslide locations for calibration and determination of model parameters.

The Flow-R model, an acronym for “Flow path assessment of gravitational hazards at a regional scale” [28], is built on the Matlab platform and primarily aims to simulate the flow propagation of materials in a 2D space based on empirical methods. The input data required for the Flow-R model predominantly comprise terrain-related maps, such as slope, curvature, and flow accumulation. The algorithms and parameters for flow direction, inertia, and friction loss used in the Flow-R model are determined through calibration with past flow landslide events within the same region or under similar conditions. More detailed information regarding the Flow-R model can be found in reference [28–29].

- Application of the Flow-R software (with calibrated parameters) to forecast the potential hazards associated with material flow in areas identified as susceptible to flow landslides.

3. Study area and data collection

Tam Chung commune is situated in Muong Lat district and is characterized as a highland area encompassing a natural land expanse of approximately 123.89 km². Geographically, it is bounded by coordinates ranging from 20°29’54” to 20°39’12” latitude North and from 104°34’02” to 104°41’58” longitude East. The administrative borders of Tam Chung commune are shared with Muong Ly commune to the east, Ten Tan commune to the west, Nhi Son commune and Muong Lat town to the south, and Tan Xuan commune (Moc Chau-Son La) and Hua Phan district (Laos) to the north. As of the statistical records until 2019, the commune is home to a total population of 4,070 individuals residing in 852 households, resulting in an average population density of approximately 13 people/km² [30].

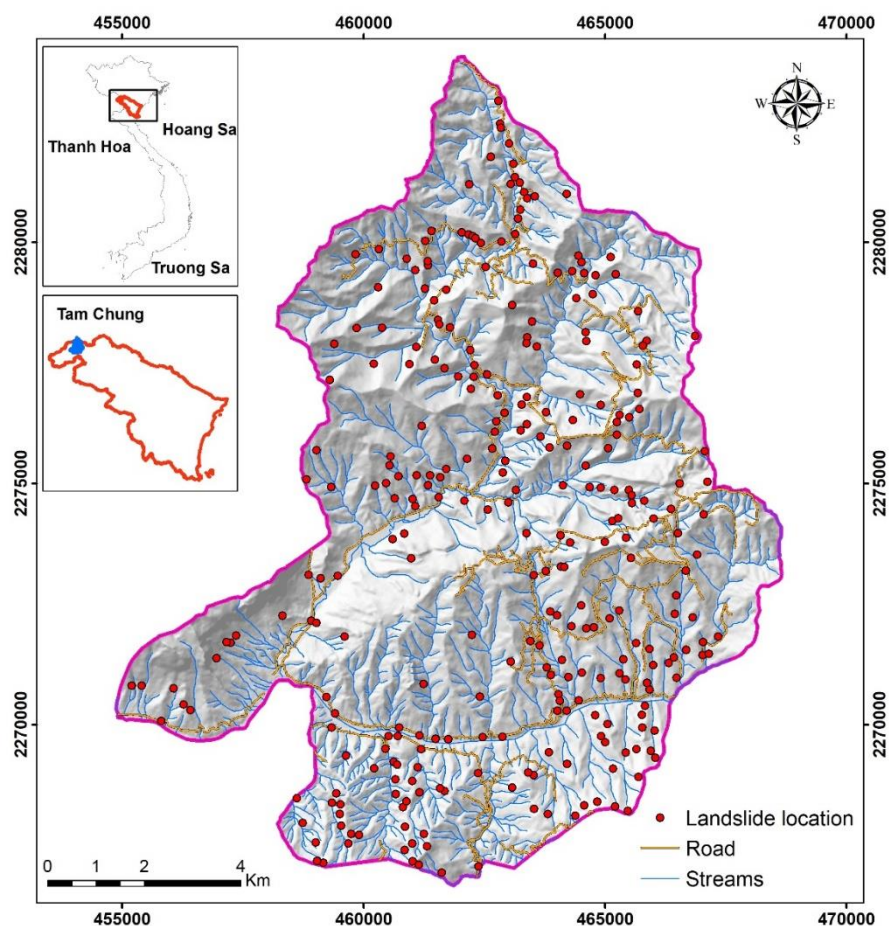


Figure 2. The location of Tam Chung commune and the landslide inventory.

The topography of Tam Chung commune is highly diverse and complex. It mainly consists of interconnected high mountains forming mountain ranges, which are divided by streams, creating distinct regions. The overall terrain has a basin-like shape sloping in three directions: northeast, northwest, and southeast. The average absolute elevation ranges from 650–700 m, with steep slopes averaging from 25° to 35° and some areas exceeding 35°. The lowest point is located in the area near the mouth of the Ma river in the southeast of the commune, with an absolute elevation of approximately 135 m, while the highest point is in the mountainous region in the northwest of the commune, with an absolute elevation of approximately 1,574 m. The average annual rainfall in Tam Chung commune is 1,266 mm, with the highest recorded rainfall at 1,969 mm and the lowest recorded rainfall at 1,014 mm. However, the majority of rainfall is concentrated during the rainy season from April to October, with heavy rain events typically occurring in July and August.

Geohazards, particularly landslides, are observed in most of the villages within Tam Chung commune, with the highest occurrence in Suoi Long, on followed by Poong, Lat, Pom Khuong, Cha Lan, and Sai Khao. Flow landslides are a common type of landslide in the area, often occurring on naturally eroded slopes, predominantly in areas of reforestation and agricultural land.

Based on the data collected from the 2019 landslide field investigation conducted by the State-Funded Landslide Project (SFLP) “Investigation, Assessment, and Zoning of Landslide Hazard in the Mountainous Provinces of Vietnam” and the Google Earth satellite imagery interpretation results, the research team identified 296 landslide occurrences within the Tam Chung commune. The field surveys revealed that the highest concentration of landslide occurrences is observed in areas characterized by natural slope gradients ranging from 25.74° to 42.26°, elevations varying between 135 and 608.98 meters, cross-section cutting densities

ranging from 1.93 to 4.16 km/km², and deep section cutting densities ranging from 144.88 to 442.15 m/km². Certain locations exhibited a pattern of recurrent landslides, particularly during periods of heavy rainfall, which have been documented in recent years. The corresponding landslide inventory is presented in Figure 2.

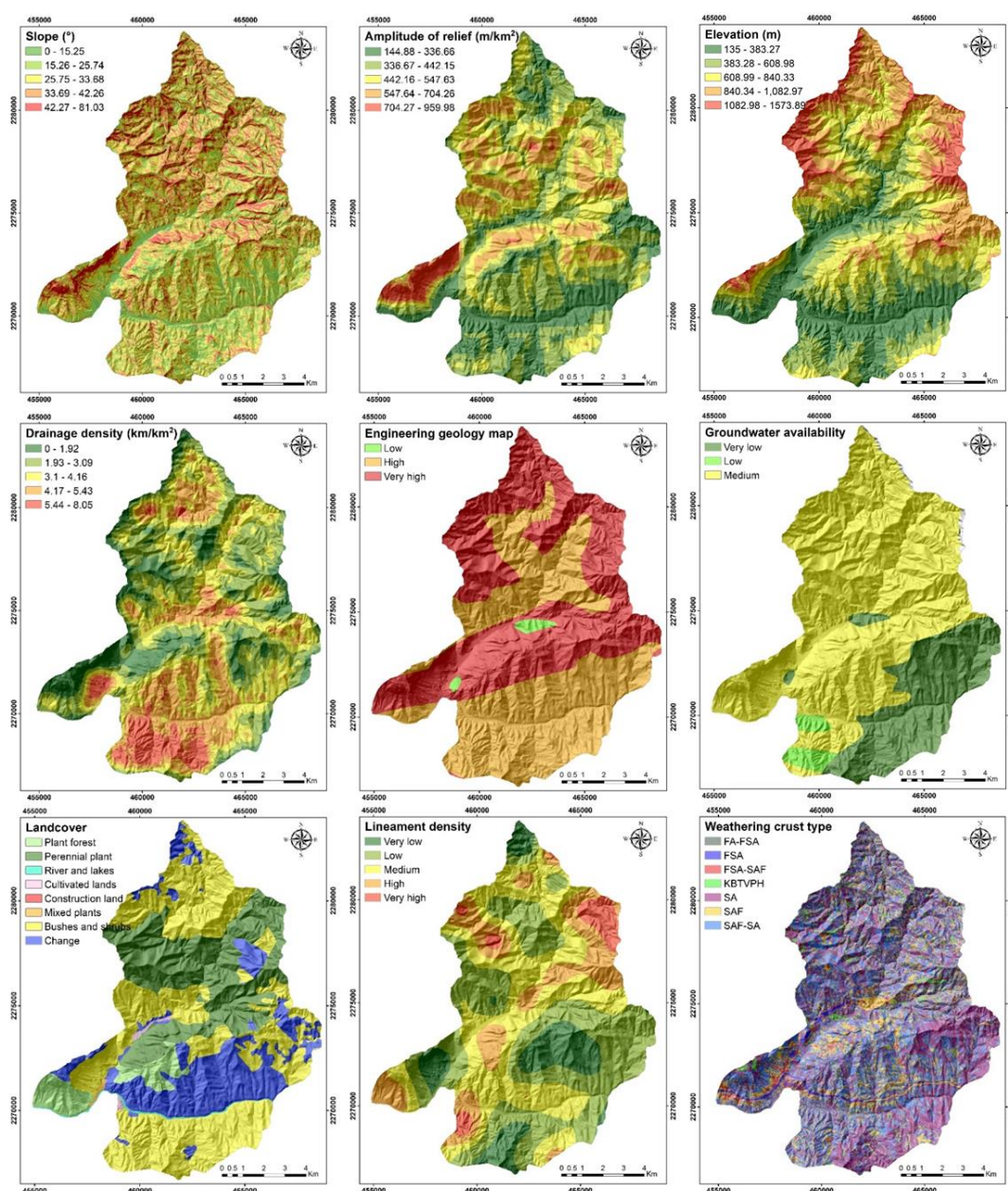


Figure 3. The landslide factor maps in Tam Chung commune.

The analysis and evaluation of the factors influencing landslide susceptibility in the Tam Chung commune, including the determination of their weights, were conducted by summarizing the assessment opinions of three groups: field survey personnel, landslide research experts, and model implementation personnel. Nine factors have been identified as crucial in the formation of landslides within the Tam Chung commune: slope, relief amplitude, elevation, drainage density, engineering geology, groundwater availability, land cover, lineament density, and weathering crust type. Therefore, these nine landslide factor maps have been selected as the primary input data for the SMCE model to assess and zoning landslide susceptibility areas. Therefore, mentioned maps were obtained from the SFLP project, utilizing scales of 1:10,000 and 1:50,000, and featuring a precise resolution of 20 meters (Figure 3).

The criteria weights (W) of each landslide factor map and their attributes are summarized in the “criteria tree” depicted in Figure 4.

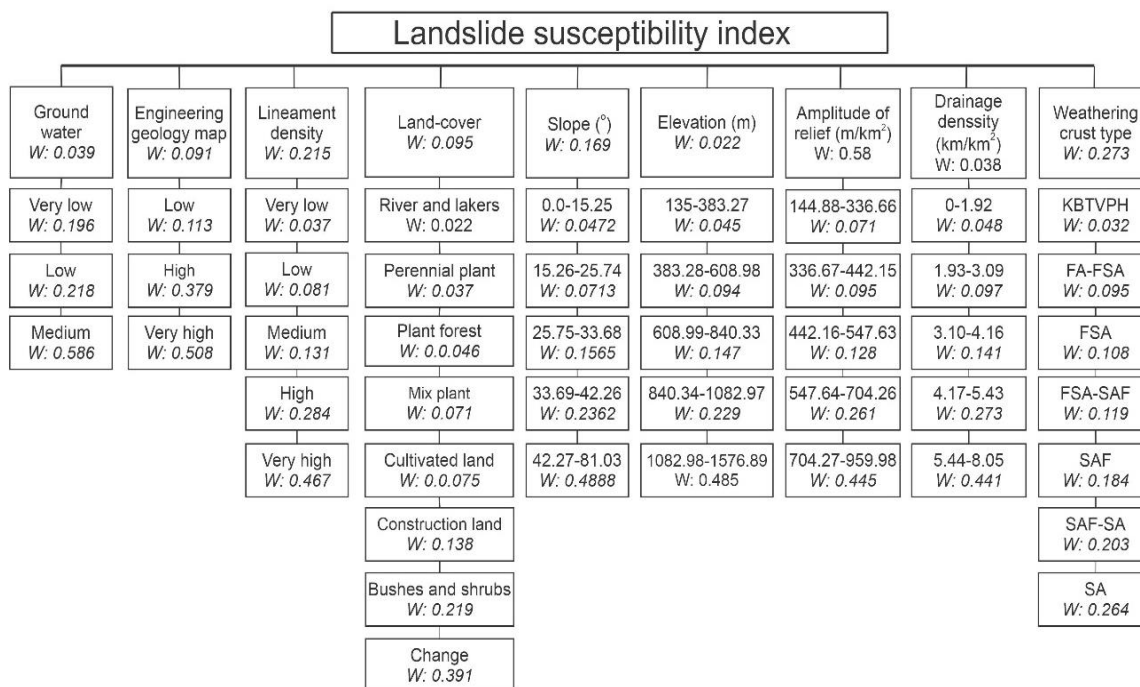


Figure 4. Criteria tree for criteria weight (W), showing the influence on landslide occurrence of nine factors.

4. Results and discussion

4.1. SMCE model application

By analyzing the natural distribution (Jenks natural breaks classification method [31]) of the Landslide Susceptibility Index (LSI) across all pixels on the susceptibility index map, four threshold values have been established. These thresholds are used to classify the area of the Tam Chung commune into five distinct zones, each representing different levels of susceptibility: very low, low, moderate, high, and very high (Table 1).

Table 1. LSI thresholds for generating landslide susceptibility map in Tam Chung commune.

Landslide susceptibility index (LSI)	Landslide susceptibility class
0–0.0872	Very Low
0.0873–0.1158	Low
0.1159–0.1432	Moderate
0.1433–0.1802	High
0.1803–0.2975	Very High

- The zone exhibiting a significantly high susceptibility to landslides covers an estimated area of 24.23 km², accounting for approximately 15% of the total natural area. This area of heightened susceptibility is primarily concentrated in the northwestern portion of Lat village, Tam Chong village, and the eastern region of Hin Phang village.

- The high susceptibility zone spans an area of approximately 30.22 km², accounting for approximately 29% of the total natural area. This zone is characterized by a scattered and interspersed distribution, often adjacent to areas exhibiting a very high susceptibility to landslides.

- The zone characterized by moderate susceptibility to landslides covers an area of approximately 44.74 km², representing approximately 36% of the total natural area. It is primarily concentrated in the eastern and southeastern regions of Tam Chung commune, while the remaining portion is scattered across areas with low-lying topography.

- The low susceptibility and very low susceptibility zones cover an approximate area of 24.54 km², comprising approximately 20% of the total natural area. These zones are primarily concentrated along the floodplains of the Lat stream, specifically in Pong Ngoai village.

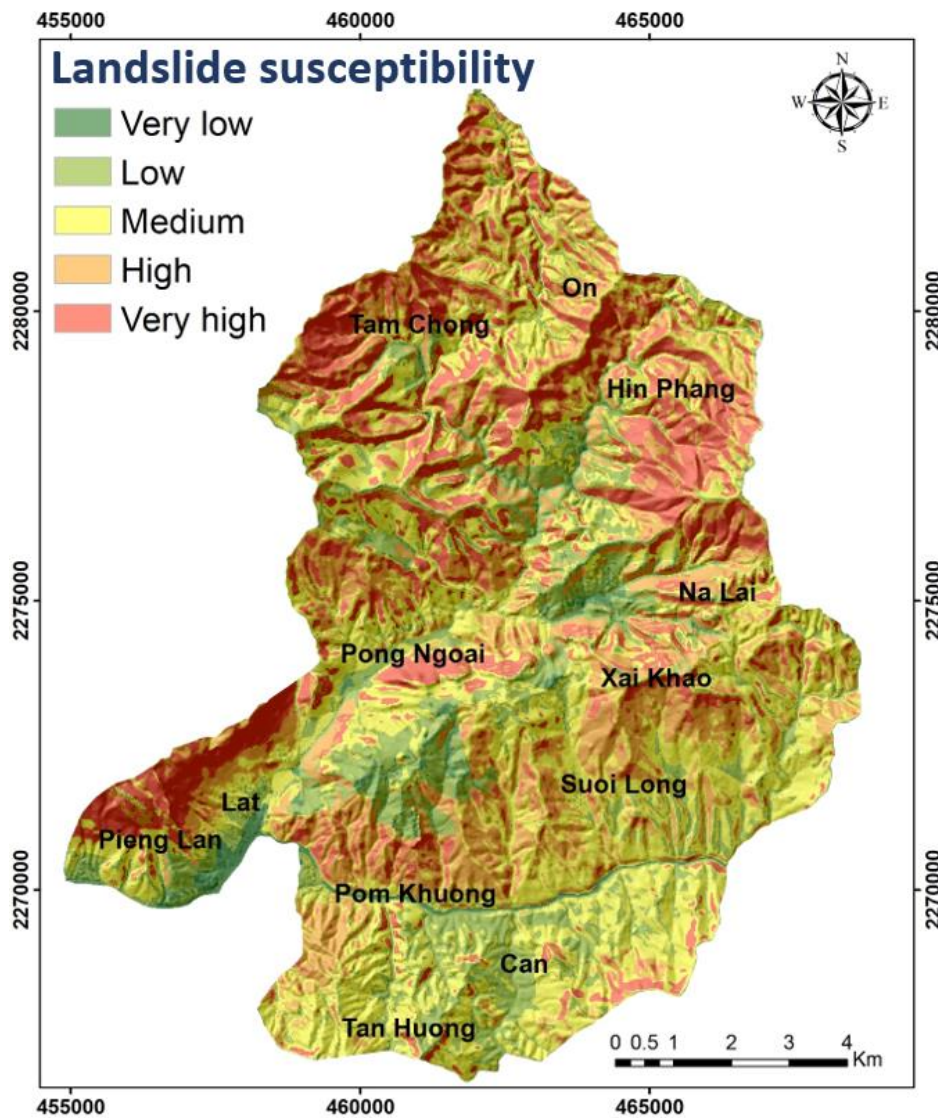


Figure 5. The landslide susceptibility map was constructed using the SMCE model.

The comparison between the landslide susceptibility zoning results obtained using the SMCE method and the findings from the field investigation (Table 2) reveals a high level of conformity and reliability. The majority of observed landslides occurred in areas identified as high and very high susceptibility zones (78%) and no landslide events were reported in locations designated as very low susceptibility.

Although the SMCE model heavily relies on expert opinions, it has successfully addressed the requirement for extensive data collection to identify high susceptibility landslide areas. However, a notable observation from comparing the landslide susceptibility map with the landslide inventory map is that a significant number of landslides (67 landslide locations or 22%) occurred in areas assessed as having moderate to low susceptibility. Upon further investigation, these landslides were predominantly small-scale events, occurring along roads and within residential areas. Two main factors could explain this issue: the terrain data used in this study was not updated to reflect rapid changes in reality (construction activities), and the resolution of the data (20 m) was not detailed enough to capture small-scale slopes.

Table 2. The results of the landslide susceptibility classification using the SMCE method were compared with the landslide inventory map.

Landslide susceptibility class	Predicted landslide susceptibility classes		Observed landslides	
	Area (km ²)	Percentage (%)	Number	Percentage (%)
Very Low	2.81	2%	0	0%
Low	21.73	18%	12	4%
Moderate	44.74	36%	55	18%
High	30.72	29%	84	29%
Very High	24.23	15%	145	49%

4.2. Flow-R model application

To calibrate the algorithms and parameters of Flow-R for suitability in the Tam Chung commune area, two locations that experienced flow landslide events in August 2018 were chosen for calibration. Location 1 corresponds to the Tam Chung Ethnic Secondary School in Lat village (as depicted in Figure 6), while Location 2 is situated in Suoi Long village (Figure 7). The flow landslide that occurred at Location 1 resulted in significant devastation to several structures within the school premises, leading to an estimated economic loss exceeding 6 billion VND. Initially, the landslide encompassed three distinct sliding masses, spanning a total area of approximately 6 hectares, and affecting an additional area of approximately 16 hectares. The debris involved in the flow consisted of a mixture of boulders, gravel, soil, sand, and water, which cascaded from the source areas towards the secondary school and the residential zone of Lat village, covering a distance of approximately 1.2 km.

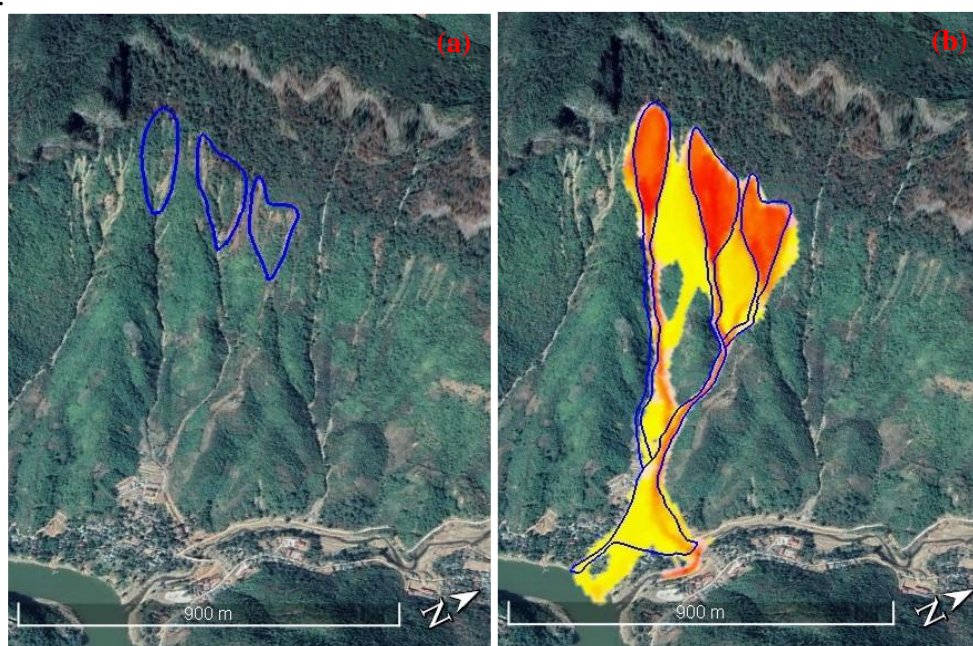


Figure 6. (a) The initial area (blue area); (b) The observed hazard (blue) and the simulation result (yellow to red) in location 1 by the Flow-R model.

Although the flow landslide at Location 2 did not cause damage to infrastructures, it severely affected agricultural land, rendering it unsuitable for cultivation. The initial area of the flow landslide 2 was estimated to be around 2.5 hectares, with a total impacted area of approximately 10 hectares. The materials involved in the flow, including boulders, gravel, soil, sand, and water, followed the stream course and crossed the National Highway 16, extending a distance of about 2 km.

The results of applying the Flow-R model to the two locations 1, 2 were compared with the actual field conditions and presented in Figure 6 and Figure 7. The blue areas represent

the initial parts of landslides (determined based on field surveys and remote sensing analysis), while the yellow to red areas indicate the results from the Flow-R software, with increasing probabilities of being affected by landslide materials. Regarding flow direction and length, the implementation of the Flow-R model in the two calibrated areas exhibited a notable resemblance to the field observations. Furthermore, the accuracy of the predicted hazard areas was relatively high, with 93% and 79.5% of the actual hazard areas (in location 1 and location 2, respectively) overlapping with the simulated hazard areas.

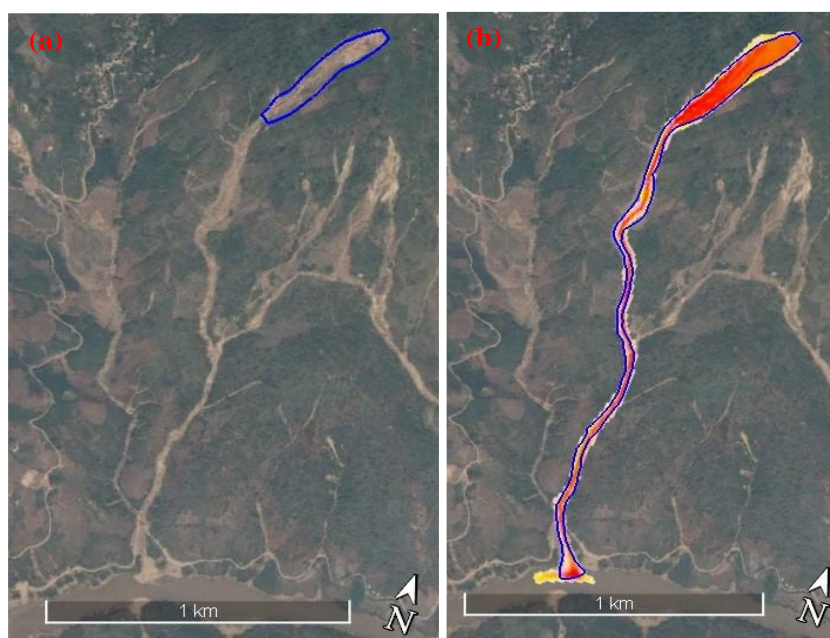


Figure 7. (a) The initial area (blue area); (b) The observed hazard (blue) and the simulation result (yellow to red) in location 2 by the Flow-R model.

Based on the results obtained from the SMCE model for landslide susceptibility zoning, focused investigations and surveys were conducted in areas exhibiting high susceptibility and posing potential risks to the population and public infrastructure. A total of 17 areas prone to flow landslides were identified, primarily concentrated in Suoi Long, Lat, Pieng Lan, and Pong Ngoai villages. Subsequently, these areas were subjected to the calibrated Flow-R model to predict the potential extent of material impact in the event of flow landslide occurrences. The results of applying the Flow-R model to these areas are presented in Fig. 8, where increasing probabilities of being affected by flowing material are represented by varying shades from yellow to red. The predicted material flows were found to potentially travel significant distances, ranging from 0.7 km to over 2 km, posing a significant threat to residential areas and potentially causing extensive damages.

The Flow-R model is employed for simulating the spatial extent of flow landslides and exhibits remarkable simulation capabilities. It stands out among global software programs by allowing material impact forecasting without the need for detailed geotechnical parameter determination, thereby eliminating the requirement for soil and rock sampling and analysis. The primary advantage of the Flow-R software lies in its suitability for large-scale areas, such as entire watersheds, with basic input data requirements. However, due to its reliance on basic input data, the Flow-R model can only provide preliminary predictions regarding the areas susceptible to material impact, without being able to forecast the velocity or thickness of the material.

The calibration results of the model reveal that certain discrepancies in the primary flow directions between the simulated and actual conditions can be attributed to the inaccuracies in representing the terrain in the digital elevation model (DEM) data. According to [23], the performance of the Flow-R model is highly dependent on the accuracy of the DEM. The use

of a DEM with a resolution of approximately 10 m (or finer) yields the best results, whereas employing a DEM with a resolution of around 25 m significantly reduces accuracy. Due to data limitations in this study, the authors were unable to experiment with more detailed DEMs for comparison. However, it is recommended to apply the Flow-R model using a maximum DEM resolution of 20m.

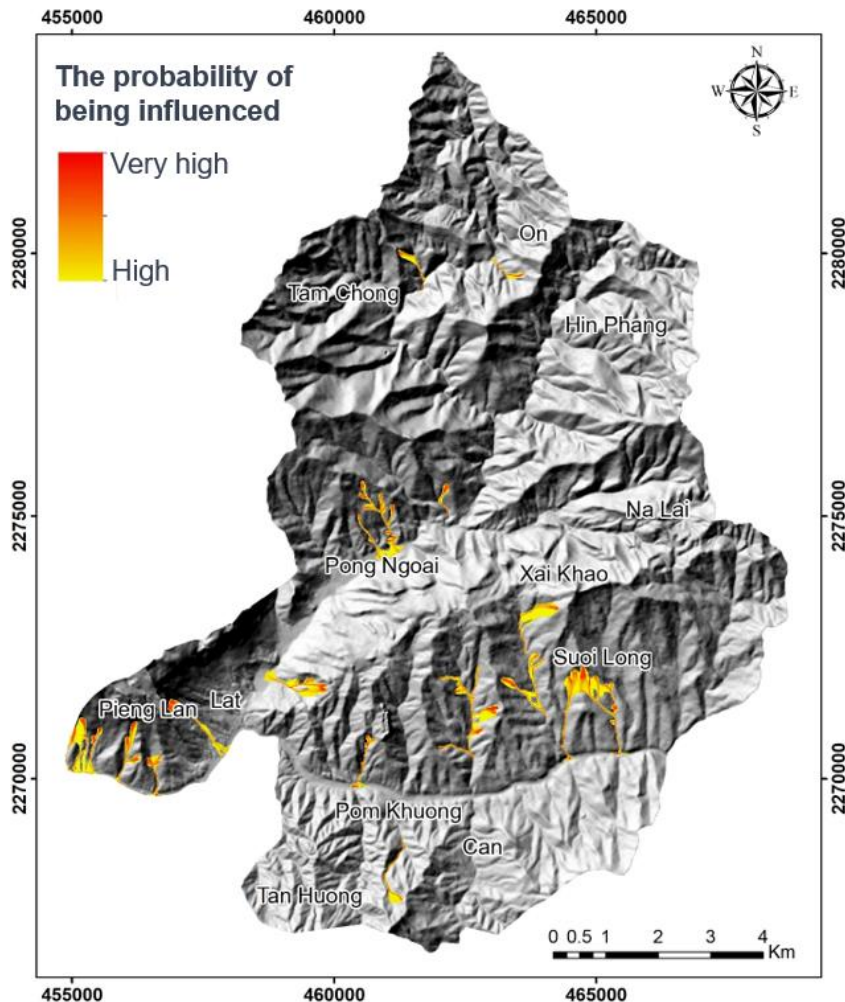


Figure 8. The potential hazards are identified through the application of the Flow-R model in Tam Chung commune.

Another limitation that may affect the simulation results of the Flow-R model is its inability to account for the presence of structures such as bridges, underground culverts, and buildings. The failure to represent the flow of materials beneath bridges or within underground culverts results in an overestimation of material flow in the surrounding areas compared to reality. Conversely, the absence of structures such as buildings leads to an underestimation or lack of prediction of material flow in the vicinity.

The results from applying the proposed procedure to Tam Chung commune clearly demonstrate the necessity of combining the SMCE and Flow-R models for forecasting flow landslide susceptibility and hazards. The application of the SMCE model has greatly assisted in identifying numerous landslide-prone areas, enabling focused detailed investigations. However, on-site surveys and the application of the Flow-R model have been limited to residential or inhabited areas, saving significant costs and time.

Residential areas tend to concentrate in flat areas, which are generally evaluated as having low or moderate landslide susceptibility. Consequently, residents and local authorities may become complacent and may not implement appropriate prevention measures. The

results from the Flow-R model have highlighted the importance of simulating the flow of landslide materials to forecast potential hazard areas. With their extended reach and spread, the predicted flow materials from the 17 flow landslides have the potential to directly impact residential areas and transportation routes.

5. Conclusion

This study presents a comprehensive approach that integrates field surveys and the application of the SMCE and Flow-R models to forecast the potential extent of material impact during flow landslide occurrences. The use of the SMCE model at small to medium scales optimizes resource allocation by identifying priority areas for detailed investigations. This approach minimizes the time and cost associated with extensive field surveys and allows for targeted data collection in high-susceptibility areas. At larger scales, field surveys and the application of the Flow-R model are subsequently conducted to predict areas susceptible to material displacement.

The proposed procedure is successfully applied and validated in the Tam Chung commune, Muong Lat district, Thanh Hoa province, demonstrating its high reliability. Through field surveys and the application of the Flow-R model, several areas are identified with low landslide susceptibility but high susceptibility to material displacement. Thus, for geohazard events with prolonged impacts, such as flow landslides, the application of material flow simulation models is crucial for effective prevention and damage mitigation.

In areas already mapped with landslide susceptibility zoning, detailed investigations and the implementation of the Flow-R model can be conducted to delineate areas at risk of material displacement. For larger areas characterized by diverse geological conditions, the Flow-R model should be supplemented with additional geological maps. In areas of high significance, characterized by dense populations and critical infrastructure, the application of more precise models, such as detailed 3D models of the terrain, analysis of soil samples to determine geotechnical parameters, and geophysical surveys to estimate material thickness, should be considered.

Based on the forecasted displacement trends of sliding materials, local authorities should adopt a combination of structural and non-structural measures to minimize potential damage. Non-structural measures include raising awareness among the population, proactively evacuating residents in high-susceptibility areas during heavy rainfall and adjusting urban planning and infrastructure in the region. Proposed structural measures for densely populated areas include initiating landslide mass movements in a preemptive manner, constructing material barriers along the flow path of flow landslides, altering the direction of material flow, and reinforcing structures within the hazardous zone.

By integrating statistical analysis, expert knowledge, and model application, despite the existence of certain limitations in the results, this study contributes valuable insights into the assessment and zoning of landslide hazards. The findings enhance the understanding and management of landslide hazards in the Tam Chung commune, facilitating informed decision-making for disaster prevention and mitigation efforts. These research findings will be integrated into a shared inter-sectoral database, serving the early warning system for geohazards in the mountainous provinces of Vietnam in general, and specifically in Thanh Hoa province [32]. Furthermore, the presented results will serve as a scientific basis for the development of technical regulations and the management of geohazard investigative operations in Vietnam [33].

Authors contribution: Constructing research idea: N.T.H., N.D.H.; Sample analysis: N.H.D., N.D.H., N.T.H., P.V.S.; Writing original draft preparation: N.D.H., N.T.H.; Writing review and editing: T.T.V.

Acknowledgments: The research is a part of the project “Designing and establishing a unified interdisciplinary big data system for early warning of landslides, debris flows, and flash floods” (TNMT.2021.04.07). Additionally, the authors received support from the project “Establishing a scientific foundation and proposing regulations for managing geohazard, environmental geology investigative activities, monitoring, and warnings” (TNMT.2022.01.33). The authors are grateful to the two anonymous reviewers for their insightful comments and suggestions that improved this paper.

Conflicts: The authors declare that this article was the work of the authors, has not been published elsewhere, has not been copied from previous research; there was no conflict of interest within the author group.

References

1. Mizutori, M. SRSR Statement for the International Landslide Consortium Conference Kyoto, Japan. Proceedings of 2018 IPL Symposium on Landslides, 03 December 2018, Kyoto University, Uji Campus, Kyoto, Japan.
2. Polemio, M.; Petrucci, O. Rainfall as a landslide triggering factor: an overview of recent international research. The 8th International Symposium on Landslides in Cardiff in the Year, 2000.
3. Crosta, G.B.; Frattini, P. Rainfall-induced landslides and debris flows. *Hydrol. Processes* **2008**, *22*(4), 473–477. Doi:10.1002/hyp.6885.
4. Hung, L.Q.; Van, N.T.H.; Son, P.V.; Ninh, N.H.; Tam, N.; Huyen, N.T. Landslide Inventory Mapping in the Fourteen Northern Provinces of Vietnam: Achievements and Difficulties. In: Sassa, K.; Mikoš, M.; Yin, Y. (eds) *Advancing Culture of Living with Landslides*. Springer, Cham. **2017**, Doi:10.1007/978-3-319-59469-9_44.
5. Dai, F.C.; Lee, C.F.; Ngai, Y.Y. Landslide risk assessment and management: an overview. *Eng. Geol.* **2002**, *64*(1), 65–87. Doi:10.1016/S0013-7952(01)00093-X.
6. Jakob, M.; Lambert, S. Climate change effects on landslides along the southwest coast of British Columbia. *Geomorphology* **2009**, *107*(3–4), 275–284. Doi:10.1016/j.geomorph.2008.12.009.
7. Gariano, S.L.; Guzzetti, F. Landslides in a changing climate, *Earth–Sci. Rev.* **2016**, *162*, 227–252. Doi:10.1016/j.earscirev.2016.08.011.
8. Cruden, D.M.; Varnes, D.J. Landslide types and processes. In: Turner AK, Schuster RL (eds) *Landslides: investigation and mitigation (Special Report)*. Washington, DC, USA: National Research Council. Transportation and Research Board Special Report **1996**, *247*, 36–75.
9. Sassa, K.; Nagai, O.; Solidum, R.; Yamazaki, Y.; Ohta, H. An integrated model simulating the initiation and motion of earthquake and rain induced rapid landslides and its application to the 2006 Leyte landslide. *Landslides* **2010**, *7*(3). Doi:10.1007/s10346-010-0230-z.
10. Online available: <https://www.usgs.gov/faqs/what-landslide-hazard-map>.
11. Minh, V.C. et al. Study on the prediction of landslides, flash floods, and debris flows in Lai Chau province. Institute of Geology, Vietnam Academy of Science and Technology, 1996.
12. Van, T.T. et al. Survey and assessment of the landslide hazards for 13 sections of the Ho Chi Minh Highway and 4 sections of National Highway 1, proposing measures to ensure the safety of traffic, production, and living activities in residential areas. Vietnam Institute of Geological Sciences and Mineral Resources, 2006.
13. Hung, L.Q. et al. Study on the application of WebGIS technology, high-resolution RADAR image analysis, and GIS spatial modeling to develop a geogazard and environmental disaster warning system in Vietnam. Case study in Bac Kan province. Vietnam Institute of Geological Sciences and Mineral Resources, **2014**.

14. Hung, L.Q.; Van, N.T.H.; Duc, D.M.; Ha, L.T.C.; Van Son, P.; Khanh N.H.; Binh L.T. Landslide susceptibility mapping by combining the analytical hierarchy process and weighted linear combination methods: a case study in the upper Lo River catchment (Vietnam). *Landslides* **2016**, 13(5), 1285–1301. doi:10.1007/s10346-015-0657-3.
15. Huyen, N.T.; Khanh, N.Q.; Duong, N.H.; Ninh, N.H.; Ha, N.D. The results delineate the susceptible areas to landslides and flash floods in Da Nang City. *VN J. Hydrometeorol.* **2023**, 745, 21–33. doi:10.36335/VNJHM.2023(745).21-33.
16. An, H.; Tran, T.V.; Lee, G.; Kim, Y.; Kim, M.; Noh, S.; Noh, J. Development of time-variant landslide-prediction software considering three-dimensional subsurface unsaturated flow. *Environ. Modell. Software* **2016**, 85, 172–183. <https://doi.org/10.1016/j.envsoft.2016.08.009>.
17. Thiery, Y.; Malet, J.P.; Sterlacchini, S.; Puissant, A.; Maquaire, O. Landslide susceptibility assessment by bivariate methods at large scales: application to a complex mountainous environment. *Geomorphology* **2007**, 92(1–2), 38–59. doi:101016/j.geomorph200702020.
18. Quang, L.H.; Loi, D.H.; Sassa, K.; Takara, K.; Ochiai, H.; Dang, K.; Abe, S.; Asano, S.; Ha, D.N. Susceptibility assessment of the precursor stage of a landslide threatening Haiwan Railway Station, Vietnam. *Landslides* **2018**, 15, 309–325. <https://doi.org/10.1007/s10346-017-0870-3>.
19. Ha, N.D.; Sayama, T.; Sassa, K.; Takara, K.; Uzuoka, R.; Dang, K.; Pham, T.V. A coupled hydrological-geotechnical framework for forecasting shallow landslide hazard—a case study in Halong City, Vietnam. *Landslides* **2020**, 17, 1619–1634. <https://doi.org/10.1007/s10346-020-01385-8>.
20. Tran, T.V.; Alvioli, M.; Hoang, V.H. Description of a complex, rainfall-induced landslide within a multi-stage three-dimensional model. *Nat. Hazards* **2022**, 110, 1953–1968. <https://doi.org/10.1007/s11069-021-05020-0>.
21. Hung, O. Numerical modelling of the motion of rapid, flow-like landslides for hazard assessment. *KSCE J. Civ. Eng.* **2009**, 13(4), 281–287. <https://doi.org/10.1007/s12205-009-0281-7>.
22. Liu, K.F.; Huang, M.C. Numerical simulation of debris flow with application on hazard area mapping. *Comput. Geosci.* **2006**, 10, 221–240.
23. Fischer, L.; Rubensdotter, L.; Sletten, K.; Stalsberg, K.; Horton, P.; Jaboyedoff, M. Debris flow modeling for susceptibility mapping at regional to national scale in Norway. In Proceedings of the 11th International and 2nd North American Symposium on Landslides, Banff, Alberta, Canada. 2012, pp. 723–729.
24. Blahut, J.; Horton, P.; Sterlacchini, S.; Jaboyedoff, M. Debris flow hazard modelling on medium scale: Valtellina di Tirano, Italy. *Nat. Hazards. Earth. Syst. Sci.* **2010**, 10(11), 2379–2390. doi:10.5194/nhess-10-2379-2010.
25. Castellanos, A.E.A.; Westen, C.J. Generation of a landslide risk index map for Cuba using spatial multi-criteria evaluation. *Landslides J. Int. Consortium Landslides* **2007**, 4, 311–325.
26. Technical Assistance on Geo-Information Technology for Hazard Risk Assessment – GITHRA. Twente University, 2010.
27. Castellanos, E.A. Multi - scale landslide risk assessment in Cuba. PhD Dissertation, ITC and University of Utrecht, 2008.
28. Horton, P.; Jaboyedoff, M.; Rudaz, B.; Zimmermann, M. Flow-R, a model for susceptibility mapping of debris flows and other gravitational hazards at a regional scale. *Nat. Hazards. Earth. Syst. Sci.* **2013**, 13, 869–885. doi:10.5194/nhess-13-869-2013.
29. Online available: <https://www.flow-r.org/home>

30. Online available: www.thanhhoa.gov.vn.
31. Jenks, G.F. The Data Model Concept in Statistical Mapping. *International Yearbook of Cartography*, 1967, 7, 186–190.
32. Ha, N.D. Design and construct a unified, inter-sectoral big data system to serve the early warning of landslides, flash floods events in real-time within the mountainous and midland regions of Vietnam. The research report presents the outcomes achieved in Phase II/2022 with the code TNMT.2021.04.07, conducted by the Viet Nam Institute of Geological Sciences and Mineral Resources in Hanoi, 2022.
33. Son, P.V. Establishing a scientific foundation and proposing regulations for managing geohazard, environmental geology investigative activities, monitoring, and warnings. The research report presents the outcomes achieved in Phase I/2022 with the code TNMT.2022.01.33, conducted by the Viet Nam Institute of Geological Sciences and Mineral Resources, 2022.

The barotropic simulation of coastal current in Soc Trang derived from a hydraulic model in curvilinear coordinates

Kim Tran Thi¹, Huy Dinh Ngoc¹, Huy Nguyen Dam Quoc², Phuoc Nguyen Van³, Phung Nguyen Ky¹, and Bay Nguyen Thi^{4,5*}

¹ Faculty of Marine Resource Management, Ho Chi Minh City University of Natural Resources and Environment, Vietnam; ttkim@hcmunre.edu.vn; kyphungng@gmail.com; huyspb@gmail.com

² Institute of Coastal and Offshore Engineering, Vietnam, 658 Vo Van Kiet, Ward 1, District 5, Ho Chi Minh City, Vietnam; damquochuy71@gmail.com

³ Ho Chi Minh City Union of Science and Technology Associations, 224 Dien Bien Phu, Ward 7, District 3, Ho Chi Minh City Vietnam; nvphuoc196@gmail.com

⁴ Department of Fluid Mechanics, Ho Chi Minh City University of Technology, Vietnam, 268 Ly Thuong Kiet Street, Ward 14, District 10, Ho Chi Minh City, Vietnam; ntbay@hcmut.edu.vn

⁵ Vietnam National University Ho Chi Minh City, Vietnam, Linh Trung Ward, Thu Duc District, Ho Chi Minh City, Vietnam; ntbay@hcmut.edu.vn

*Corresponding author: ntbay@hcmut.edu.vn; Tel.: +84–902698585

Received: 18 April 2023; Accepted: 26 June 2023; Published: 25 September 2023

Abstract: The coastal current plays a vital role in the transportation of sediment near the shoreline, significantly impacting the distribution of sediment grain sizes and shoreline transformations. This study focuses on examining the near-shore coastal current along the Soc Trang Province coast in Vietnam, considering the combined influences of waves, winds, and tides by utilizing a model in curvilinear coordinate system. Rigorous calibration and validation of the model are conducted using data obtained from measurement stations, revealing a consistent correlation between the observed data and simulated results. The direction of the coastal current, governed by the interplay of waves and winds, exhibits variation according to the monsoon season. During the northeast monsoon, the flow velocity is notably influenced, surpassing the impact of the southwest monsoon. In the northeast monsoon season, the tidal currents from the northeast to southwest align with the wave-induced current, resulting in an amplified coastal current during both spring tide (3-5%) and neap tide (2-5%). Conversely, in the southwest monsoon season, the tidal currents and wave-induced current move in opposing directions, leading to a reduction in coastal current velocities during high tide (3-4%) and low tide (3-4.5%). On the other hand, the impact of wind-induced current is negligible due to the small and low-lying nature of these areas, thereby minimizing the influence of wind on the overall flow dynamics.

Keywords: Coastal current; Hydraulic model; Tidal current; Wave induced current; Wind induced current.

1. Introduction

The near-shore estuary and coastal environment exhibit intricate natural processes influenced by tides, waves, currents, saline water, and their interplay. Investigating the coastal current within such areas serves as a foundational step for future studies involving sediment transport, shoreline accretion and erosion, coastal protection strategies, port and

harbor design, navigation, flood prediction, coastal erosion mitigation, and changes in the continental shelf seabed. By understanding the dynamics of coastal currents, we gain valuable insights into the complex mechanisms shaping these environments, enabling us to make informed decisions and develop effective solutions for coastal management and sustainable development [1–2]. Furthermore, the coastal current significantly influences the process of saline intrusion, particularly in the context of climate change and rising sea levels [3]. As the current is influenced by a combination of factors including waves, wind, and tides, many studies on coastal currents tend to concentrate on examining one of these factors individually.

In recent years, hydraulic models like TELEMAC have been extensively utilized for studying hydraulic features in rivers, estuaries, coastal areas, and oceans [4–5]. Numerical simulations using these models have proven to be highly valuable and cost-effective tools for enhancing our understanding of these phenomena. Research in this field often involves the use of shallow water equations (SWE) or the application of the finite-volume primitive equation Community Ocean Model (FVCOM) [6]. The SWE, initially proposed by Saint-Venant in 1871 to simulate flow in open channels [7–8], has been widely employed for describing shallow water flows. It can be derived as a simplification of the Navier–Stokes equation through vertical dimension averaging [9]. Two-dimensional numerical models commonly used for near-shore hydrodynamics include the CCHE2D hydraulic model, developed by Jia and Wang in 1999 [10]; However, the shear stress terms at the water surface were not considered in the 2001 version of this model [11]. The CCHE2D model, created by Mississippi State University, aims to simulate hydraulic transmission, water quality, sediment transport, and riverbed fluctuations [12]. Another notable model is TELEMAC, developed in 1987 by the French National Hydraulic and Environment Laboratory (<http://www.opentelemac.org/>). TELEMAC is a powerful integrated modeling tool capable of handling 1D, 2D, and 3D flows. The model employs flexible meshing and finite-element numerical schemes. Modules such as TELEMAC2D/3D and SISYPHE are used to simulate flow, sediment transport, and bottom evolution [5]. A widely used commercial software, MIKE 21, was developed by the Danish Hydraulic Institute (DHI) for simulating various flow features in creeks, rivers, lakes, estuaries, bays, and coastal areas [13]. The software comes in two versions: classic and flexible mesh (FM). The FM version utilizes a triangulated and unstructured mesh, offering improved resolution within the study domain [14]. Moreover, the MIKE 21C model employs curvilinear finite difference grids to predict hydraulic and morphological changes in two dimensions, optimizing results near land boundaries [15]. Most current modeling approaches employ structured curvilinear systems or unstructured triangular assemblies for mesh generation. While the unstructured approach provides greater flexibility in shape, the resulting model outputs may be less accurate due to the stretching of triangular grid cells in the current direction [16–17]. In contrast, curvilinear grid cells provide more accurate model outputs by closely aligning with land boundaries, especially in areas with complex bathymetry. When curvilinear coordinates are used, the velocity in the ξ direction (a coordinate direction in the curvilinear system) resulting from complex bathymetry is fully accounted for within the model through the Cartesian coordinate system. Hence, simulation results based on curvilinear coordinates tend to be superior to those based on the Cartesian coordinate system in areas with complex bathymetry [18–20].

Soc Trang, a coastal province located in the Mekong Delta, covers an area of 3311.87 km² and is home to approximately 1.3 million residents. Situated in the estuary region of the Hau River, a major tributary of the Mekong River, the northeastern part of the province is bounded by the Hau River, while the southeastern region is adjacent to the sea [21]. The study area experiences a tropical monsoon climate characterized by two distinct seasons: the flood season (May to October) and the drought season (November to April). River flow

and tidal currents exert a significant influence on the area, with the tides being of mixed semidiurnal and diurnal nature and displaying pronounced diurnal inequality [22–23]. The Tra Vinh - Soc Trang coast in the Mekong Delta is characterized by the presence of a tidal beach with multiple intertidal bars, shaped by the interaction of waves and tides [24]. While the coastal current in Soc Trang Province is only minimally influenced by wind-affected and wave-induced currents, these factors play a crucial role in shaping sediment transport patterns and the geomorphological evolution of the coastline [24]. Hydraulic processes at the river mouths are heavily influenced by both river discharges and monsoons [24–25]. The study of [25] has demonstrated that the direction of suspended sediment movement depends on the prevailing monsoon direction. The coastal estuarine area in the Mekong Delta has undergone complex changes in its hydraulic regime due to climate change and upstream development [26]. The coast of Soc Trang has been extensively studied regarding the contribution of natural hydrodynamic sediment redistribution and erosion caused by human activities [25, 27–30]. Notably, a three-dimensional hydrodynamic redistribution model has been proposed to account for sediment movement from land, rivers, and other sources. This model incorporates calibration based on a combination of observations, laboratory experiments, and satellite analysis. The study by [27] provides a brief illustration of wind-induced and wave-induced currents in the area. However, in-depth studies on the impacts of factors such as waves, wind, and tides on coastal current are still limited. With the strong occurrence of erosion (instead of deposition as before) and the influence of climate change, evaluating the effects of each factor is a prerequisite for studying sediment transport along the coast, the dynamics of erosion and deposition, as well as coastal management at the local area.

This study utilized a numerical model to simulate the coastal current in the Soc Trang area, considering the influential factors of wind and tides on waves. The model employed in this study was developed by [31] and is based on the depth-integrated 2D Reynolds equation in Cartesian coordinates. This model serves as a fundamental tool for assessing and managing coastal protection and risk reduction measures in the region. By implementing a curved coordinate system, the numerical model effectively minimizes errors in areas with complex shorelines. Additionally, the use of an open-source model facilitates the enhancement of monitoring and early warning systems, as it allows for convenient code implementation and further development.

2. Materials and Methods

2.1. Study area

To mitigate the impact of boundary condition errors, the study area was expanded to encompass the sea area stretching from Vung Tau to Ganh Hao in Vietnam. The geographical coordinates of this expanded area range from 302993 to 1085665 east and 797766 to 1328835 north (Figure 1a). This extended study area includes the coastal region of Soc Trang Province along with neighboring provinces. It spans approximately 300 km in length and has a width of approximately 160 km, extending from the shoreline into the sea.

2.2. Data collection

The topographic data used in this study were obtained from the East Sea's topography in 2010, collected and extracted by the Southern Institute of Water Resources Science, Vietnam (SIWRR). A calculating grid was constructed using an orthogonal curved grid format, comprising 130×155 cells. The grid size varied between 150 meters and 300 meters, with dx and dy representing the cell dimensions (Figure 1) [31].

The tidal harmonic constants, including the amplitudes and phases of each tidal constituent, were obtained from the DTU10 Global Tide Model. The data used had a

resolution of $0.125^\circ \times 0.125^\circ$ and were extracted specifically for the three open boundaries at sea, namely the left, right, and sea boundaries, as depicted in Figure 1.

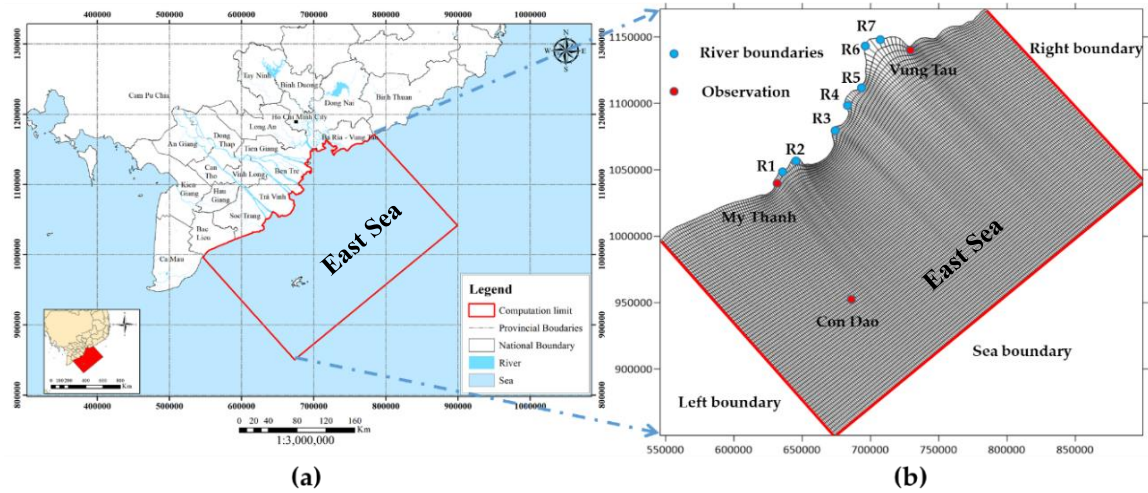


Figure 1. Study area.

To validate the model, hourly water level data from the Vung Tau, Con Dao, and My Thanh stations were collected from the Southern Regional Hydrometeorological Station in 2017. These water level measurements were utilized to verify the accuracy of the model's predictions, in detailed: the water levels from 1:00 am on 01 January 2017 to 1:00 am on February 28, 2017, at Con Dao, from 10:00 am on January 15, 2017, to 10:00 pm on February 14, 2017 at My Thanh station, and from 1:00 a.m. on January 1, 2017, to 10:00 p.m. on February 28, 2017 at Vung Tau station.

Wind data: Wind velocity with a spatial resolution of 0.5 degrees and temporal resolution of 3 hours were collected from <https://cds.climate.copernicus.eu> /from 0:00 am on 01 January 2017 to 23 December 2017.

Wave data: S_{xx} , S_{xy} , S_{yy} stress fields were simulated from the Mike 21SW model from 0:00 am on 01 January 2017 to 23 December 2017, extracted from [32].

2.3. Numerical model description

The governing equations in the curvilinear coordinates (HyCCM Model) are constructed based on the Reynolds equation depth-integrated 2D in Cartesian coordinates [31]. In the 2D model, the vertical velocity component is so small that it is ignored, and the pressure is approximated as the hydrostatic pressure distribution. In previous studies, the nonlinear, Coriolis, friction bed components have been solved in curvilinear coordinate systems. In this study, the two components of wave and wind friction are constructed in a curvilinear coordinate system, as described in Equation 1 [31].

$$\begin{cases} p_\tau + gHJ^{-1}(g_{22}\zeta_\xi - g_{12}\zeta_\eta) = \Psi_1 \\ q_\tau + gHJ^{-1}(g_{11}\zeta_\eta - g_{12}\zeta_\xi) = \Psi_2 \\ JH_\tau + p_\xi + q_\eta = 0 \end{cases} \quad (1)$$

where ξ , η are space coordinates (m).

$$\begin{aligned} \Psi_1 &= \Psi_{a1} + \Psi_{T1} + \Psi_{k1} + \Psi_{S1} + \Psi_{W1} \\ \Psi_2 &= \Psi_{a2} + \Psi_{T2} + \Psi_{k2} + \Psi_{S2} + \Psi_{W2} \end{aligned} \quad (2)$$

where $\tau = t$ is time (s); $p = JUH$ is the ξ component of velocity; $q = JVH$ is the η component of velocity; $H = h + \zeta$; ζ is the fluctuation of the water surface (m); h is the static depth from the still water surface to the bed (m); Ψ_{a1} and Ψ_{a2} are the ξ and η components of nonlinear [31]; $\Psi_{\tau 1}$, and $\Psi_{\tau 2}$ are the ξ and η components of friction bed

[31]; Ψ_{k1} , and Ψ_{k2} are the ξ and η components of Coriolis [31]; Ψ_{s1} , and Ψ_{s2} , the ξ and η components of wind friction, are calculated as Equations 4-5.

$$\Psi_{S1} = \left[\frac{1}{\rho} C_{10} \rho_a |W| (W_x y_\eta - W_y x_\eta) \right] \quad (4)$$

$$\Psi_{S2} = \left[\frac{1}{\rho} C_{10} \rho_a |W| (W_x x_\xi - W_y y_\xi) \right] \quad (5)$$

$$\text{with } C_{10} = (0.75 + 0.067|W|) \cdot 10^{-3} \quad (6)$$

where W is wind velocity (m/s); ρ_a is the density of air above the sea surface [kg/m^3]; W_x and W_y are the x and y components of wind velocity (m/s), respectively; Ψ_{w1} , and Ψ_{w2} , the ξ and η components of wave friction, are calculated as Equation 7 and Equation 8.

$$\Psi_{W1} = - \left[\frac{I^{-1}}{\rho} (S_{1\xi}(y_\eta y_\eta - y_\eta x_\eta) + S_{1\eta}(y_\xi x_\eta - y_\xi y_\eta) + S_{3\eta}(x_\xi y_\eta - x_\xi x_\eta) + S_{3\xi}(x_\eta x_\eta - x_\eta y_\eta) + (S_{2\xi} g_{22} - S_{2\eta} g_{12})) \right] \quad (7)$$

$$\Psi_{W2} = - \left[\frac{I^{-1}}{\rho} (S_{1\xi}(y_\eta x_\xi - y_\eta y_\xi) + S_{1\eta}(y_\xi y_\xi - y_\xi x_\xi) + S_{3\eta}(x_\xi x_\xi - x_\xi y_\xi) + S_{3\xi}(x_\eta y_\xi - x_\eta x_\xi) + (S_{2\eta} g_{11} - S_{2\xi} g_{12})) \right] \quad (8)$$

$S_1 = S_{xx}$; $S_2 = S_{xy} = S_{yx}$; $S_3 = S_{yy}$ are the x and y components of effective shear stress.

U and V are defined as the ‘‘contravariant’’ base vectors of the curvilinear coordinate system.

The system of Eq. 1 is solved using the alternating direction implicit (ADI) method on the C-Arakawa grid. The mesh nodes are located on the boundary where the velocity component is perpendicular to the boundary. In the algorithm, the water level is simulated using the implicit diagram, employing the semi-implicit ‘‘gradient’’ method. On the other hand, the nonlinear component is solved using an explicit diagram. This combination of implicit and explicit schemes helps in efficiently and accurately modeling the water level and accounting for the nonlinearities in the system [31].

2.4. Model setup

Open boundaries

Water level: water level ζ of 8 tidal constitutions K_1 , O_1 , P_1 , Q_1 , M_2 , S_2 , N_2 and K_2 at three open boundaries at sea (left, right and sea boundaries as Figure 1) are calculated from sigma (σ), amplitude (A), phase (g^0) and period (t), as illustrated in Equation 9:

$$\zeta = A \times \cos(\sigma t - g^0) \quad (9)$$

Sigma (σ) and period (t) are defined in [31], while the amplitude and phase of each tidal constitution are extracted from the DTU10 Global Tide Model at three open boundaries at sea.

River boundaries in estuaries (R_1 , R_2 , R_3 , R_4 , R_5 , R_6 , and R_7 as Figure 1) are discharged and extracted from [33–34].

The stress fields S_{xx} , S_{xy} , and S_{yy} in 2017 are simulated from the Mike 21SW model and extracted from [32].

Wind data: Wind velocity with a resolution of 0.5 degrees, W_x , W_y wind data are obtained from there-analyzed wind data of <https://cds.climate.copernicus.eu/> in 2017.

Land boundary: $u_n = 0$, where n stands for the normal direction.

Initial conditions: the velocity components p and q are zero, and sea level is zero.

The scenarios: four scenarios are simulated in the study:

Cases with wind induced current: these cases simulate only the flow under the influence of wind (use only wind boundaries).

Cases with wave induced current: these cases simulate only the flow under the influence of waves (use only wave boundaries).

Cases with tidal currents: these cases simulate only the flow under the influence of tidal current (use only tidal boundaries).

Coastal current: these cases simulate the flow under the influence of wind, waves, river flow and tidal currents.

The flow chart is illustrated as Figure 2.

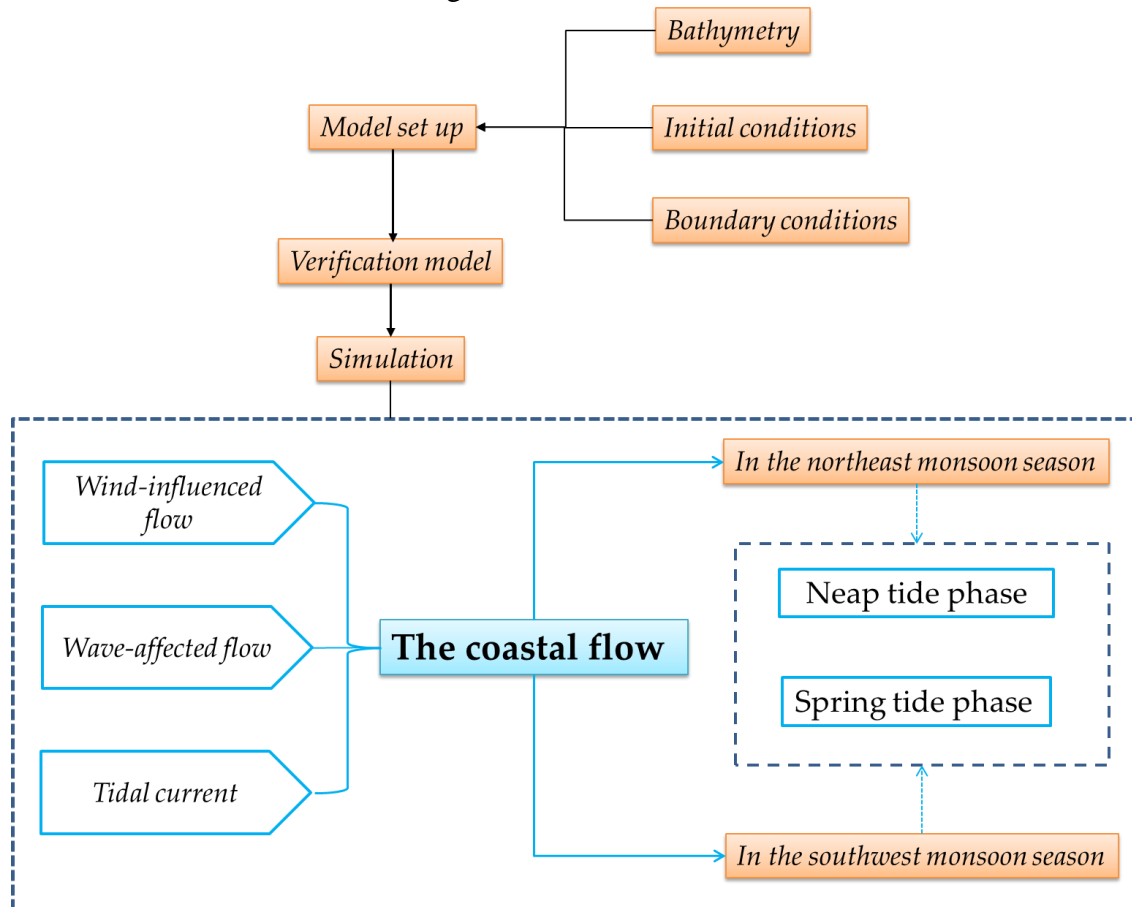


Figure 2. Flow chart of study structure.

2.5. Evaluation criteria

In this study, the Nash-Sutcliffe efficiency coefficient (NSE), the coefficient of determination (R^2) and root mean squared error (RMSE) are required to measure model performance.

The Nash-Sutcliffe efficiency coefficient (NSE)

The Nash-Sutcliffe efficiency coefficient (NSE) ranges between $-\infty$ and 1. $NSE = 1$ indicates a perfect match between the observed and predicted results [35]. NSE is computed as shown in Equation 1:

$$NSE = 1 - \left[\frac{\sum_{i=1}^n (O_i - P_i)^2}{\sum_{i=1}^n (O_i - \bar{O})^2} \right] \quad (10)$$

where O_i is the i^{th} observation for the constituent being evaluated; P_i is the i^{th} simulated value for the constituent being evaluated; \bar{O} is the mean of observed data for the constituent being evaluated; and n is the total number of observations.

The coefficient of determination (R^2)

For the coefficient of determination, R^2 ranges between 0 and 1 and describes the proportion of the variance in the measured data, with higher values indicating less error variance [36]. R^2 is computed as shown in Equation 11:

$$R^2 = \left[\frac{\sum_{i=1}^n (O_i - \bar{O})(P_i - \bar{P})}{\sqrt{\sum_{i=1}^n (O_i - \bar{O})^2 \sum_{i=1}^n (P_i - \bar{P})^2}} \right]^2 \quad (11)$$

where O_i is the i^{th} observation for the constituent being evaluated; P_i is the i^{th} simulated value for the constituent being evaluated; \bar{O} is the mean of observed data for the constituent being evaluated; \bar{P} is the mean of simulation data for the constituent being evaluated; and n is the total number of observations.

Root mean squared error (RMSE)

RMSE values smaller than 0.05 are considered a good fit, values from 0.05 to 0.08 are considered a fair model fit, and values greater than 0.10 are considered a poor fit [38].

$$RMSE = \sqrt{\frac{1}{n} \sum_{i=1}^n (P_i - O_i)^2} \quad (12)$$

where O_i is the i^{th} observation for the constituent being evaluated; P_i is the i^{th} simulated value for the constituent being evaluated; and n is the total number of observations.

3. Results

3.1. Model verification

In the area, the water levels at Con Dao from 1:00 am on 01 January 2017 to 1:00 am on February 28, 2017, at My Thanh station from 10:00 am on January 15, 2017, to 10:00 pm on February 14, 2017, and at Vung Tau station from 1:00 a.m. on January 1, 2017, to 10:00 p.m. on February 28, 2017, are used to verify the model. Three criteria for model performance evaluation include NSE, R^2 and RMSE.

The water level simulations at the three stations show a high agreement between the observed and simulated data in terms of phase and amplitude. The water level comparison between the observations and simulations at Con Dao is better than the results at the My Thanh and Vung Tau stations, with $R^2 = 0.85$, $NSE = 0.83$ and $RMSE = 0.011$ (Figure 3a). While the comparison result in My Thanh is a fair model fit, with $R^2 = 0.78$, $NSE = 0.65$ and $RMSE = 0.053$ (Figure 3b), these values in Vung Tau are lower, at $R^2 = 0.73$, $NSE = 0.63$ and $RMSE = 0.061$ (Figure 3c). The lower water level simulation compared to observations may be caused by the baroclinic effects that were not set up in the model.

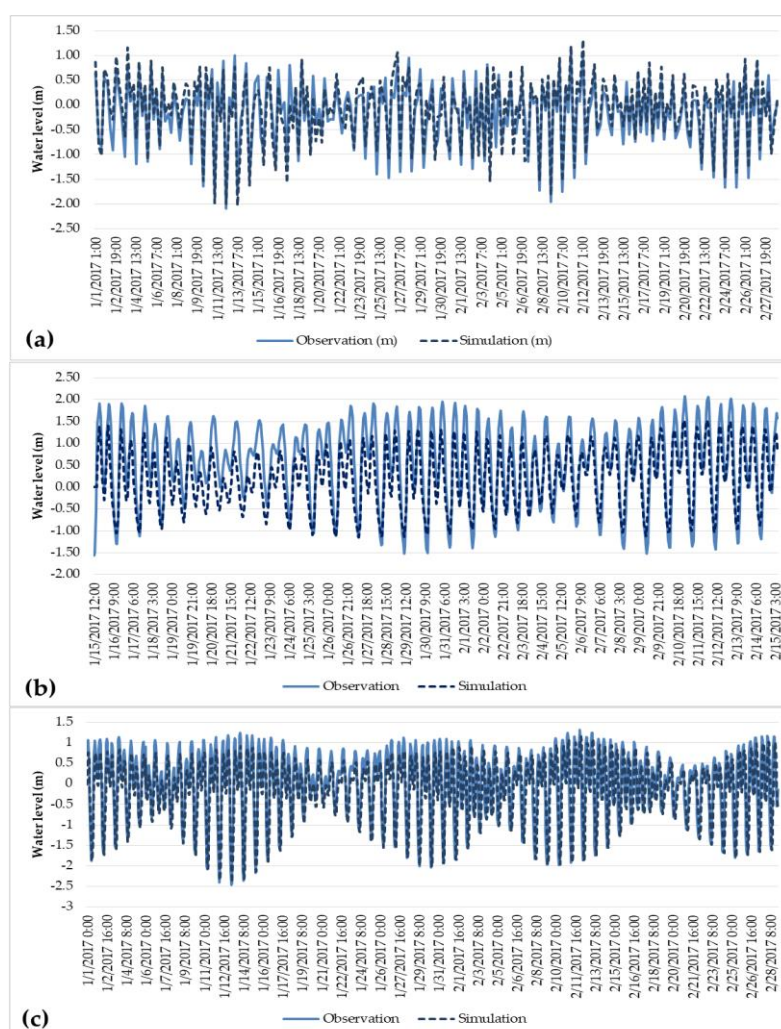


Figure 3. Water level comparison between observation and simulation at Con Dao (a), My Thanh (b) and Vung Tau (c).

The discrepancy in amplitude can be attributed to the water level data obtained from the model for the eight tidal constituents K_1 , O_1 , P_1 , Q_1 , M_2 , S_2 , N_2 and K_2 . While there is a difference in amplitude between the model's data and the observed data, the phase of the water level demonstrates strong consistency. This indicates that these eight tidal constituents exert significant influence in the study area, despite the slight variation in their amplitudes.

After model verification, the roughness coefficient exhibits variability with depth, ranging from 0.026 to 0.058 ($m^{1/3}/s$) as illustrated in Figure 4. The roughness coefficient serves as a measure of the resistance to flow caused by the irregularities of the channel bed and banks. In this case, the coefficient values demonstrate a range of roughness characteristics across different depths within the study area.

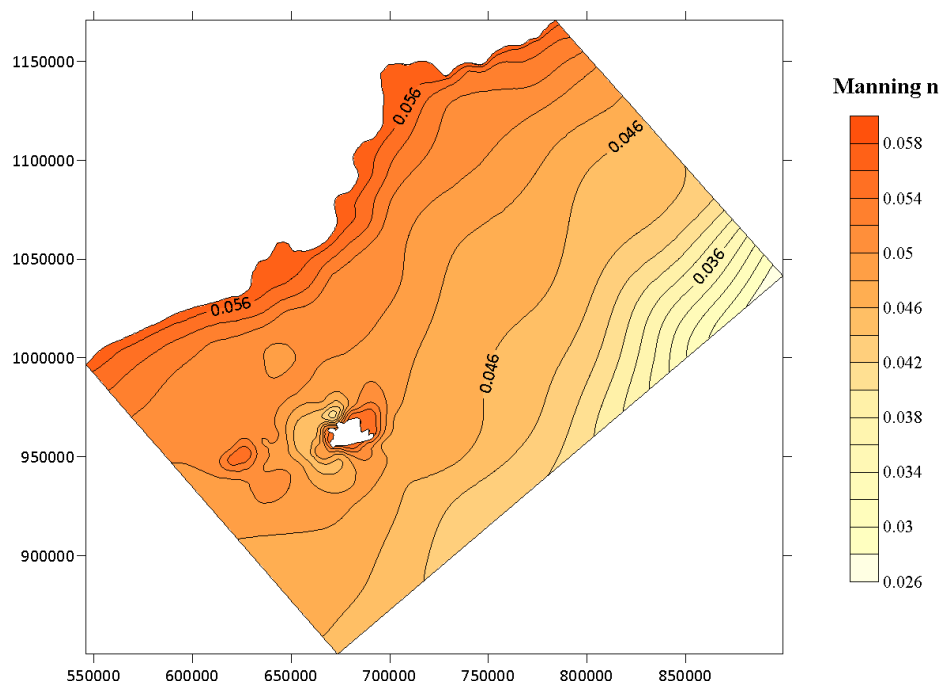


Figure 4. The roughness coefficient map.

3.2. Simulation results of the seasonal flow of the northeast and southwest monsoons

3.2.1. Case with wind induced current

During the northeast monsoon season (November to early March 2017), the simulation results indicate the presence of wind-induced current along the coast, predominantly flowing in a northeast direction. The current velocity in the Soc Trang coastal area is relatively higher and larger compared to other areas, reaching approximately 2.5 cm/s. In contrast, the near-shore area experiences lower current velocities due to the influence of topography and increased bottom friction.

In the Hau Estuaries area, the influence of the northeast wind on the flow is minimal due to the small size and low-lying nature of these areas. The flow velocity in area (a) (Dinh An Estuary) ranges from approximately 0.45 to 0.85 cm/s, while in area (b) (Tran De Estuary), it varies from 0.46 to 0.94 cm/s. Comparatively, the near-shore area (c) exhibits the highest flow velocities among the three areas, ranging from 1.22 to 1.64 cm/s. Additionally, the water level fluctuations in the area gradually increase in the direction of the wind.

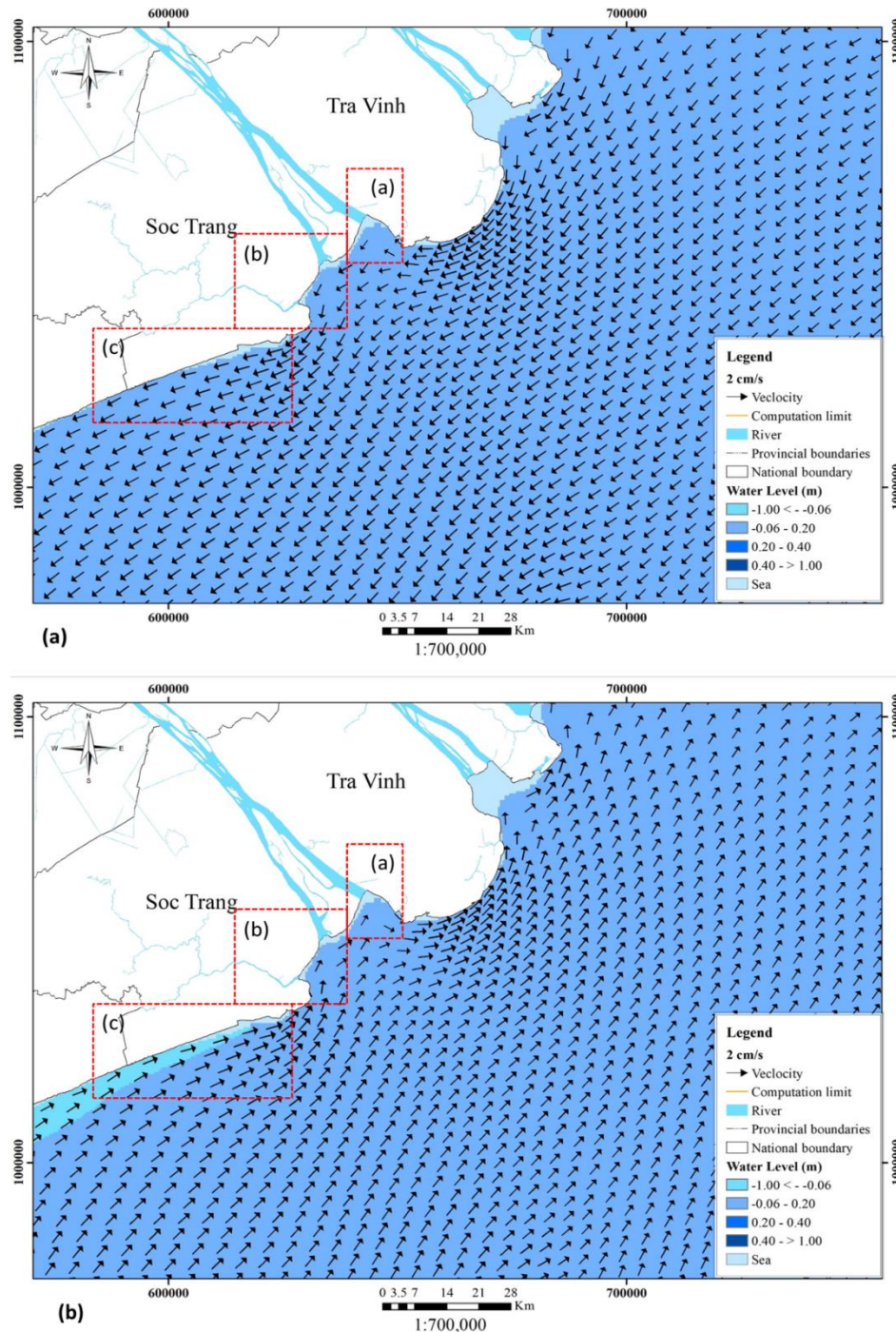


Figure 5. (a) Simulation results of wind induced current in the northeast monsoon season at 15:00 on 25 February 2017; (b) Simulation results of wind induced current in the southwest monsoon season at 9:00 on 26 September 2017.

During the southwest monsoon season (June to early October 2017), the simulation results show a wind-induced current in the study area flowing along the shore in a southwest direction (Figure 5b). The overall flow velocity in the region is relatively small compared to the northeast monsoon season. In the Soc Trang coastal area, the current flow velocity is approximately 2 cm/s (Figure 5b), while in the coastal area, it is slightly smaller.

In the estuary area, the influence of the southwest wind is limited. The flow velocity in area (a) ranges from approximately 0.4 to 0.74 cm/s, in area (b) from 0.42 to 0.82 cm/s, and in area (c) from 1.1 to 1.53 cm/s (Figure 5b). These velocities indicate relatively lower flow rates compared to the coastal and near-shore areas.

3.2.2. Case with wave induced current

The simulation results show the presence of wave-induced currents along the shore in the northeast direction. These currents are formed in the breaking wave zone, where the waves approaching the coastal area undergo dumping and uneven distribution due to shallow water depths and inhomogeneous bottom topography (with water depth being only approximately 1.3 times the wave height). This uneven distribution of waves creates different wave stress fields, and when a wave breaks, the wave energy transforms into a force that moves the water mass, generating shoreline currents.

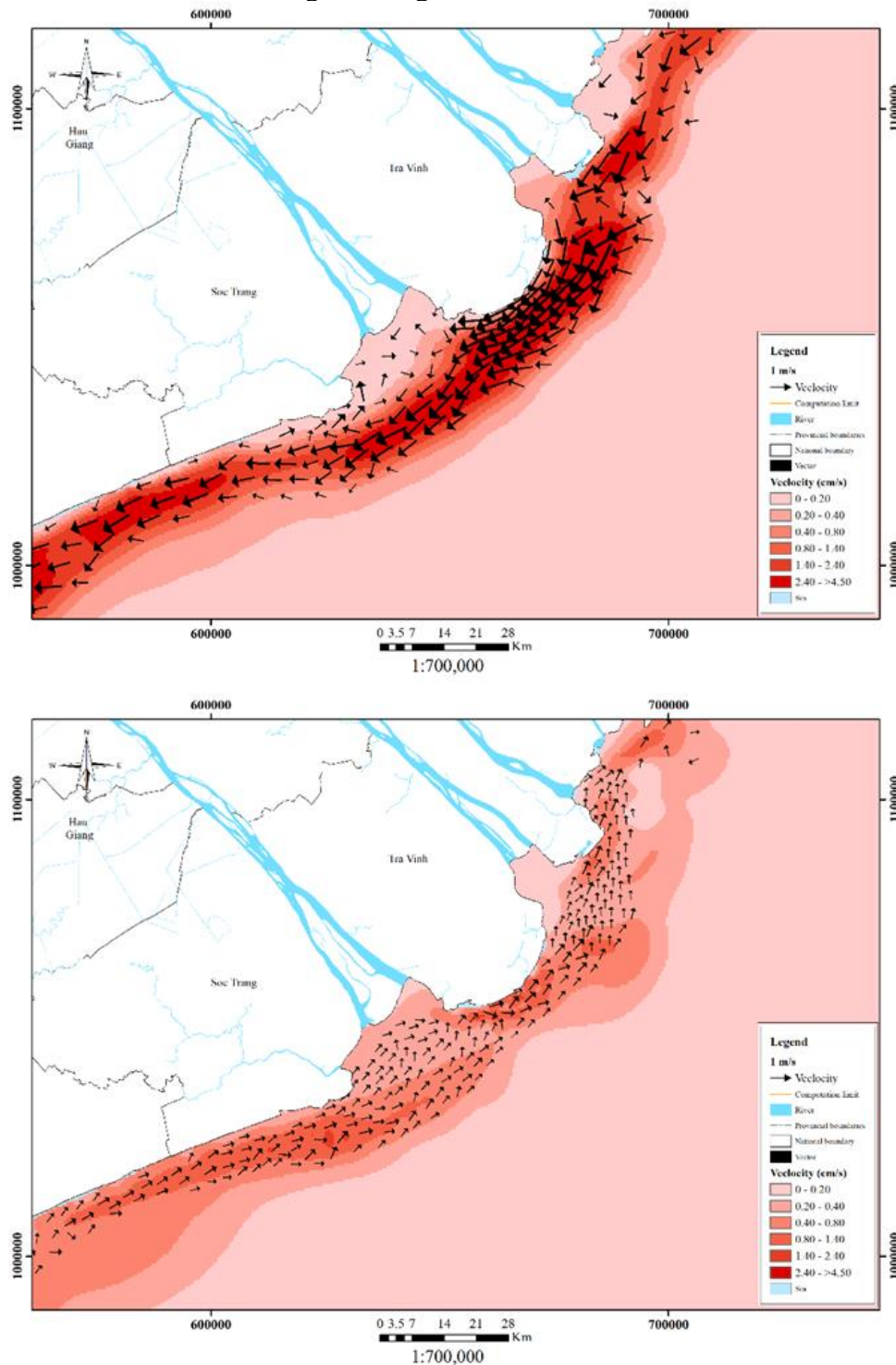


Figure 6. (a) Simulation results of wave induced current in the northeast monsoon season at 15:00 on 25 February 2017; (b) Simulation results of wave effects in the southwest monsoon season at 9:00 on 26 September 2017.

The wave induced current, although relatively small compared to other factors, plays a role in the distribution of suspended sediment in the area. When considering only the flow influenced by waves, the wave-induced current has a width of approximately 6-7 m parallel to the shoreline, primarily located in the breaking wave zone. Specifically, around Con Dao, the width of the wave-induced current is only 3-4 m. The maximum velocity in the near-shore area is around 3.2-5 cm/s in area (c). However, the velocity in the Hau River estuary is significantly smaller. In the Dinh An Estuary (area (a)), the velocity ranges from 0.75-1.5 cm/s, while in the Tran De Estuary (area (b)), it is slightly higher, ranging from 0.78-1.9 cm/s (Figure 6a). The narrow topography and large bottom friction in the river mouth areas minimize the influence of waves on the flow dynamics.

During the southwest monsoon season (July to early October 2017), the simulation results show that the wave-induced current in the area primarily flows in the southwest direction. However, the wave-induced current in the southwest monsoon season is generally weaker than that in the northeast monsoon season.

At the mouth of the Hau River, there are vortices with insignificant velocity, approximately 0.2 cm/s in area A. The maximum velocity of the wave-induced current is only 3.6 cm/s in the coastal section of Soc Trang Province (area (c)). Compared to the northeast monsoon season, the coastal current has a lower velocity during the southwest monsoon (Figure 6b). There is no significant difference in the simulation results of the flow velocity in the Dinh An and Tran De estuaries, with ranges of 0.5-1.2 cm/s and 0.52-1.3 cm/s, respectively (in areas (a) and (b) in Figure 6b).

Overall, the simulation results demonstrate that the offshore velocity is small, but as the waves approach the breaking wave area, the velocity increases. The maximum velocity is reached at the breaking point and then decreases abruptly as the waves approach the shore. The wave direction in the area, influenced by the monsoon seasons, plays a significant role. During the northeast monsoon, the wave direction is northeasterly, while during the southwest monsoon, it is southwesterly. These directional changes are consistent with previous studies on the South China Sea area [24, 39–41]. To fully consider the contribution of coastal currents to regional flows, it is essential to consider the overall influence of wind-wave factors, river currents, and tidal currents.

3.2.3. Case with tidal currents

In the study area, the tidal currents generally follow the direction of tidal currents in the East Sea. The dominant tide in the area is irregular semidiurnal, and the tidal range, which is the difference between high tide and low tide, ranges from 2 m to 4 m during the day [24, 42]. The flow velocities during the spring tide and neap tide phases were extracted at 13:00 and 19:00 on 15 February 2017, respectively.

During the spring tide phase (Figure 7a), the tidal current flows in the northeast direction from the East Sea towards the estuaries. The highest velocity, reaching nearly 1 m/s, is observed at the river mouth, while the overall velocity in the region is lower. The tidal current velocity close to the shore is negligible. In the Dinh An estuary (area (a)), the tidal current velocities range from 0.54 m/s to 0.96 m/s, while in the Tran De estuary (area (b)), they range from 0.4 m/s to 0.92 m/s. Comparatively, the study findings differ from [23], which analyzed the mean water surface slope and showed higher velocities in the Dinh An channel compared to the Tran De channel.

During the neap tide phase (Figure 7b), the difference between the tidal current velocities in the estuary and coastal area becomes more pronounced compared to the spring tide phase. The tidal current velocity in the Dinh An estuary ranges from 0.44 m/s to 0.92 m/s, and in the Tran De estuary, it ranges from 0.35 m/s to 0.9 m/s, which is approximately triple the velocity observed in the coastal area (0.2 m/s).

These results indicate that tidal current velocities vary with tidal phases, with higher velocities during spring tide and lower velocities during neap tide. The estuaries experience stronger tidal currents compared to the coastal area, with the Dinh An estuary generally exhibiting higher velocities than the Tran De estuary.

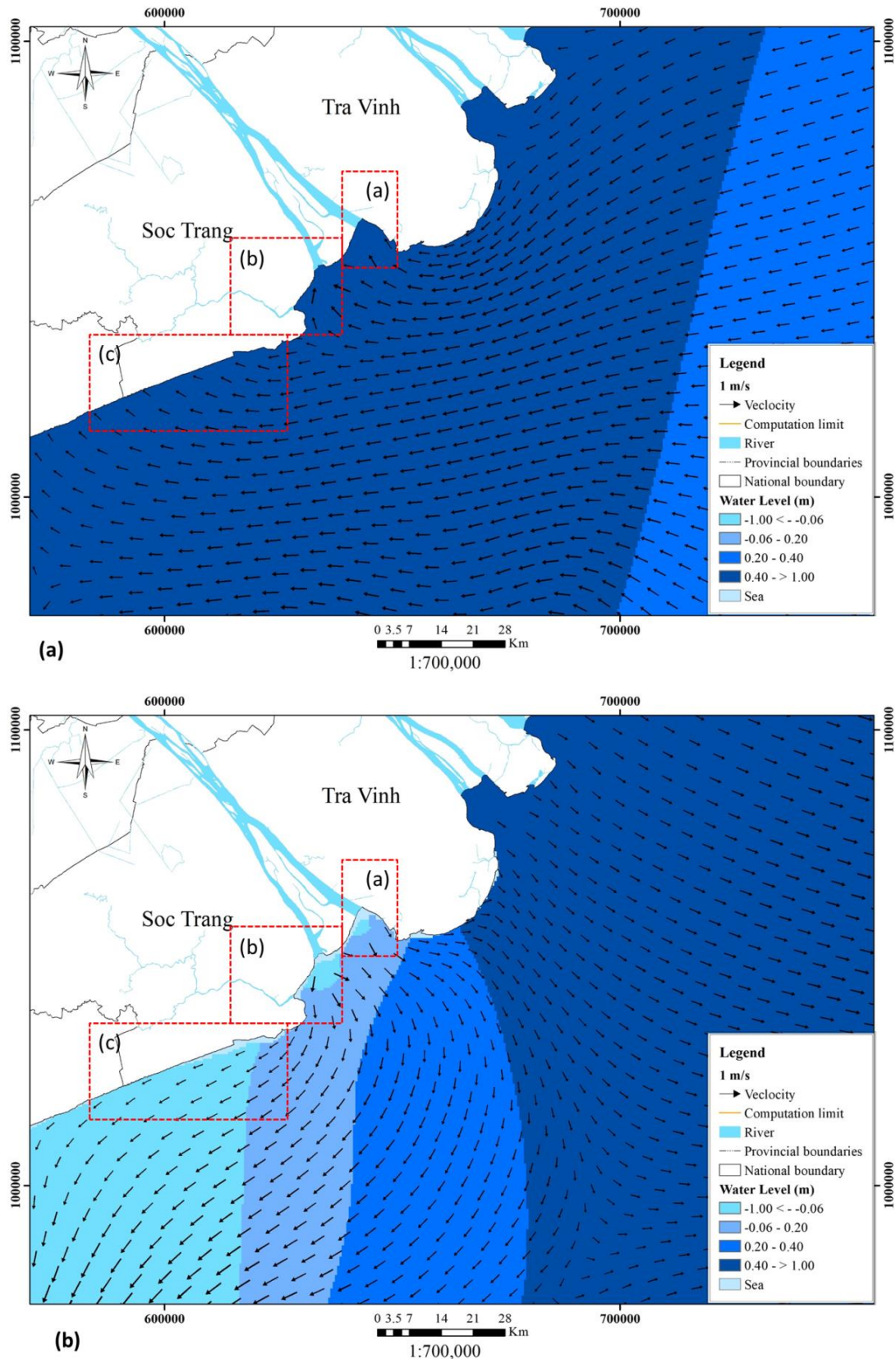


Figure 7. (a) Simulation results of the tidal current at spring tide at 13:00 on 15 February 2017; (b) Simulation results of the tidal current at neap tide at 19:00 on 15 February 2017.

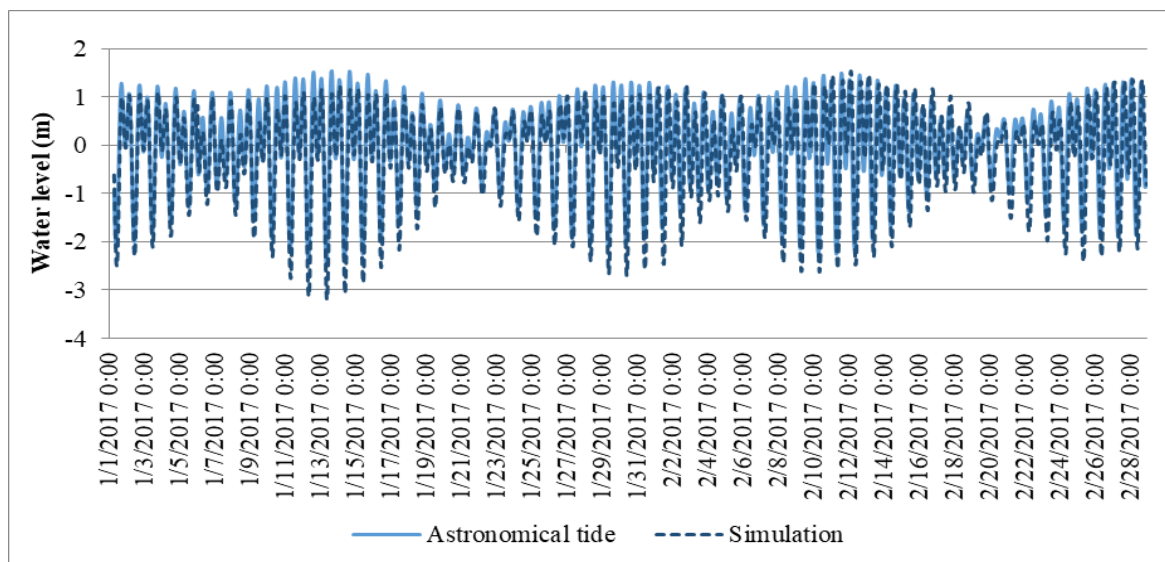


Figure 8. Water level comparison between astronomical tide and simulation at Vung Tau.

When comparing the results with the astronomical tide forecast at Vung Tau, considering only the influence of tides, the findings show a close match between the astronomical tide and the calculated results from the model, with $R^2 = 0.93$, $NSE = 0.91$ and $RMSE = 0.008$ (Figure 8). The calculation of these results is explained by the fact that the input data of the model include the extraction of the amplitude and phase of each tidal component from the DTU10 Global Tide Model.

3.2.4. Coastal current

During the northeast monsoon season, the coastal current in the study area is primarily influenced by tidal currents. The tidal currents flow from the northeast, which is the same direction as the wave induced current. This alignment leads to an increase in the coastal current during both the spring tide and neap tide phases.

During the spring tide phase (Figure 9a), the coastal current experiences an approximate increase of 3-5%. Similarly, during the neap tide phase (Figure 9b), the coastal current sees an increase of approximately 2-5%. These increases in coastal currents are attributed to the combined effects of tidal currents and wave induced currents. The influence of wind on the study area is considered insignificant in comparison.

The maximum velocity recorded in the Dinh An Estuary during the spring tide phase is 1.08 m/s, and during the neap tide phase, it is 1.12 m/s (areas (a) and (b) in Figure 9a and 9b). In the Tran De Estuary, the maximum velocity is slightly lower, measuring 0.92 m/s during the spring tide phase and 0.94 m/s during the neap tide phase (areas (a) and (b) in Figures 9a, 9b).

Therefore, in the northeast monsoon season, the coastal current in the study area is primarily driven by tidal currents, with some contribution from wave induced currents, while wind has minimal influence on the coastal current dynamics. The velocity of the neap tide in these estuaries is higher than that of the spring tide due to river discharge. The discharge in the Dinh An Estuary is 33.48 m³/s in the spring tide and is -33.79 m³/s in the neap tide, while that in the Tran De Estuary is 20.63 m³/s in the spring tide and is -21.85 m³/s in the neap tide (Symbol “-” means flow direction in the neap tide).

Similarly, during the southwest monsoon season, the tidal current that flows from northeast to southwest has the opposite direction to the wave induced current (from southwest to northeast), leading to a decrease in the combined current at spring tide (3-4%) (Figure 9c) and at neap tide (3-4.5%) (Figure 9d).

During the spring tide phase, the tidal current from the East Sea (belong to South China Sea) flows toward the Mekong estuaries, creating two main tidal trends: tidal currents from the southwest and tidal currents from the northeast. When reaching the mouth of the Hau River, the northeast tidal current is phased earlier, resulting in a tendency for the flow to have a northeast direction when the tide rises in the southwest monsoon season. The eddies in the Hau estuary are caused by the interference of tidal currents and currents in the river. The maximum velocity in the Dinh An Estuary is 1.1 m/s in the spring tide phase, which is higher than that in Tran De Estuary, at 0.9 m/s (34.59 m³/s of discharge in Dinh An Estuary and 20.56 m³/s of discharge in Tran De Estuary) (Figure 9c).

During the neap tide phase, the value of coastal current velocity at locations in the southwest monsoon is mostly smaller than the flow in the northeast monsoon at the spring tide. However, there are some locations near the mouth of the Dinh An River where the value of the flow in the southwest monsoon is higher; during this season, the flood water from the river is greater, with peaks in late summer (August-September) [39]. The maximum velocity in the Dinh An Estuary is 1.14 m/s, which is higher than that in the Tran De Estuary, at 0.94 m/s (-34.76 m³/s of discharge in the Dinh An Estuary and -21.83 m³/s of discharge in the Tran De Estuary) (Figure 9d).

The coastal current results from the dominance of the wind, wave, river flow and tidal currents of the northeast monsoon, as the flow in the southwest monsoon is much weaker than that in the northeast monsoon. In the estuary, the river flow still dominates; the discharge from upstream greatly affects its flow velocity.

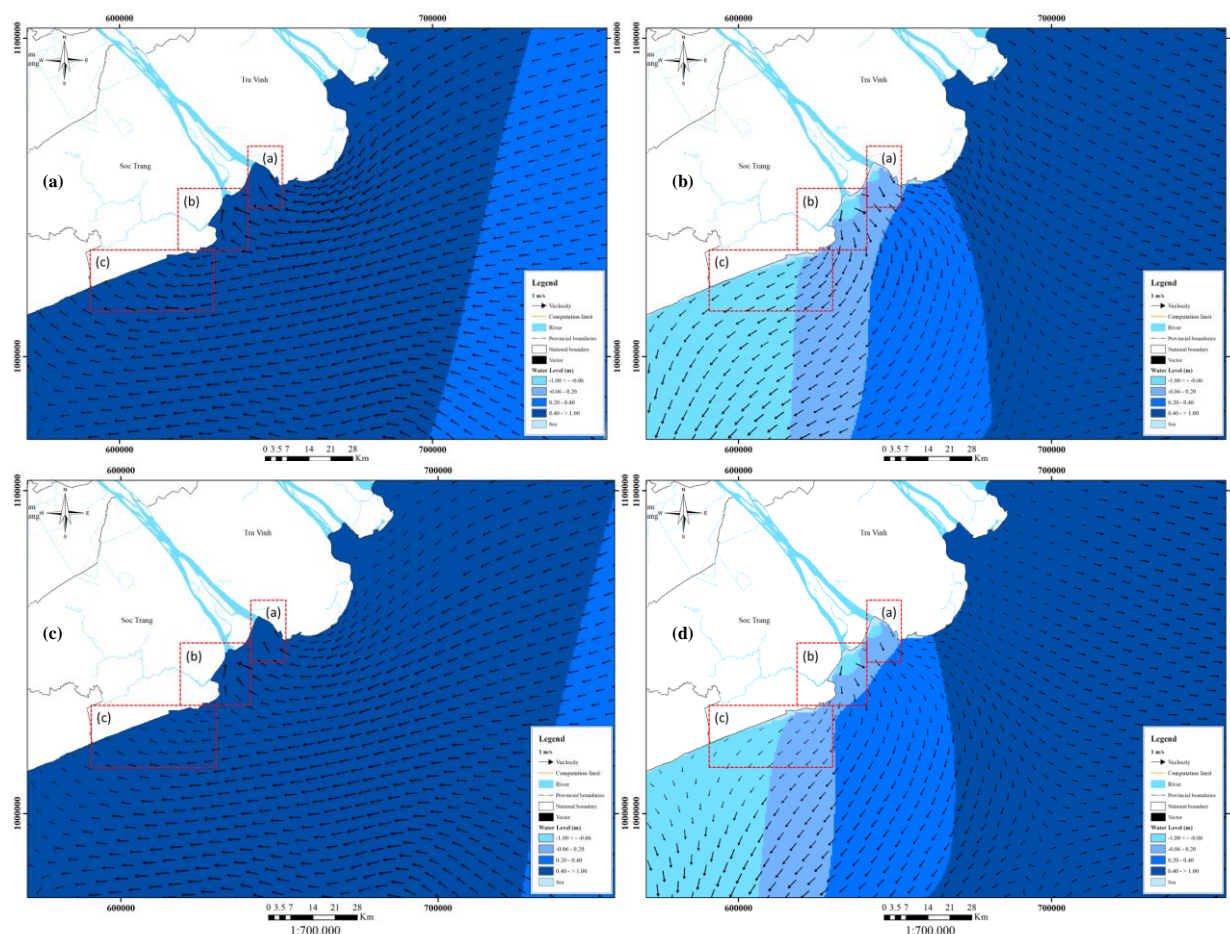


Figure 9. Simulation results of the coastal current in: (a) the northeast monsoon season at spring tide phase at 13:00 on 15 February 2017; (b) the northeast monsoon season at neap tide phase at 19:00 on 15 February 2017; (c) the southwest monsoon season at spring tide phase at 14:00 on 20 September 2017; (d) the southwest monsoon season at neap tide phase at 20:00 on 20 September 2017.

To compare the influence of wave, wind and tide factors in the study area, three positions S1, S2 and S3 are extracted to consider the velocity value, these three positions are described as in Table 1.

Table 1. The extraction sites.

No	Name	Lattitute	Longtitude
1	S1	9°09'05.80"N	105°55'31.87"E
2	S2	9°13'35.21"N	106°09'27.98"E
3	S3	9°25'09.94"N	106°13'19.50"E

According to the statistical results from Figure 10 and Figure 11, because the wave induced current and the wind induced current in the Northeast monsoon has a Southwest - Northeast direction, coinciding with the spring and neap tides during the Northeast monsoon, so the coastal current velocity increases. Meanwhile, because the wave induced current and the wind induced current in the Southwest monsoon have a Northeast-Southwest direction, in contrast with the spring and neap tides during the Southwest monsoon, the flow velocity decreases. The influence of waves and winds deep into the estuary is negligible.

This result is quite similar to the simulation results of currents under the influence of waves and tides in both direction and magnitude in the study of [27].

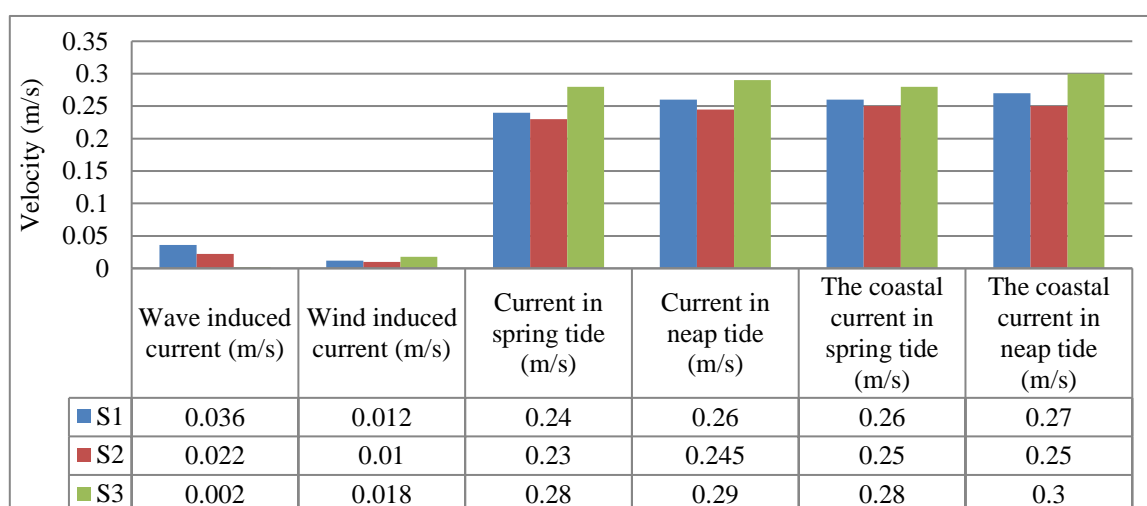


Figure 10. Coastal current velocity of each single element and total flow during the Northeast monsoon season at the extraction sites.

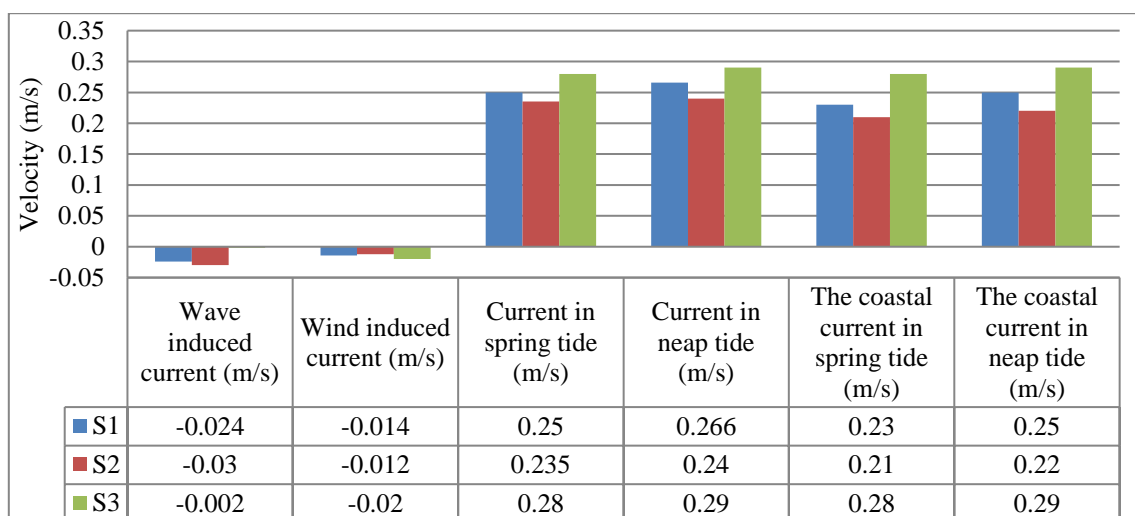


Figure 11. Coastal current velocity of each single element and total flow during the Southwest monsoon season at the extraction sites.

4. Conclusion

The coastal currents in the study area are influenced by various factors, including wind, waves, and tides. During the northeast monsoon season, wind induced currents flow along the coast in the northeast direction, with the highest velocity of 2.5 cm/s observed in the Soc Trang coastal area. In the southwest monsoon season, the wind induced currents flow along the shore in the southwest direction, but with lower velocities compared to the northeast monsoon season. Wave induced currents are also influenced by the wind seasons, flowing from the northeast to the southwest and into the West Sea during the northeast monsoon, and from the southwest to the northeast during the southwest monsoon. The velocities of wave induced currents are generally higher in the northeast monsoon season. However, tidal currents dominate the coastal currents, with significantly higher velocities than wind and wave induced currents. During the spring tide phase, tidal currents reach their maximum velocities, nearly 1 m/s at the river mouth, while remaining relatively smaller in the overall region. In the Dinh An estuary, tidal current velocities range from 0.54 to 0.96 m/s, and in the Tran De estuary, they range from 0.4 to 0.92 m/s. During the neap tide phase, the velocity difference between the river mouth and surrounding areas is even more pronounced. Tidal currents close to the shore have negligible velocities.

Regarding the coastal current, in the northeast monsoon season, the tidal currents from the northeast-southwest are in the same direction as the wave induced current, leading to an increase in the coastal current during spring tide (3-5%) and at neap tide (2-5%). In the southwest monsoon season, the direction is the opposite for tidal current and wave induced current; as a result, the velocities of the coastal current decrease at high tide (3-4%) and low tide (3-4.5%). The influence of winds deep in the estuary (Tran De and Dinh An estuaries) is negligible because these areas are small and low-lying, which reduces the influence of wind on the flow.

However, this study has not yet assessed the influence of wave induced currents on sediment transport along the coast, which is also a research direction for the future. In this study, some uncertainties that may affect the calculated results are the boundary conditions at the sea, which only consider the eight major tidal constituents.

Author Contributions: Conceptualization, T.T.K., N.T.B.; methodology, T.T.K., N.V.P., N.T.B., N.K.P.; software, T.T.K., N.D.Q.H., P.T.M.D., P.A.T.; validation, P.T.M.D.; formal analysis, T.T.K., P.T.M.D., N.D.Q.H.; investigation, N.T.B., N.K.P.; resources, N.T.B.; data curation, N.D.Q.H., N.T.B.; writing—original draft preparation, T.T.K., N.T.B.; writing—review and editing, T.T.K., N.T.B.; visualization, N.V.P., N.D.Q.H.; supervision, N.K.P., N.T.B.; project administration, N.K.P.; funding acquisition, N.K.P.

Acknowledgments: We would like to thank Ho Chi Minh City University of Technology (HCMUT), VNU–HCM for their donations of time and facilities for this study.

Conflicts of Interest: The authors declare no conflict of interest.

References

1. Tran, D.A.; Hoang, L.P.; Bui, M.D.; Rutschmann, P. Simulating future flows and salinity intrusion using combined one-and two-dimensional hydrodynamic modelling the case of Hau River, Vietnamese Mekong delta. *Water* **2018**, *10*(7), 897.
2. Stansby, P.K. Coastal hydrodynamics-present and future. *J. Hydraul. Res.* **2013**, *51*(4), 341–350.
3. Chang, S.W. et al. Does sea-level rise have an impact on saltwater intrusion? *Adv. Water. Resour.* **2011**, *34*(10), 1283–1291.
4. Galland, J.; Goutal, C.N.; Hervouet, J.M. TELEMAC: A new numerical model for solving shallow water equations. *Adv. Water. Resour.* **1991**, *14*(3), 138–148.
5. Hervouet, J.M. TELEMAC modelling system: an overview. *Hydrol. Processes* **2000**, *14*(13), 2209–2210.

6. Zangiabadi, E. et al. Computational fluid dynamics and visualisation of coastal flows in tidal channels supporting ocean energy development. *Energies* **2015**, *8*(6), 5997–6012.
7. de Saint-Venant, B.A.J.C. Théorie du Mouvement Non Permanent des Eaux, avec Application aux Crues de Rivières et à l'Introduction des Marées dans leur Lit. Comptes Rendus des séances de l'Académie des Sciences, 1871, pp. 147–154.
8. Castro-Orgaz, O.; Hager, W.H. Shallow water hydraulics. *Springer*, **2019**.
9. Ersoy, M.; Lakkis, O.; Townsend, P. A Saint-Venant model for overland flows with precipitation and recharge. *Math. Comput. Appl.* **2020**, *26*(1), 1.
10. Jia, Y.; Wang, S.S. Numerical model for channel flow and morphological change studies. *J. Hydraul. Eng.* **1999**, *125*(9), 924–933.
11. Jia, Y.; Wang, S.S. CCHE2D: Two-dimensional hydrodynamic and sediment transport model for unsteady open channel flows over loose bed. National Center for Computational Hydroscience Engineering, Technical Report No. NCCHE-TR-1, 2001.
12. Thakur, B. et al. Exploring CCHE2D and its sediment modelling capabilities. in World Environmental and Water Resources Congress 2018: Hydraulics and Waterways, Water Distribution Systems Analysis, and Smart Water. American Society of Civil Engineers Reston, VA, 2018.
13. Kadam, P.; Sen, D. Flood inundation simulation in Ajoy River using MIKE–FLOOD. *ISH J. Hydraul. Eng.* **2012**, *18*(2), 129–141.
14. Nigussie, T.A.; Altunkaynak, A. Modeling the effect of urbanization on flood risk in Ayamama Watershed, Istanbul, Turkey, using the MIKE 21 FM model. *Nat. Hazard.* **2019**, *99*(2), 1031–1047.
15. Sarker, S. Essence of MIKE 21C (FDM Numerical Scheme): Application on the River Morphology of Bangladesh. *Open J. Modell. Simul.* **2022**, *10*(2), 88–117.
16. Bomers, A.; Schielen, R.M.J.; Hulscher, S.J. The influence of grid shape and grid size on hydraulic river modelling performance. *Environ. Fluid. Mech.* **2019**, *19*(5), 1273–1294.
17. Baker, T.J. Discretization of the Navier Stokes equations and mesh induced errors. Mississippi State Univ. Mississippi State, MS (United States): United State, 1996.
18. Liu, X.; Ma, J.; Xu, S.; Wang, B. On the generation of coastline-following grids for ocean models—trade-off between orthogonality and alignment to coastlines. *Ocean. Dyn.* **2017**, *67*, 1095–1104.
19. Morianou, G.G.; Kourgialas, N.N.; Karatzas, G.P.; Nikolaidis, N.P. Assessing hydro-morphological changes in Mediterranean stream using curvilinear grid modeling approach-climate change impacts. *Earth. Sci. Inf.* **2018**, *11*(2), 205–216.
20. Yousefi, K.; Veron, F. Boundary layer formulations in orthogonal curvilinear coordinates for flow over wind-generated surface waves. *J. Fluid Mech.* **2020**, 888, A11.
21. Truong, Q.C.; Nguyen, T.H.; Tatsumi, K.; Pham, V.T.; Tri, V.P.D. A Land-Use Change Model to Support Land-Use Planning in the Mekong Delta (MEKOLUC). *Land* **2022**, *11*(2), 297.
22. Tran, D.A.; Tsujimura, M.; Vo, L.P.; Nguyen, V.T.; Kambuku, D.; Dang, T.D. Hydrogeochemical characteristics of a multi-layered coastal aquifer system in the Mekong Delta, Vietnam. *Environ. Geoche. Health* **2020**, *42*(2), 661–680.
23. Xing, F.; Meselhe, E.A.; Allison, M.A.; Weathers III, H.D. Analysis and numerical modeling of the flow and sand dynamics in the lower Song Hau channel, Mekong Delta. *Cont. Shelf Res.* **2017**, *147*, 62–77.
24. Tamura, T.; Horaguchi, K.; Saito, Y.; Nguyen, V.L.; Tateishi, M.; Ta, T.K.O.; Nanayama, F.; Watanabe, K. Monsoon-influenced variations in morphology and sediment of a mesotidal beach on the Mekong River delta coast. *Geomorphology* **2010**, *116*(1–2), 11–23.
25. Thanh, V.Q. et al. Sediment transport and morphodynamical modeling on the estuaries and coastal zone of the Vietnamese Mekong Delta. *Cont. Shelf. Res.* **2019**, *186*, 64–76.

26. Bayrak, M.M.; Marks, D.; Hauser, L.T. Disentangling the concepts of global climate change, adaptation, and human mobility: A political-ecological exploration in Vietnam's Mekong Delta. *Clim. Dev.* **2022**, 14(10), 1–10.
27. Marchesiello, P.; Nguyen, N.M.; Gratiot, N.; Loisel, H.; Anthony, E.J.; Dinh, C.S.; Nguyen, T.; Almar, R.; Kestenare, E. Erosion of the coastal Mekong delta: Assessing natural against man induced processes. *Cont. Shelf. Res.* **2019**, 181, 72–89.
28. Thanh, V.Q.; Reyns, J.; Wackerman, C.; Eidam, E.F.; Roelvink, D. Modelling suspended sediment dynamics on the subaqueous delta of the Mekong River. *Cont. Shelf. Res.* **2017**, 147, 213–230.
29. Nguyen, N.M.; San, D.C.; Nguyen, K.D.; Pham, Q.B.; Gagnon, A.S.; Mai, S.T.; Anh, D.T. Region of freshwater influence (ROFI) and its impact on sediment transport in the lower Mekong Delta coastal zone of Vietnam. *Environ. Monit. Assess.* **2022**, 194(7), 1–15.
30. Mai, N.P.; Thang, T.D.; Kantoush, S.; Sumi, T.; Binh, D.V.; Trung, L.V. The processes of saltwater intrusion into Hau River. Proceeding of the International Conference on Asian and Pacific Coasts. *APAC 2019*, pp. 1477–1483.
31. Kim, T.T.; Long, N.K.T.; Hong, N.T.T.; Phung, N.K.; Bay, N.T. Mapping the residual tidal ellipse from Vung Tau–Bac Lieu, Viet Nam by using a numerical model in curvilinear coordinate. *VN J. Hydrometeorol.* **2021**, 8, 50–63.
32. Kim, T.T.; Nguyen, T.T.P.; Hoang, H.K.; Nguyen, T.T.H.; Nguyen, T.N.M.; Phung, D.T.M. Mapping erosion-accretion risk maps in the coastal area of Soc Trang. *VN Sci. Tech. Dev. J.* **2021**, 5(SI2), SI64–SI74.
33. Kim, T.T.; Bay, N.T.; Ky, P.N.; Nguyen, M.T.T.; Tra, N.N.Q. Bottom morphology in hau estuaries under influences of sediment reduction and climate variation. *VN Sci. Tech. Dev. J.* **2021**, 4(SI1), SI84–SI94.
34. Thuy, N.T.D. et al. Modelling Accretion and Erosion Processes in the Bassac and Mekong Rivers of the Vietnamese Mekong Delta. Proceeding of the APAC 2019: Proceedings of the 10th International Conference on Asian and Pacific Coasts. Springer, Hanoi, Vietnam, APAC 2019, pp. 1431–1437.
35. Nash, J.E.; Sutcliffe, J.V. River flow forecasting through conceptual models part I—A discussion of principles. *J. Hydrol.* **1970**, 10(3), 282–290.
36. Moriasi, D.N.; Arnold, J.G.; Van Liew, M.W.; Bingner, R.L.; Harmel, R.D.; Veith, T.L. Model evaluation guidelines for systematic quantification of accuracy in watershed simulations. *Trans ASABE.* **2007**, 50(3), 885–900.
37. Steiger, J.H. Statistically based tests for the number of common factors. in the annual meeting of the Psychometric Society. Iowa City, IA. 1980.
38. Browne, M.W.; Cudeck, R. Alternative ways of assessing model fit In KA Bollen & JS Long (Eds.), Testing structural equation models. Newbury Park, CA: Sage, **1993**, 136–162.
39. Chen, C.; Lai, Z.; Beardsley, R.C.; Xu, Q.; Lin, H.; Viet, N.T. Current separation and upwelling over the southeast shelf of Vietnam in the South China Sea. *J. Geophys. Res: Oceans* **2012**, 117(C3), C03033.
40. Shi-Feng, S. Waves in South China Sea, in Oceanology of China Seas. *Oceanology China Seas* **1994**, 135–140.
41. Mirzaei, A.; Tangang, F.; Juneng, L.; Mustapha, M.A.; Husain, M.L.; Akhir, M.F. Wave climate simulation for southern region of the South China Sea. *Ocean Dyn.* **2013**, 63(8), 961–977.
42. Gugliotta, M.; Saito, Y.; Nguyen, V.L.; Ta, T.K.O.; Nakashima, R.N.; Tamura, T.; Uehara, K.; Katsuki, K.; Yamamoto, S. Process regime, salinity, morphological, and sedimentary trends along the fluvial to marine transition zone of the mixed-energy Mekong River delta, Vietnam. *Cont. Shelf Res.* **2017**, 147, 7–26.

Research Article

Evaluation of the current status of wastewater management and treatment from super-intensive whiteleg (*Penaeus vannamei*) shrimp ponds in Ben Tre Province

That Lang Ton^{1*}, Van Tan Lam², Tran Thi Kim Tu³, Van Tuan Nguyen¹

¹ Ho Chi Minh University of Natural Resources and Environment, Ho Chi Minh City, Vietnam; tlang@hcmunre.edu.vn

² Department of Science and Technology, Ben Tre province, Vietnam; lvtankhn@gmail.com

³ Center of Environment and Technology Service, Ho Chi Minh City, Vietnam; kimtu1610@gmail.com

*Correspondence: tlang@hcmunre.edu.vn; Tel.: +84–903893932

Received: 5 June 2023; Accepted: 11 July 2023; Published: 25 September 2023

Abstract: Ben Tre province in Viet Nam must contend with the fact that the farming environment is deteriorating because of poor disease management practices, pond wastewater discharge, and bottom muck. The current state of extremely intense shrimp farming in Ben Tre province is depicted in this study. In addition, this study also evaluates the state of Ben Tre province's wastewater treatment and super-intensive shrimp farming practices. Shrimp pond wastewater is often held in settling ponds in super-intensive shrimp farming households in three districts of Binh Dai, Ba Tri, and Thanh Phu of Ben Tre province, however, some households will continue to discharge wastewater through treatment ponds. According to the analysis's findings, treated shrimp ponds have considerably superior water quality than untreated shrimp ponds. However, the concentration of COD, BOD₅, H₂S, and NH₃ in treated ponds remained higher than the standard of QCVN 02-19:2014/BNNPTNT, although having dropped in comparison to untreated ponds. As a result of the aforementioned fact, it is imperative to conduct research and develop an environmentally friendly and highly effective wastewater treatment process to conserve and circulate water for extremely intensive shrimp ponds in the Ben Tre Province area.

Keywords: Super-intensive shrimp pond; Wastewater; *Penaeus vannamei*.

1. Introduction

The Vietnamese government is concentrating on intensive shrimp production, enhancing value chain efficiency, certification and standards enforcement, and minimizing risk in an effort to make the country the top exporter of seafood in the world. An empirical examination of the price relationship and the shrimp exports from Vietnam's supply chain revealed that the white-leg shrimp's price transmission was noticeably superior to the black-tiger shrimp's [1]. Therefore, white-leg shrimp farming is being interested and developed both in terms of area and intensification, especially in the development of high-tech white-leg shrimp farming [2–3]. With high levels of natural resource usage, probable environmental damage, ominous climatic changes, and wealth inequalities related to production intensification, the key question is whether super-intensive production can be the driver toward shrimp production sustainability [4]. In Vietnam, the Mekong Delta's coastal regions are home to the country's largest aquaculture region. Additionally, one of the coastal provinces, Ben Tre have a

J. Hydro-Meteorol. **2023**, *16*, 56-64; doi: 10.36335/VNJHM.2023(16).56-64 <http://vnjhm.vn/>

super-intensive shrimp farming area of approximately 2500 hectares by 2022. In order to transform the shrimp business into the province's main source of production, adapt to climate change, and safeguard the biological environment, Ben Tre province is also extending the area of marine shrimp farming with high-technology applications. Ben Tre, however, shares the same problem as many other areas in that the farming environment has been negatively impacted by infectious disease management, spontaneous development, discharge, and improper chemical use in general [5–6]. Furthermore, numerous new technological approaches have been discovered in an effort to address the enormous issues surrounding shrimp effluent and ensure its sustainability, but none could claim to be a comprehensive and integrated approach that takes into account all technical, legal, social, environmental, public health, and institutional concerns [7–10]. Regarding the characteristics of water quality and sediment in the vannamei culture system, there are many studies that have demonstrated that the quality evolution of pollutant parameters discharged from the shrimp farming process tends to increase over time [11–13]. Accordareg to research by [2] in 2010, sediment in shrimp ponds is produced from a variety of sources, including suspended solids from runoff, lime, fertilizers, chemicals, and antibiotics; uneaten food, dead phytoplankton, and molting shrimp shells; solid waste from shrimp production; and inorganic matter is eroded from the pond wall. Additionally, the usage of fertilizers, antibiotics, and pesticides in shrimp ponds can build up in the sediment and the environment. In 2019, in Ben Tre province, a study was conducted on the state of waste management and treatment from intensive white-leg ponds to evaluate the level of pollution, and the efficacy of available technologies, and to recommend treatment options that would be practical and affordable for farmers. Anh currently, the majority of shrimp farms directly discharge wastewater and sludge into the environment after each crop, contaminating the surrounding area and harming the health of the local populace. So, this study continues to evaluate the degree of pollution and the treatment potential of existing technologies, it is required to research the current condition of waste management and treatment from super-intensive white-leg ponds in Ben Tre province. This study is required because the practice that it addresses indicates improvements in shrimp farming performance.

2. Materials and Methods

This study included shrimp household from three districts of Ben Tre province: Binh Dai, Ba Tri, Thanh Phu, as shown in Figure 1.

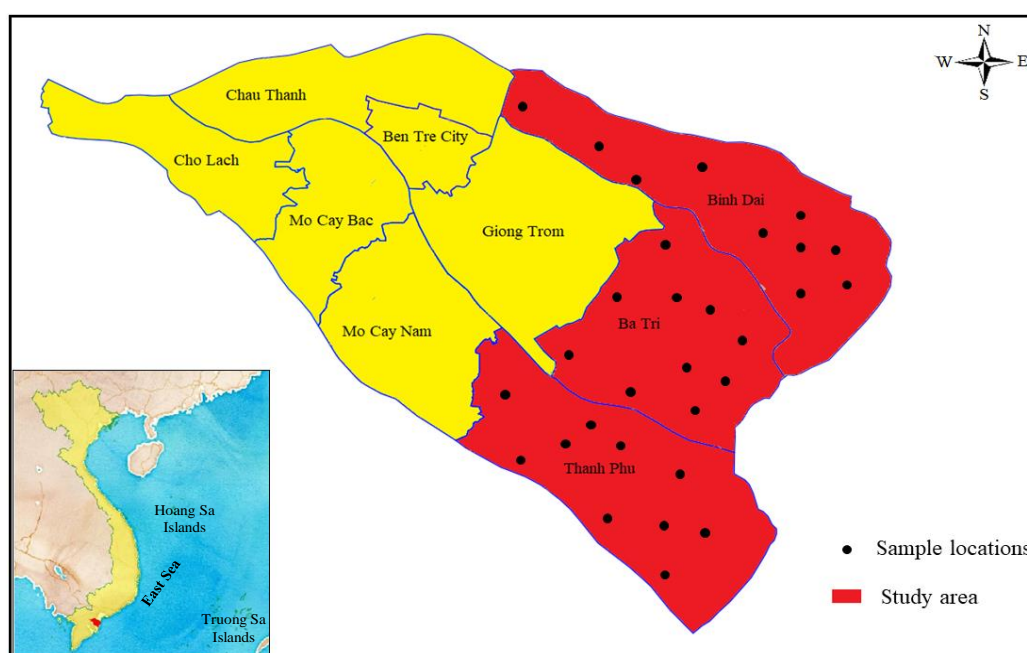


Figure 1. The study area.

The study uses the following methods:

- Method of sociological survey: collect information through 30 questionnaires in three districts of Binh Dai, Ba Tri, and Thanh Phu to determine the area of ponds, farming techniques, the amount of wastewater generated, and the method of production current methods of wastewater management and treatment.

- Statistical method: used to process survey data, from there, determine the mean and standard deviation.

- Data processing: The water quality data were compared among the sampling locations and were also compared with QCVN 02-19:2014/BNNPTNT to assess water quality in farming areas [14].

Wastewater samples were collected in 30 super-intensive shrimp ponds in Binh Dai, Ba Tri, Thanh Phu districts of Ben Tre province. Wastewater samples, after being transported to the laboratory, were analyzed for Temperature, Dissolved Oxygen (DO), pH, Salinity, Ammonia (NH₃), Ammonium (NH₄⁺), H₂S, Nitrite (NO₂⁻), Phosphate (PO₄³⁻), Total Suspended Solids (TSS), COD, BOD₅. Wastewater samples were taken and preserved according to the instruction of TCVN 6663-1:2016 and analyzed by specialized methods as shown in Table 1.

Table 1. Methods of analyzing pollution parameters in the wastewater environment of shrimp ponds.

Parameters	Methods
Field	
pH	TCVN 6492:2011
Temperature	SMEWW 2550B:2017
DO	TCVN 7325:2016
Salinity	SMEWW 2520:2012
Laboratory	
TSS	TCVN 6625:2000
COD	SMEWW 5520C:2012
BOD ₅	TCVN 6001-1:2008
PO ₄ ³⁻	TCVN 6202:2008
NO ₂ ⁻	TCVN 6178:1996
H ₂ S	US EPA Method 376.2
NH ₃	QCVN 10-MT:2015/BTNMT
NH ₄ ⁺	SMEWW 4500-NH ₃ .B&F:2017

3. Results and discussion

Super-intensive white-leg shrimp farming households use 3 main models in the shrimp farming process as follows:

Model 1: Reservoir Pond → sedimentation pond → Water treatment pond → Prepared Pond → culture pond.

Model 2: Reservoir Pond → sedimentation pond → Water treatment pond → culture pond.

Model 3: Reservoir Pond → sedimentation pond → culture pond.

3.1. Characteristic of shrimp wastewater

From September 2022 to February 2023, a survey was conducted at 30 households that raised white-leg shrimp in three districts of Ben Tre province: Binh Dai, Ba Tri, and Thanh Phu. Based on 10 households in each district, descriptive statistics of the pond, intake, and effluent water quality are presented as mean, standard deviation and derived for the super-intensive white-leg shrimp production characteristics in Ben Tre as shown in Table 2.

Table 2. Statistical analysis of technical parameters of the super-intensive white-leg shrimp farming.

Parameters	Unit	Binh Dai	Ba Tri	Thanh Phu
Pond area	(ha/household)	1.47±1.25	2.45±3.82	1.34±1.37
Pond number	-	9.3±4.69	10.5±11.5	7.6±7.63
Water deep of pond	m	1.53±0.10	1.53±0.48	1.55±0.06
Stocking density	PL/m ²	148±58.08	104±35.96	121±20.79
Production cycle duration	days	110±14.23	113±26.48	101±10.12
Number of employees	-	4±3	2±1	3±3

PL: Post Larvae

According to the study results, Ba Tri district has the greatest shrimp farming area (2.45 ha/household), and there is a significant disparity in size between shrimp farming families. Binh Dai and Thanh Phu districts, however, have shrimp farming areas that are comparable. Since larger areas are sometimes difficult to manage for ponds and water environment factors can easily change in a small area affecting shrimp growth and lowering productivity. Therefore, each shrimp square has an area of between 1 and 5 hectares.

Shrimp seed is stocked at densities ranging from 100 to 200 shrimp per square meter, high or low depending on the technical capabilities and financial resources of each household. According to the study findings, Ba Tri district has a lower stocking density than Binh Dai and Thanh Phu districts. The variables governing water depth, the number of harvest days, and the number of employees tasked with managing ponds are comparable amongst districts.

3.2. The process of raising and managing ponds

The management features of the selected household for the current status of using feed, antibiotics, chemicals and probiotics in super-intensive white-leg shrimp farming in three districts is presented in Table 3.

Table 3. Statistical analysis of using feed, antibiotics, chemicals, and preparations in super-intensive white-leg shrimp farming.

Parameters	Unit	Binh Dai	Ba Tri	Thanh Phu
Feed intake	kg/ha.day	187.82±29.07	134.97±70.73	200.62±127.96
Sterilizer	kg/m ²	0.043±0.00	0.027±0.0	0.027±0.00
Antibiotics	g/kg of feed intake	8.00±0.82	8.9±1.10	7.85±2.19
Vitamin	g/kg of feed intake	12.5±0.0	10±0.0	9.44±0.0
Bioproducts	l/1000m ²	2.9±0.2	2±0.0	1.8±0.3
Water treatment chemicals	kg/1000m ²	1.76±0.25	1.5±0.00	1.6±0.21

The amount of feed largely relies on stocking density and the length of postlarval days. With a high stocking density, the feed fed to the pond each day increases with the postlarvae's age in days. The behaviors and methods used to maintain and manage the ponds are other factors contributing to the variation in feed requirements among shrimp farms. According to the survey results, Binh Dai and Thanh Phu districts have a fairly high average feed intake, the lowest is Ba Tri district. The evolution of water quality, as well as the growth and development of cultured shrimp, are significantly impacted using food, antibiotics, vitamins, and biological products for detoxification and chemicals for disinfection. The survey reveals that among the three districts, the average amounts of sterilizer, vitamins, probiotics, and water treatment chemicals are not considerably different, and the variability is not

significant. Nevertheless, Ba Tri has the highest amount of antibiotics (8.9 g/kg of feed intake), while the stocking density is the least (104 ± 35.96 PL/m²).

Table 4. Statistical analysis of water use and wastewater generation in super-intensive white-leg shrimp farming.

Parameters	Unit	Binh Dai	Ba Tri	Thanh Phu
Intake water volume	m ³ /m ²	3336±2747.54	2055±1347.11	5400±3806.43
Total of effluent volume	m ³ /m ²	3386±2785.47	2060±1340.15	5733.43±4327.73

Statistical analysis of water use and wastewater generation in super-intensive white-leg shrimp farming is shown in Table 4. The water intake in shrimp ponds was the highest in Thanh Phu and the smallest in Ba Tri, while the average pond area in Thanh Phu was the smallest (1.34 ± 1.37 ha/household) and the largest in Ba Tri (2.45 ± 3.82 ha/household). In super-intensive culture ponds, excessive feed, and fertilizer use results in a significant nutrient influx into the natural water through the discharge canal. Without a doubt, during the growth cycles, the water exchange rate has a significant impact on the effluent loading [15–17].

3.3. Analysis results of pond wastewater quality

Sampling to analyze wastewater characteristics in Ba Tri district, Binh Dai district, Thanh Phu district gives the following results of water analysis parameters: Temperature, Dissolved Oxygen (DO), pH, Salinity, Ammonia (NH₃-N), Ammonium (NH₄-N), H₂S, Nitrite (NO₂-N), Phosphate (PO₄-P), Total Suspended Solids (TSS), COD, BOD₅.

Table 5 shows the analytical parameters of untreated super-intensive shrimp pond effluent analysis of some households in Ben Tre province. The analysis of untreated wastewater samples from super-intensive shrimp farming households reveals that the COD, BOD₅, H₂S, and NH₃ have mean values that exceeded the standard except for NH₃ in Ba Tri district. Temperature and pH are within normal ranges of the standard. The pH value in the wastewater from the observed, super-intensive shrimp ponds vary with a small amplitude between 7.4 and 7.8. The pH and DO mean values of the super-intensive shrimp pond wastewater are relatively similar to the pH and DO mean value in intensive shrimp ponds in Bac Lieu province [18]. However, salinity, PO₄³⁻, H₂S, and NH₃ of super-intensive shrimp ponds are greater than those of intensive shrimp ponds in Ben Tre province, with the exception of H₂S in Thanh Phu and Ba Tri districts and NH₃ in Thanh Phu District. The mean NH₄⁺ values of this study are greater, with the exception of Ba Tri district, than the effluent of super-intensive shrimp farms in Bac Lieu, which has NH₄⁺ ranges between 0.016 to 1.246 mg/l [19]. Additionally, the concentration of COD and BOD₅ in this study area is significantly higher than that of the hyper-intensive shrimp ponds in Bac Lieu, where COD concentrations range from 4.43 to 55 19 mg/l and BOD₅ concentrations from 10.21 to 90.12 mg/l. Probably, due to humus buildup, excessive manure, excess food, and other factors, water contains a large number of organic materials. Moreover, the amount of fertilizer given to various ponds determines the variation in COD and BOD₅ concentration in shrimp pond water, which contributes to the wide fluctuation range of COD and BOD concentrations in this research area.

Table 5. Analysis results of untreated super-intensive shrimp pond effluent in Ben Tre province.

Parameters	Unit	Binh Dai	Thanh Phu	Ba Tri	Intensive shrimp pond*	QCVN 02–19: 2014/BNNPTNT
pH	–	7.5±0.19	7.8±0.64	7.4±0.11	7.72 ± 0.34	5.5–9
Temperature	°C	28.±0.71	27.7±0.5	26.3±0.5	–	18–33

Parameters	Unit	Binh Dai	Thanh Phu	Ba Tri	Intensive shrimp pond*	QCVN 02-19: 2014/BNNPTNT
DO	mg/l	5.7±0.6	6.5±0.6	5.8±0.5	5.44 ± 0.7	–
Salinity	‰	10.7±0.5	12.3±2.0	10.33±0.5	12.7 ± 4.2	–
TSS	mg/l	58.3±24.74	36.6±12.5	40.3±10.5	74.4 ± 53.2	<100
COD	mg/l	1625.9±337.83	2054.6±448.2	1773.2±138.4	183 ± 4.8	<150
BOD ₅	mg/l	657.4±142.06	757.3±154.7	665.9±52.3	74.7 ± 19.7	<50
PO ₄ ³⁻	mg/l	0.1±0.13	0.1±0.1	0.1±0.0	0.2 ± 0.3	–
NO ₂ ⁻	mg/l	0.03±0.03	0.39±0.59	0.01±0.00	–	–
H ₂ S	mg/l	0.38±0.08	0.21±0.14	0.24±0.17	0.198 ± 0.03	< 0.05
NH ₃	mg/l	1.19±0.88	2.24±2.43	0.30±0.15	1.95 ± 1.4	< 0.3
NH ₄ ⁺	mg/l	1.26±0.90	2.36±2.50	0.32±0.16	–	–

*: Characteristics of effluent from intensive shrimp ponds of 30 households in 3 districts were sampled and analyzed

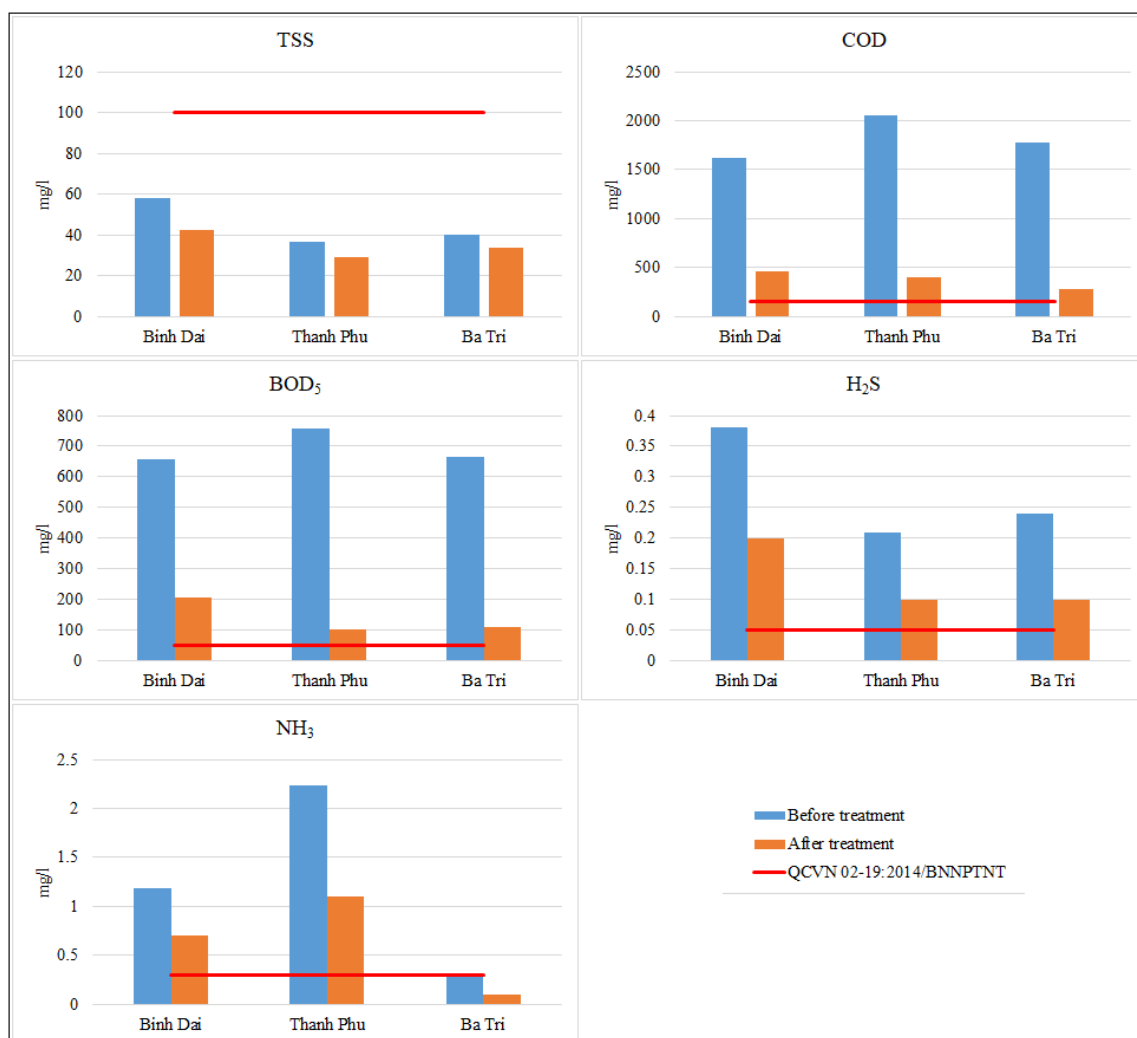


Figure 2. TSS, COD, BOD₅, H₂S, NH₃ concentrations in three districts before and after treatment.

The analysis result of treated super-intensive shrimp pond effluent in Ben Tre province is shown in Table 6. Based on the findings, it can be concluded that the mean pH, temperature, and salinity of treated super-intensive shrimp pond effluent are comparatively similar to those of untreated super-intensive shrimp pond effluent. The remaining analytical parameters with the exception of DO are significantly lower in treated super-intensive shrimp pond effluent than in untreated super-intensive shrimp pond effluent. Except for H₂S in Binh Dai district, the mean pH, temperature, and H₂S values are less than those of the treated intensive shrimp pond in Ben Tre. However, compared to intensive shrimp pond effluent, the DO, salinity, and NH₃ values are higher.

Table 6. Analysis results of treated super-intensive shrimp pond effluent in Ben Tre province.

Parameters	Unit	Binh Dai	Thanh Phu	Ba Tri	Intensive shrimp pond*	QCVN 02-19: 2014/BNNPTNT
pH	–	7.5±0.21	7.8±0.69	7.4±0.09	8.5	5.5–9
Temperature	°C	28±0.71	27.7±0.5	26.3±0.5	32	18–33
DO	mg/l	6.4±0.22	7.±0.45	6.5±0.18	6.4	–
Salinity	‰	10.7±0.5	12.3±2	10.3±0.5	7	–
TSS	mg/l	42.2±16.9	29.1±13.8	33.7±9.8	–	<100
COD	mg/l	463±157.3	397.6±38.7	284.6±26.2	–	<150
BOD ₅	mg/l	205.3±67.5	100.9±7.8	110.7±22.5	–	<50
PO ₄ ³⁻	mg/l	0.1±0.06	0.03±0.03	0.01±0.01	–	–
NO ₂ ⁻	mg/l	0.01±0.02	0.1±0.06	0.0003±0.001	–	–
H ₂ S	mg/l	0.2±0.04	0.1±0.01	0.1±0.05	0.2	< 0.05
NH ₃	mg/l	0.7±0.6	1.1±1.1	0.1±0.1	0.46	< 0.3
NH ₄ ⁺	mg/l	0.8±0.64	1.1±1.12	0.1±0.1	–	–

*: The water quality after 30 days of settling of a shrimp farming household in Thanh Phu district, Ben Tre.

Figure 2 illustrates that the concentration of COD and BOD in treated wastewater declined the most, whereas the concentration of TSS in the shrimp pond did not vary much between before and after treatment. In addition, the concentration of H₂S and NH₃ in treated wastewater was reduced by half. However, the quantities of COD, BOD₅, H₂S, and NH₃ in treated ponds remained higher than the standard of QCVN 02-19:2014/BNNPTNT, although having dropped in comparison to untreated ponds.

4. Conclusions

The average water surface area per household for the super-intensive white-leg shrimp ponds in the three districts of Binh Dai, Ba Tri, and Thanh Phu in the province of Ben Tre is 1.34–2.45 ha, with a water depth of 1.53–1.55 m. According to the three main methods of shrimp farming, shrimp pond wastewater is typically stored in a settling pond after each crop, with 100% of the wastewater being treated by settling ponds. Some facilities will also keep processing shrimp pond wastewater using treatment ponds. The parameters of H₂S, NH₃, BOD₅, and COD remain exceed the permitted limits for the pond, despite the fact that the quality of shrimp pond wastewater after treatment is better than the quality of shrimp pond wastewater before treatment.

Wastewater treatment is therefore necessary to recycle, reuse, or discharge waste into the canal. In comparison to the criteria for surface water quality [20] and marine water quality [21], PO₄³⁻, NO₂⁻, and NH₄⁺ must be treated to minimize their concentrations in order to ensure the survival of aquatic animal life. To support the sustainable development of the fishing industry, it is important to create a high-tech shrimp farming model that is both ecologically beneficial and associated with financial gains.

Author Contribution: Conceptualization: D.H.P.; methodology: D.H.P.; Processing of data: D.H.P.; Construction of maps: D.H.P.; Analysis of results: D.H.P.; writing–original draft preparation: D.H.P.; writing–review and editing: D.H.P.

Acknowledgments: Department of Science and Technology, Ben Tre province, Vietnam.

Conflicts of Interest: This manuscript is the research work of the collective author, not published anywhere, not copied from previous studies.

References

1. Truong, H.N.; Le, T.C.; Pham, T.T. Price transmission in shrimp production in Vietnam. *IOP Conf. Ser. Earth Environ. Sci.* **2023**, *1155(1)*, 012028. Doi:10.1088/1755-1315/1155/1/012028.
2. Ngoc, P.T.A.; Le, V.; Pham, T.T.; Pham, H.C.; Le, T.C.; Lansink, A.O. Technical and scale efficiency of intensive white-leg shrimp (*Litopenaeus vannamei*) farming in Vietnam: A data envelopment analysis. *Aquac. Econ. Manag.* **2023**, *27(1)*, 50–65. Doi:10.1080/13657305.2021.2003483.
3. Thakur, K.; Patanasatienkul, T.; Laurin, E.; Vanderstichel, R.; Corsin, F.; Hammell, L. Production characteristics of intensive whiteleg shrimp (*Litopenaeus vannamei*) farming in four Vietnam Provinces. *Aquac. Res.* **2018**, *49(8)*, 2625–2632. Doi:10.1111/are.13720.
4. Nguyen, T.A.T.; Nguyen, K.A.T.; Jolly, C. Is super-intensification the solution to shrimp production and export sustainability?. *Sustainability* **2019**, *11(19)*, 1–22. Doi:10.3390/su11195277.
5. Phu, T.M.; Vinh, P.Q.; Dao, N.L.A.; Viet, L.Q.; Thinh, N.Q. Chemical use in intensive white-leg shrimp aquaculture in Ben Tre province, Vietnam. *Int. J. Sci. Res. Publ.* **2019**, *9(8)*, 92112. Doi:10.29322/ijsrp.9.08.2019.p92112.
6. Nguyen, T.C.; Phan, D.N.; Nguyen Thi, H.D.; Nguyen Ngoc, K.N.; Dang Ngo, Y.L. Water Quality Status of White Leg Shrimp Farming Areas in Binh Dai District, Ben Tre Province, Vietnam. *Tra Vinh Univ. J. Sci.* **2022**, *1(46)*, 94–103. Doi:10.35382/tvujs.1.46.2022.866.
7. Iber, B.T.; Kasan, N.A. Recent advances in Shrimp aquaculture wastewater management. *Heliyon* **2021**, *7(11)*, e0828. Doi:10.1016/j.heliyon.2021.e08283.
8. Chellapandi, P. Development of top-dressing automation technology for sustainable shrimp aquaculture in India. *Discov. Sustain.* **2021**, *2*, 26. Doi:10.1007/s43621-021-00036-9.
9. McIntosh, R. Advancing Shrimp Farm Technologies Support Greater Efficiencies, Sustainability. *Glob. Aquac. Advocate* **2008**, 88–90.
10. Beltrán-Lugo, L.; de León, F.I.D.; Peinado-Guevara, V.; Peinado-Guevara, H.; Herrera-Barrientos, J.; Cuadras-Berrelleza, A.A.; Montoya-Leyva, M.A. Sustainable Innovation Management in the Shrimp Sector of the Municipality of Guasave, State of Sinaloa, Mexico. *Sustainability* **2023**, *15(4)*, 3161. Doi:10.3390/su15043161.
11. Umamaheswari, T.; Rajakumar, M.; Senthiladeban, R.; Felix, N.; Athithan, S.; Sugumar, G. Value chain approaches in farmed white leg shrimp *Penaeus vannamei* in Nagapattinam district of Tamil Nadu. *J. Entomol. Zool. Stud.* **2018**, *6(5)*, 2071–2077.
12. Mateka, H.A.; Tamatamah, R.; Kyewalyanga, M. Study on the Water Quality Parameters in Semi-Intensive Coastal Shrimp Culture System in Mafia Island, Tanzania. *J. Environ. Earth Sci.* **2015**, *5(1)*, 142–151.
13. Barraza-Guardado, R.H.; Arreola-Lizárraga, J.A.; López-Torres, M.A.; Casillas-Hernández, R.; Miranda-Baeza, A.; Magallón-Barrajas, F.; Ibarra-Gámez, C. Effluents of shrimp farms and its influence on the coastal ecosystems of bahía de Kino, Mexico. *Sci. World J.* **2013**, *2013*. Doi:10.1155/2013/306370.

14. MONRE. National technical regulation on backish water shrimp culture farm-Conditions for veterinary hygiene environmental protection and food safety, 2014.
15. Hopkins, J.; Hamilton, R.; Sandifer, P.; Browdy, C.; Stokes, A. Effect of Water Exchange Rate on Production, Water Quality, Effluent Characteristics and Nitrogen Budgets of Intensive Shrimp Ponds. *J. World Aquac. Soc.* **2007**, *24*, 304–320. Doi:10.1111/j.1749-7345.1993.tb00162.x.
16. Boopathy, R.; Lyles, C. Shrimp Production and Biological Treatment of Shrimp Wastewater in the United States. *New Horizons Biotechnol.* **2008**, 235–252.
17. Makmur, Taukhid, I.; Tampangallo, B.R.; Asaad, A.I.J.; Rachmansyah. Application of sludge collector in super-intensive Vannamei shrimp farms. *IOP Conf. Ser. Earth Environ. Sci.* **2021**, 919, 012059. Doi:10.1088/1755-1315/919/1/012059.
18. Trang, D.T.D.; Tram, H.T.B.; Ton, T.L. An assessment of the province of Ben Tre's wastewater management and treatment practices related to the extensive white shrimp (*Litopenaeus vannamei*) ponds. *Resoures Environ. J.* **2020**, 1–3.
19. Giao, N.T.; Nhien, H.T.H.; Anh, P.K.; Thuptimdang, P. Groundwater quality assessment for drinking purposes: a case study in the Mekong Delta, Vietnam. *Sci. Rep.* **2023**, *13*, 4380. Doi:10.1038/s41598-023-31621-9.
20. MONRE. National technical regulation on surface water quality. 2015, pp. 13.
21. MONRE. National technical regulation on marine water quality. 2015.

Research Article

Flood risk assessment from high tide based on principal component analysis (PCA) of Sentinel-1 satellite images sequence for Ho Chi Minh City

Doan Ha Phong^{1*}

¹ Viet Nam institute of Meteorology, Hydrology & Climate Change; dhphong@gmail.com

*Correspondence: dhphong@gmail.com; Tel.: +84–913212325

Received: 8 June 2023; Accepted: 24 July 2023; Published: 25 September 2023

Abstract: Using Sentinel-1 image series with 10m resolution from the past to present by Principal Component Analysis (PCA) method for Ho Chi Minh City area, helping to assess flood risk due to canal leveling, slitting in some complicated times, narrows the space for water regulation. In addition, Climate change causes sea level rise, thereby increasing the existing water level along with that in large rivers and also causing storm surge, which coincides with the time of flood discharge at Dau Tieng and Tri An reservoirs. The situation of groundwater exploitation, subsidence of the existing ground is continuous and increasing. With the accumulated settlement estimated to date about 100 cm, the current settlement rate is about 2-5 cm per year. Particularly in concentrated areas such as commercial works, the subsidence rate is about 7-8 cm per year. The rate of land subsidence is about twice as high as sea level rise. Therefore, Ho Chi Minh City is one of the cities affected by flooding due to high tide, especially in the current climate change conditions. According to the statistics of flood-prone areas due to high tides from 2014 to 2022, Can Gio district has the highest risk of flooding, with a flooded area of up to 3.713.236 hectares. The districts with an extremely high risk of flooding after Can Gio district are Cu Chi district, Binh Chanh district, and Nha Be district, with 1,764,564 ha, and 1,296,246 ha, and 1,012,550 hectares.

Keywords: Satellite image; Sentinel-1; Flood risk; Principal Component Analysis; High Tides.

1. Introduction

Statistical and near-real-time information about flooded areas is necessary for several public services, e.g., emergency, rescue, rehabilitation, spatial planning, habitat monitoring, and adapting to climate change. Remote Sensing satellites can provide operational and timely data as well as spatial information on flooded areas covered by water. Two types of satellite imagery are available to monitor flood dynamics on the surface: optical aperture radar (OAR) and data radar (SAR). Optical remote sensing can only be applied in cloudless situations. However, flooding often occurs during periods of prolonged rain and frequent cloud cover. Therefore, SAR systems are often the preferred tool for monitoring floods from space. The flat, water surface is characterized by low SAR backscatter, and the difference in backscatter reflectance often enables flood mapping [1]. Using a combination of different SAR image data such as COSMO-SkyMed and Sentinel-1, or combined with Flood Research Optical images such as MODIS and terraSAR-X [2–5], monitor inundation changes thanks to the advantage of multi-temporal images and through surface cover indices [6–10], through the dynamic identification of the water-marked area [11], using the urban area marker [11–15], and using backscatter signals from SAR images to detect and mark the rapid evolution of flooded areas, especially flooding caused by high tides [16–18]. Based on the summary of A

local thresholding approach to flood water delineation [8, 18], the most applied method to map floods from a single image is the threshold histogram, which can be used in conjunction with other image processing methods. different photos. Time change detection techniques [19–20] and associative analysis [21] have also been used to map open water. However, time-varying detection methods require two images and may therefore be limited by the temporal coverage of the satellite images. To improve the accuracy of flood maps, the advantages of ancillary data, such as the HAND index (elevation above the nearest drainage) are derived from the DEM (digital elevation model) and the DIST index (distance from drainage system) are derived from the watershed as well as the land use map, which has been demonstrated in several studies [17, 18, 20, 22]. Most of the proposed methods for flood mapping are semi-automatic. A fully automated method integrating thresholding separation and fuzzy logic classifiers has been proposed and applied by the author [18] for TerraSAR-X processing and by the author [23] to process Sentinel-1 (S1).

Recent research by the authors [24–25] summarized the methods of mapping flooding under the forest canopy. Research by the author [24] showed that the most applied method to detect submerged areas under vegetation is to identify increased backscatter values compared with other objects. The penetration depth of SAR signals into vegetation is higher for longer wavelengths, so the use of L-band has been recommended [26, 27–28]. However, several studies [20, 29–30] have demonstrated the ability of C-band and X-band data to identify submerged vegetation, especially in the case of sparse forest and leafless forests. Co-polarization signals (HH or VV) are preferred over cross-polarized signals for mapping water under vegetation. Studies have shown that using HH polarization leads to more accurate results than VV polarization [31–32]. Furthermore, the use of polarization analysis and/or an interferometric SAR combination has been used to map flooding under vegetation [33]. However, the availability of full polarization data is often limited in terms of spatial extent and temporal coverage.

Sentinel-1 images have modes (i) single polarized VV (Vertical-Vertical) or HH (Horizontal) and (ii) double polarized VH (Vertical-horizontal) or HV (Horizontal-Vertical). investigated the effects of single VV and double VH polarization for flood monitoring in the Ebro River Basin, Spain, using Sentinel-1 images [34]. A combination of Sentinel1 and Landsat images for inundation area identification and flood impact monitoring for the Houston, Central Greece, and East Coast of Madagascar regions of the United States [35]. The results from the above studies all confirmed that the VV polarization for inundation monitoring results is quite suitable for building flood maps using Sentinel-1 images. The above examples demonstrate that VV polarization can be used to determine the water surface area with rapid variation and is well suited to the observation of high tides.

In the past, the creation of flood maps often took a lot of time and money using SNAP software. The recent introduction of the Google Earth Engine (GEE) cloud platform has increased the convenience of research [36–37], providing powerful computing resources for free. GEE has been widely used in large-scale and long-term flood dynamics monitoring missions [38–40]. Another advantage of this platform is that it provides multiple datasets, facilitates data collection, and allows researchers to use different datasets for collaborative analysis to improve data collection and algorithmic accuracy [41–42].

Simultaneous operation of 2 satellites, Sentinel 1A and Sentinel 1B, allows to shorten the time of image acquisition at a location on the earth's surface to 6 days (compared to 12 days if only 1 satellite is used). The sensor on the Sentinel-1 satellite acquires a composite open aperture radar image, channel C.

2. Methodology

2.1. Description of study site

Hydrological regimes: Since there are two main seasons of the rainy season and the dry season, the flow mode in the two systems of the Saigon River and the Dong Nai River also forms two respective flow modes. At the same time, due to the impact of the East Sea, the rivers of the inner city of Ho Chi Minh city are affected by the tide strongly and throughout the year. Here is the semi-diurnal tides regime shown through the fluctuations:

The moon fluctuates: two times of high tide and two times of low tide; the time of high tide is 50 minutes back compared to the previous day. Seasonal developments: There are two high tides in a month (from the 27th day of the previous month to the 5th of the following month and from the 13th to the 18th of the solar calendar). Seasonal fluctuation: Spring tides (days 11, 12, and 1 of the solar calendar): this period is maintained by the flow of the rainy season in the inner city, so the high tide period usually lasts from September to January of the solar calendar.

Subsidence: By synthesizing the results of high-speed measurements in the Ho Chi Minh city region and the Mekong River Delta in 2017, 2018 of the Ministry of Natural Resources and Environments showed the land in Ho Chi Minh city and the provinces of the Cuu Long river valley is falling down the main causes are:

- The group of natural causes such as the displacement of the plates, the soil processes attempting to end up dehydrating and the natural contraction of the layer of an early Holoxen sediment.
- The group of human-influenced causes such as underground water mining, urbanization increases the load on weak soil, vibration due to traffic activities.

Based on the Subsidence partition shows that Ho Chi Minh city is falling at a high rate of more than 10 cm in 10 years in the district of Binh Chanh, southern of Binh Tan district, district 8, district 7, east district 12, western district of Thu Duc, northern districts of Nha Be with a total area of 239 km². Especially where it dropped to 73 cm/10 years, from 2005-2015.

2.2. Method

Principal Component Analysis (PCA) operator, this operator generates the principal component images from a stack of co-registered detected images.

The PCA consists of a remapping of the information of the input co-registered images into a new set of images. The output images are scaled to prevent negative pixel values. The PCA operator consists of the following major steps:

Average the pixels across the input images to compute a mean image. Optionally subtract the computed mean image from each input image.

Subtract the mean value of each input image (or image from Average step) from itself to produce zero-mean images.

Compute covariance matrix from the zero-mean images given in Subtract step. Perform eigenvalue decomposition of the covariance matrix.

Compute PCA images by multiplying the eigenvector matrix by the zero-mean images given in Subtract step. Here the user can select the eigenvectors instead of using all vectors. The selection is done with a user input threshold, which is in

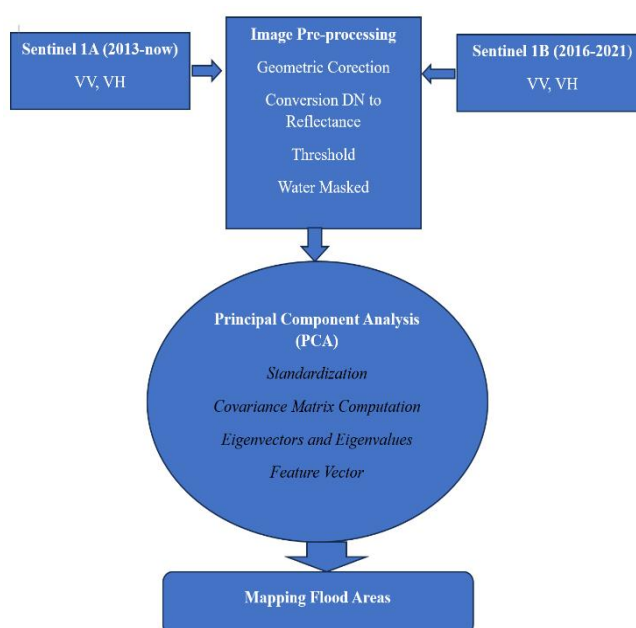


Figure 2. Flowchart of study structure.

percentage, on the eigenvalues. For example, in the case of three input images, a_1 , a_2 and a_3 (where $a_1 \gg a_2 \gg a_3$) are the eigenvalues, if the threshold is 80% and $(a_1+a_2) \gg 80\%$, then a_3 will not use in computing the PCA images. Only two PCA images will be produced.

The flowchart of study structure on principal component analysis (PCA) of Sentinel-1 satellite images sequence for Ho Chi Minh City (Figure 2).

The following parameters are calculated from the Sentinel 1 image data series for the period 2014-2022 in the Ho Chi Minh City area:

Source range: The VV polarization band is selected to perform PCA for the marking of flood-prone areas and other causes of flooding.

Eccentricity threshold: Threshold used in eigenvalue selection to produce the final PCA image. These are the values determined from the series of VV polarization values for the period 2014-2022, suitable for each year.

Show eigenvalues: Defines eigenvalues to be displayed automatically in areas flooded by high tides.

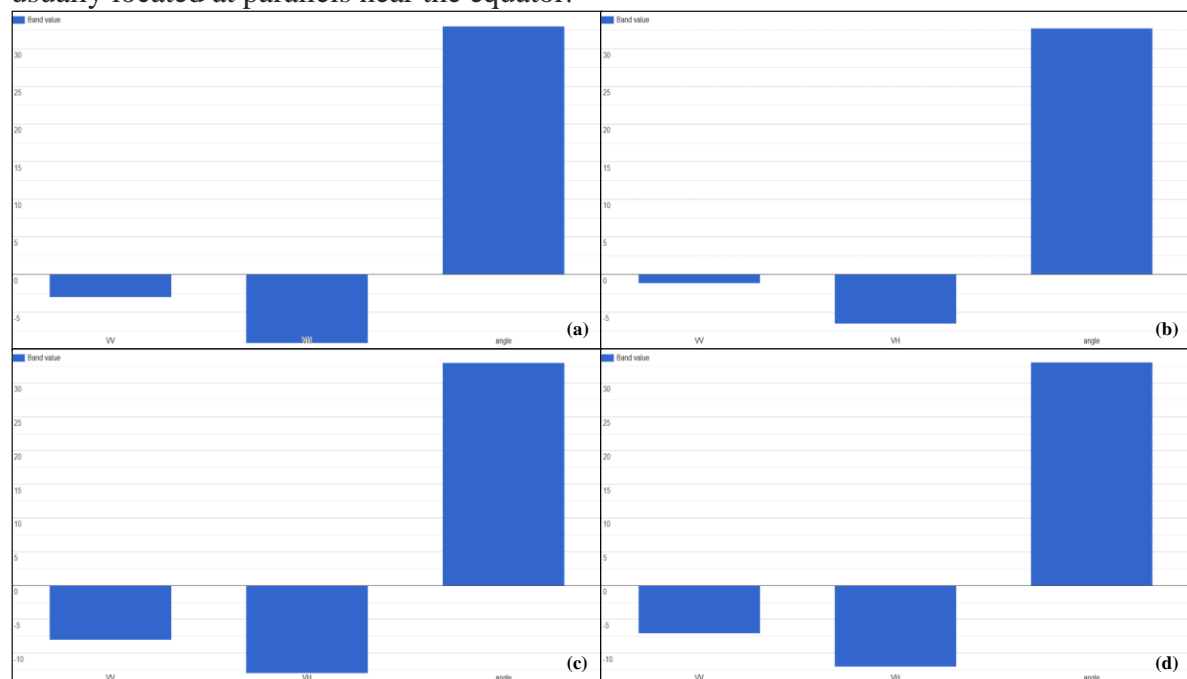
Subtracting the average image: The average image of the input images for the period 2014-2022 (September-January next year) is subtracted from each input image before applying PCA.

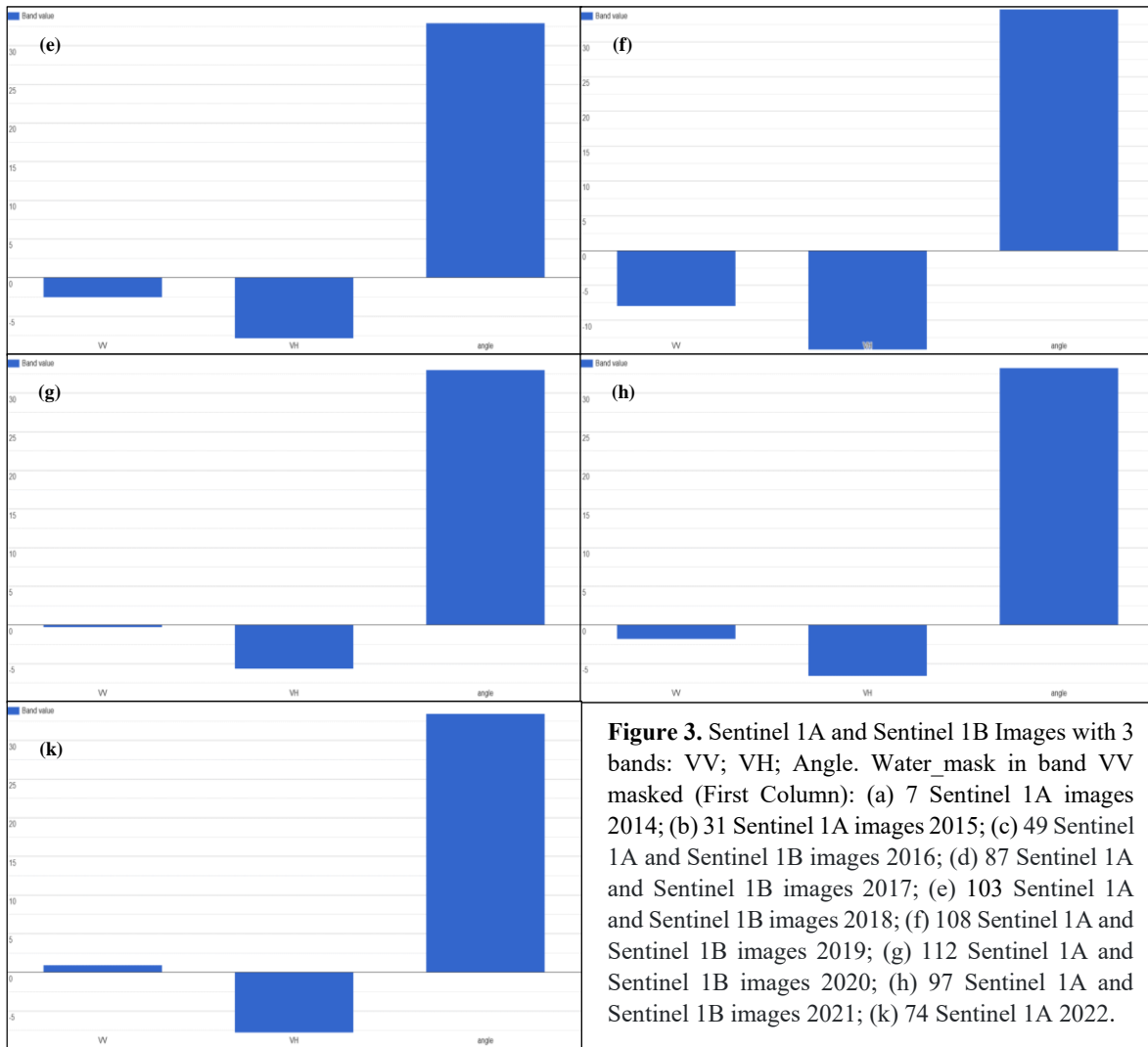
2.3. Data

Sentinel-1A was launched on 3 April 2014, and Sentinel-1B on 25 April 2016. They orbit 180° apart, together imagining the Earth every six days.

The two-satellite SENTINEL-1A and SENTINEL-1B constellation offers a 6-day exact repeat cycle. The constellation will have a repeat frequency (ascending/descending) of 3 days at the equator is expected to provide coverage over Ho Chi Minh city and main shipping routes in 1-3 days, regardless of weather conditions. Radar data will be delivered to Copernicus services within an hour of acquisition.

In December 2021, an anomaly in the power supply of Sentinel-1B caused the SAR sensor to stop working. Attempts to restore power to the sensor failed, and the mission officially ended on August 3, 2022. The highest tides of the year usually appear in October and November of the lunar calendar. The tidal regime in Ho Chi Minh City has a semi-diurnal tidal regime, with two high and low tides per day. The area affected by this type of tide is usually located at parallels near the equator.





The backscatter coefficients under VV polarization for the water area are lower than those under VH polarization (around 0–7 dB) (Figure 3a-3k).

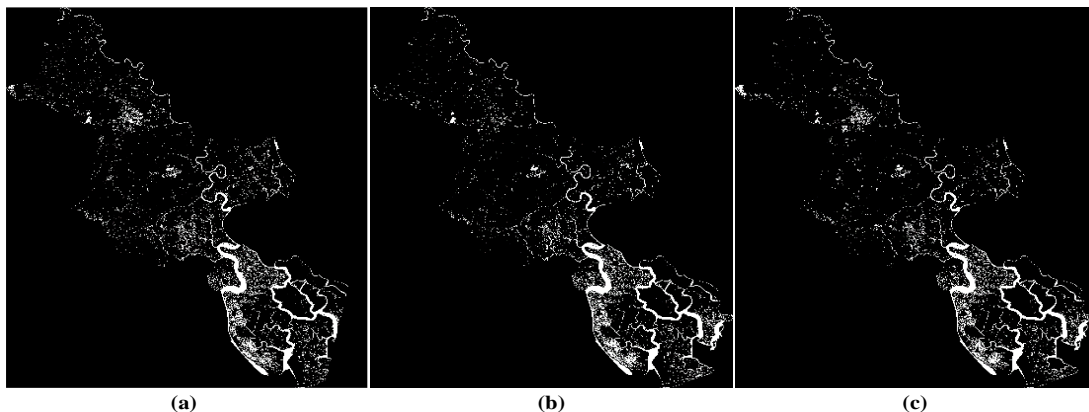
3. Results

3.1. Standardization

The aim of this step is to standardize the range of flood variables due to by continuous tides for years 2014 to 2022 to contributes equally to the analysis:

$$z = \frac{\text{value} - \text{mean}}{\text{standard deviation}} \tag{1}$$

Once the standardization is done, all the variables will be transformed to the same scale, a flood tides variable that 0 and 1.



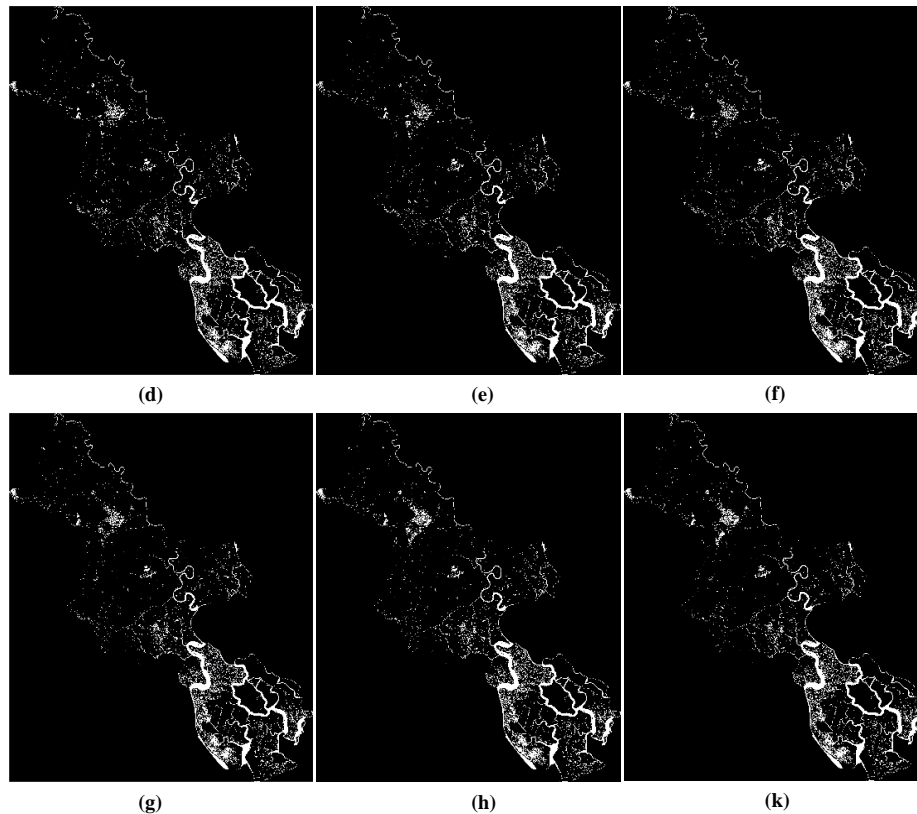


Figure 4. High tide based on principal component analysis (PCA) of Sentinel-1 satellite images sequence for Ho Chi Minh City. The image shows the distribution of flooding caused by high tide in Ho Chi Minh City from September to January next year in the period 2014–2022: (a) Flood tides 2014 (Component 1); (b) Flood tides 2015 (Component 2); (c) Flood tides 2016 (Component 3); (d) Flood tides 2017 (Component 4); (e) Flood tides 2018 (Component 5); (f) Flood tides 2019 (Component 6); (g) Flood tides 2020 (Component 7); (h) Flood tides 2021 (Component 8); (k) Flood tides 2022 (Component 9).

The Can Gio area is the area most affected by high tide from 2014 to 2022 from Sentinel-1A and Sentinel-1B. In addition, the regional city centers of Cu Chi district, Binh Chanh district, and Nha Be district are affected (Figure 4a-4k).

3.2. Covariance matrix computation

The variables of the input data set vary from the mean with respect to each other, to see if there is any relationship between them. Because sometimes, variables are highly correlated in such a way that they contain redundant information. To identify these correlations, we compute the covariance matrix from 0.3588 to 0.3746 will be selected. The covariance matrix is a 9×9 symmetric matrix (where 9 is the number of dimensions) that has as entries the covariances associated with all possible pairs of the initial variables (Table 1).

Table 1. Covariance matrix for 9-dimensional flood tides data year 2014 to 2022.

	1	2	3	4	5	6	7	8	9
1	0.0370	0.0288	0.0284	0.0280	0.0272	0.0278	0.0271	0.0270	0.0262
2	0.0288	0.0359	0.0310	0.0303	0.0296	0.0301	0.0293	0.0291	0.0282
3	0.0284	0.0310	0.0358	0.0317	0.0306	0.0308	0.0302	0.0302	0.0292
4	0.0280	0.0303	0.0317	0.0363	0.0318	0.0319	0.0311	0.0309	0.0301
5	0.0272	0.0296	0.0306	0.0318	0.0353	0.0324	0.0314	0.0312	0.0302
6	0.0278	0.0301	0.0308	0.0319	0.0324	0.0374	0.0329	0.0325	0.0316
7	0.0271	0.0293	0.0302	0.0311	0.0314	0.0329	0.0362	0.0330	0.031
8	0.0270	0.0291	0.0302	0.0309	0.0312	0.0325	0.0330	0.0370	0.0328

	1	2	3	4	5	6	7	8	9
9	0.0262	0.0282	0.0292	0.0301	0.0302	0.0313	0.0313	0.0328	0.0359

3.3. Compute the eigenvectors and eigenvalues of the covariance matrix to identify the principal components

Eigenvectors and eigenvalues are the linear algebra concepts that we need to compute from the covariance matrix to determine the principal components of the flood tides data. Principal components are new variables that are constructed as mixtures of the initial variables. These combinations are done in such a way that the new variables (i.e., principal components) are uncorrelated and most of the information within the initial variables is squeezed or compressed into the first components. So, the idea is 9-dimensional data gives you 9 principal components, PCA tries to put maximum possible information in the first component, then maximum remaining information in the second and so on Table 2.

Table 2. Eigenvectors of flood tides data year 2014 to 2022.

1	0.3079	0.7306	0.5768	-0.1828	-0.0699	-0.0020	-0.0003	-0.0096	-0.0115
2	0.3265	0.3343	-0.3588	0.5572	0.5064	0.2598	-0.1334	-0.0143	0.0154
3	0.3335	0.1791	-0.4010	0.1740	-0.4008	-0.6055	0.3703	-0.0233	-0.0196
4	0.3386	0.0219	-0.3455	-0.2906	-0.4377	0.3101	-0.4929	0.3839	0.0524
5	0.3358	-0.0955	-0.1930	-0.3903	0.0136	0.3148	0.2004	-0.7386	-0.0354
6	0.3450	-0.1788	-0.0168	-0.4138	0.4905	-0.0814	0.3916	0.4743	0.2271
7	0.3395	-0.2628	0.0144	-0.0633	0.2367	-0.3928	-0.4154	-0.0610	-0.6356
8	0.3406	-0.3214	0.3027	0.2362	-0.0554	-0.1992	-0.2975	-0.2076	0.6772
9	0.3308	-0.3289	0.3289	0.3945	-0.2938	0.4120	0.3838	0.18519	-0.2844

3.4. Feature vector

As we saw in the previous step, computing the eigenvectors and ordering them by their eigenvalues in descending order (0.27831-0.00332), allow us to find the principal components in order of significance. In this step, what we do to choose whether to keep all these components or discard those of lesser significance (of low eigenvalues), and form with the remaining ones a matrix of vectors that we call feature vectors. This makes it the first step towards dimensionality reduction, because if we choose to keep only 7 eigenvectors (components) out of 9:

Table 3. Percent and accumulative eigenvalues.

Component	Eigen value	Percent of eigen values	Accumulative of eigen values
2014	0.2783	85.0812	85.0812
2015	0.0141	4.4332	89.4137
2016	0.0085	2.5978	92.0115
2017	0.0059	1.8324	93.8439
2018	0.0052	1.5943	95.4382
2019	0.0042	1.2951	96.7334
2020	0.0037	1.1560	97.8894
2021	0.0035	1.0968	98.9862
2022	0.0033	1.0138	100.000

Table 4. Mean vector.

	Mean vector
2014	0.0384
2015	0.0373
2016	0.0372
2017	0.0377
2018	0.0366

Mean vector	
2019	0.0389
2020	0.0376
2021	0.0385
2022	0.0373

This makes it the first step towards dimensionality reduction, because if we choose to keep only 9 eigenvectors (components) out of 9, the final data set will have only 7 dimensions. 2016 and 2018 are the years with outstanding average values of high tide with values 0.0372 and 0.0366.

3.5. Recast the data along the principal components axes

In this step, which is the last one, the aim is to use the feature vector formed using the eigenvectors of the covariance matrix, to reorient the data from the original axes to the ones represented by the principal components (hence the name Principal Components Analysis). This can be done by multiplying the transpose of the original data set by the transpose of the feature vector.

$$\text{Final Data Set} = \text{Feature Vector}^T * \text{Standardized Original Data Set}^T \quad (2)$$

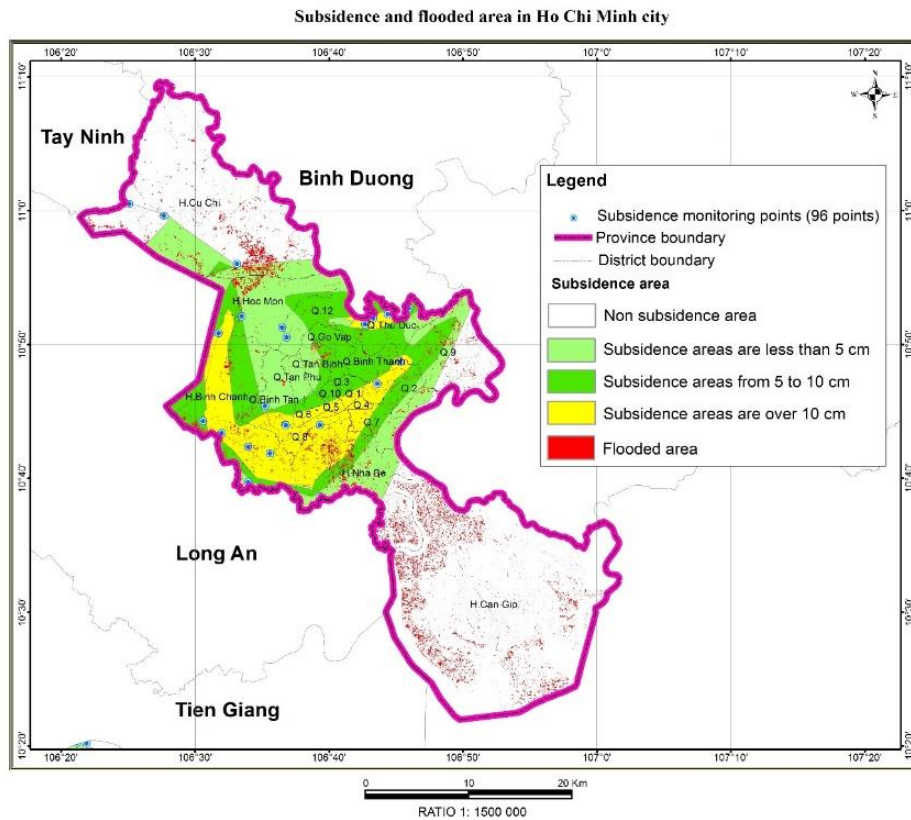


Figure 4. Flood risk assessment from high tide based on Sentinel-1 satellite for Ho Chi Minh City.

Table 5. Basic vector.

	C1	C2	C3	C4	C5	C6	C7	C8	C9
2014	0.3079	0.3265	0.3335	0.3386	0.3358	0.3450	0.3395	0.3406	0.3308
2015	0.7306	0.3343	0.1791	0.0219	-0.0955	-0.1788	-0.2628	-0.3214	-0.3289
2016	0.5768	-0.3588	-0.4010	-0.3455	-0.1930	-0.0168	0.1448	0.3027	0.3285
2017	-0.1828	0.5572	0.1740	-0.2906	-0.3930	-0.4138	-0.0633	0.2362	0.3945
2018	-0.0699	0.5064	-0.4008	-0.4377	0.01361	0.4905	0.2367	-0.0554	-0.2938
2019	0.0019	-0.2598	0.6055	-0.3101	-0.3148	0.0814	0.3928	0.1992	-0.4120
2020	3.8316	0.1334	-0.3703	0.4928	-0.2004	-0.3916	0.4154	0.2975	-0.3838
2021	-0.0096	-0.0143	-0.0233	0.3839	-0.7386	0.4743	-0.0610	-0.2076	0.1851
2022	-0.0115	0.0154	-0.0196	0.0524	-0.0354	0.2271	-0.6356	0.6772	-0.2844

The basis vector with the largest variance is the most principal (the one that explains more variance from the dataset). The dot product of each basis vector against the sample. Can be used as a measure for membership in the training sample set. High values correspond to a better fit.

4. Discussion

After 2021, only Sentinel 1A will be in operation, so the number of images collected for tidal research will be limited due to the decrease in the number of images collected. Therefore, the results collected for the period 2014–2022 can be used as a document to help study the distribution for the whole of Ho Chi Minh City visually for the period that is not only affected by high tide but also affected by socio-economic activities as well as affected by climate change.

According to the statistics of flood-prone areas due to high tides from 2014 to 2022, Can Gio district has the highest risk of flooding, with a flooded area of up to 3,713,236 hectares. The districts with a very high risk of flooding after Can Gio district are Cu Chi district, Binh Chanh district, and Nha Be district, with 1,764,564 ha, 1296,246 ha, and 1,012,550 hectares, respectively. Binh Chanh district is located in an area with a subsidence of more than 10 cm. Nha Be district is located in the subsidence area below 5cm and over 10 cm. In addition, other areas such as Hoc Mon district (inundated with 545,739 ha), district 2 (inundated with 673,997 ha), district 9 (inundated with 480,466 ha), Tan Binh district (inundated with 472,860 ha), and district 7 (inundated with 428,667 ha) are also at high risk of flooding due to high tides. Areas of District 2, District 7, District 9, and Tan Binh district are also located in the subsidence area of 5-10 cm. Areas with the lowest risk of flooding are District 3 and District 10, with a flooded area of just over 3,9 hectares. However, District 3 and District 10 are areas located in the subsidence area of 5-10 cm.

Author Contribution: Conceptualization: D.H.P.; methodology: D.H.P.; Processing of data: D.H.P.; Construction of maps: D.H.P.; Analysis of results: D.H.P.; writing—original draft preparation: D.H.P.; writing—review and editing: D.H.P.

Conflicts of Interest: This manuscript is the research work of the collective author, not published anywhere, not copied from previous studies.

Reference

1. Ulaby, F.; Moore, R.; Fung, A. Microwave Remote Sensing. Active and Passive, Artech House: Norwood, MA, USA, 1986, 3, pp. 608.
2. Boni, G.; Ferraris, L.; Pulvirenti, L.; Squicciarino, G.; Pierdicca, N.; Candela, L.; Pisani, A.R.; Zoffoli, S.; Onori, R.; Proietti, C.; et al. A Prototype System for Flood Monitoring Based on Flood Forecast Combined with COSMO-SkyMed and Sentinel-1 Data. *IEEE J. Sel. Top. Appl. Earth Obs. Remote Sens.* **2016**, *9*, 2794–2805.
3. Chen, Y.; Fan, R.; Yang, X.; Wang, J.; Latif, A. Extraction of urban water bodies from high-resolution remote-sensing imagery using deep learning. *Water* **2018**, *10*, 585.
4. Martinis, S.; Twele, A.; Strobl, C.; Kersten, J.; Stein, E. A multi-scale flood monitoring system based on fully automatic MODIS and terraSAR-X processing chains. *Remote Sens.* **2013**, *5*, 5598.
5. Pulvirenti, L.; Pierdicca, N.; Chini, M.; Guerriero, L. An algorithm for operational flood mapping from Synthetic Aperture Radar (SAR) data using fuzzy logic. *Nat. Hazards Earth Syst. Sci.* **2011**, *11*, 529–540.
6. Pulvirenti, L.; Pierdicca, N.; Chini, M.; Guerriero, L. Monitoring flood evolution in vegetated areas using cosmo-skymed data: The tuscan 2009 case study. *IEEE J. Sel. Top. Appl. Earth Obs. Remote Sens.* **2013**, *6*, 1807–1816.

7. Uddin, K.; Matin, M.A.; Meyer, F.J. Operational flood mapping using multi-temporal Sentinel-1 SAR images: A case study from Bangladesh. *Remote Sens.* **2019**, *11*, 1581.
8. Liang, J.; Liu, D. A local thresholding approach to flood water delineation using Sentinel-1 SAR imagery. *ISPRS J. Photogramm. Remote Sens.* **2020**, *159*, 53–62.
9. Schlaffer, S.; Matgen, P.; Hollaus, M.; Wagner, W. Flood detection from multi-temporal SAR data using harmonic analysis and change detection. *Int. J. Appl. Earth Obs. Geoinf.* **2015**, *38*, 15–24.
10. Wendleder, A.; Wessel, B.; Roth, A.; Breunig, M.; Martin, K.; Wagenbrenner, S. TanDEM-X water indication mask: Generation and first evaluation results. *IEEE J. Sel. Top. Appl. Earth Obs. Remote Sens.* **2013**, *6*, 171–179.
11. Chini, M.; Pulvirenti, L.; Pierdicca, N.; Guerriero, L. Multi-temporal segmentation of Cosmo-SkyMed SAR data for flood monitoring. In Proceedings of the 2011 Joint Urban Remote Sensing Event—JURSE 2011, Munich, Germany, 11–13 April 2011.
12. Chini, M.; Hostache, R.; Giustarini, L.; Matgen, P. A hierarchical split-based approach for parametric thresholding of SAR images: Flood inundation as a test case. *IEEE Trans. Geosci. Remote Sens.* **2017**, *55*, 6975–6988.
13. Giustarini, L.; Hostache, R.; Matgen, P.; Schumann, G.J.P.; Bates, P.D.; Mason, D.C. A change detection approach to flood mapping in Urban areas using TerraSAR-X. *IEEE Trans. Geosci. Remote Sens.* **2013**, *51*, 2417–2430.
14. Giustarini, L.; Hostache, R.; Kavetski, D.; Chini, M.; Corato, G.; Schlaffer, S.; Matgen, P. Probabilistic Flood Mapping Using Synthetic Aperture Radar Data. *IEEE Trans. Geosci. Remote Sens.* **2016**, *54*, 6958–6969.
15. Greifeneder, F.; Wagner, W.; Sabel, D.; Naeimi, V. Suitability of SAR imagery for automatic flood mapping in the Lower Mekong Basin. *Int. J. Remote Sens.* **2014**, *35*, 2857–2874.
16. Manjusree, P.; Prasanna Kumar, L.; Bhatt, C.M.; Rao, G.S.; Bhanumurthy, V. Optimization of threshold ranges for rapid flood inundation mapping by evaluating backscatter profiles of high incidence angle SAR images. *Int. J. Disaster Risk Sci.* **2012**, *3*, 113–122.
17. Marti-Cardona, B.; Dolz-Ripolles, J.; Lopez-Martinez, C. Wetland inundation monitoring by the synergistic use of ENVISAT/ASAR imagery and ancillary spatial data. *Remote Sens. Environ.* **2013**, *139*, 171–184.
18. Martinis, S.; Kersten, J.; Twele, A. A fully automated TerraSAR-X based flood service. *ISPRS J. Photogramm. Remote Sens.* **2015**, *104*, 203–212.
19. Long, S.; Fatoyinbo, T.E.; Policelli, F. Flood extent mapping for Namibia using change detection and thresholding with SAR. *Environ. Res. Lett.* **2014**, *9*, 035002.
20. Clement, M.A.; Kilsby, C.G.; Moore, P. Multi-temporal synthetic aperture radar flood mapping using change detection. *J. Flood Risk Manag.* **2018**, *11*, 152–168.
21. Chini, M.; Pelich, R.; Pulvirenti, L.; Pierdicca, N.; Hostache, R.; Matgen, P. Sentinel-1 InSAR coherence to detect floodwater in urban areas: Houston and hurricane harvey as a test case. *Remote Sens.* **2019**, *11*, 107.
22. Pierdicca, N.; Chini, M.; Pulvirenti, L.; Macina, F. Integrating physical and topographic information into a fuzzy scheme to map flooded area by SAR. *Sensors* **2008**, *8*, 4151.
23. Twele, A.; Cao, W.; Plank, S.; Martinis, S. Sentinel-1-based flood mapping: A fully automated processing chain. *Int. J. Remote Sens.* **2016**, *37*, 2990–3004.
24. Grimaldi, S.; Xu, J.; Li, Y.; Pauwels, V.R.N.; Walker, J.P. Flood mapping under vegetation using single SAR acquisitions. *Remote Sens. Environ.* **2020**, *237*, 111582.
25. Tsyganskaya, V.; Martinis, S.; Marzahn, P. Flood monitoring in vegetated areas using multitemporal Sentinel-1 data: Impact of time series features. *Water* **2019**, *11*, 1938.

26. Henderson, F.M.; Lewis, A.J. Radar detection of wetland ecosystems: A review. *Int. J. Remote Sens.* **2008**, *29*, 5809–5835.
27. Hess, L.L.; Melack, J.M.; Simonett, D.S. Radar detection of flooding beneath the forest canopy: A review. *Int. J. Remote Sens.* **1990**, *11*, 1313–1325.
28. Richards, J.A.; Sun, G.Q.; Simonett, D.S. L-Band Radar Backscatter Modeling of Forest Stands. *IEEE Trans. Geosci. Remote Sens.* **1987**, *GE-25*, 487–498.
29. Cohen, J.; Riihimäki, H.; Pulliainen, J.; Lemmetyinen, J.; Heilimo, J. Implications of boreal forest stand characteristics for X-band SAR flood mapping accuracy. *Remote Sens. Environ.* **2016**, *186*, 47–63.
30. Voormansik, K.; Praks, J.; Antropov, O.; Jagomagi, J.; Zalite, K. Flood mapping with terraSAR-X in forested regions in estonia. *IEEE J. Sel. Top. Appl. Earth Obs. Remote Sens.* **2014**, *7*, 562–577.
31. Pierdicca, N.; Pulvirenti, L.; Chini, M.; Guerriero, L.; Candela, L. Observing floods from space: Experience gained from COSMO-SkyMed observations. *Acta Astronaut.* **2013**, *84*, 122–133.
32. Townsend, P.A. Relationships between forest structure and the detection of flood inundation in forested wetlands using C-band SAR. *Int. J. Remote Sens.* **2002**, *23*, 443–460.
33. Brisco, B.; Schmitt, A.; Murnaghan, K.; Kaya, S.; Roth, A. SAR polarimetric change detection for flooded vegetation. *Int. J. Digit. Earth* **2011**, *6*, 103–114.
34. European Space Agency. Envisat overview. Online available: <https://earth.esa.int/eogateway/missions/envisat/description>. Accessed 12 December 2020.
35. Farr, T.G.; Rosen, P.A.; Caro, E.; Crippen, R.; Duren, R.; Hensley, S.; Kobrick, M.; Paller, M.; Rodriguez, E.; Roth, L.; Seal, D.; Shaffer, S.; Shimada, J.; Umland, J.; Werner, M.; Oskin, M.; Burbank, D.; Alsdorf, D.E. The shuttle radar topography mission. *Rev. Geophys* **2007**, *45*(2), RG2004. <https://doi.org/10.1029/2005RG000183>.
36. Gorelick, N.; Hancher, M.; Dixon, M.; Ilyushchenko, S.; Thau, D.; Moore, R. Google earth engine: planetary-scale geospatial analysis for everyone. *Remote Sens. Environ.* **2017**, *202*, 18–27. <https://doi.org/10.1016/j.rse.2017.06.031>.
37. Hirabayashi, Y.; Mahendran, R.; Koirala, S.; Konoshima, L.; Yamazaki, D.; Watanabe, S.; Kanae, S. Global flood risk under climate change. *Nat. Clim. Change* **2018**, *3*(9), 816–821. <https://doi.org/10.1038/nclimate1911>.
38. Jones, B.; Lamb, R.M. Hazards data distribution system (HDDS) (No. 2015–3048). US Geological Survey, 2015. <https://doi.org/10.3133/fs20153048>.
39. Kawasaki, A.; Berman, M.L.; Guan, W. The growing role of web-based geospatial technology in disaster response and support. *Disasters* **2013**, *37*(2), 201–221. <https://doi.org/10.1111/j.1467-7717.2012.01302.x>.
40. Klein, T.; Nilsson, M.; Persson, A.; Håkansson, B. From open data to open analyses—New opportunities for environmental applications? *Environments* **2017**, *4*(2), 32. <https://doi.org/10.3390/environments4020032>.
41. Kumar, A.; Pandey, A.C.; Khan, M.L. Urban risk and resilience to climate change and natural hazards: a perspective from Million-Plus Cities on the Indian Subcontinent. *Tech. Disaster Risk Manage. Mitigation* **2020**, 33–46. <https://doi.org/10.1002/9781119359203.ch3>.
42. Lal, P.; Prakash, A.; Kumar, A. Google Earth Engine for concurrent flood monitoring in the lower basin of Indo-Gangetic-Brahmaputra plains. *Nat. Hazards* **2020**, *104*(2), 1947–1952. <https://doi.org/10.1007/s11069-020-04233-z>.

Research Article

Application of 2D hydro-dynamic model to simulate the suspended sediment on the Tien river, Cao Lanh district, Dong Thap province

Nguyen Trong Khanh¹, Nguyen Huu Tuan¹, Hoang Thi To Nu¹, Can Thu Van^{1*}

¹ HCMC University of Natural Resources and Environment; ntkhanh@hcmunre.edu.vn; nhtuan@hcmunre.edu.vn; httnu@hcmunre.edu.vn; ctvan@hcmunre.edu.vn

*Corresponding author: ctvan@hcmunre.edu.vn; Tel.: +84–983738347

Received: 10 June 2023; Accepted: 20 July 2023; Published: 25 September 2023

Abstract: This study was carried out to analyze and evaluate the change in the amount of suspended sediment on the Tien River in the Mekong Delta. Evaluating the sediment transport regime is a very important task to effectively serve the assessment of the level of evolution (erosion/accumulation) on the riverbed. This study applied the Mike 21FM hydrodynamic model to simulate the sediment transport regime on the section flowing through Cao Lanh district, Dong Thap province - where the erosion process is very complicated recently. The simulation results show that the largest number of displaced sediments appears on the right bank, the maximum amount of sludge transported ranges from 0.91 kg/m³ to 2.7 kg/m³. During the simulation period, the total amount of sediment that has moved downstream is about -218.7×10^6 m³, the depth is -233 cm, the average rate of erosion is -77.6 cm/year, where the deepest erosion can be up to -10.0 m.

Key words: Suspended sediment; Sediment transport; River bottom evolution; Mike 21FM model.

1. Introduction

The phenomena of sedimentation and erosion are a natural process and occur continuously in most of the rivers on Earth. However, the process of sedimentation-erosion, especially riverbank erosion, becomes a concern when it causes great damage to land, property and people living along the riverbanks. In large rivers, scientists focus on the landslide process in the interaction between the country that occurs frequently over a long period of time [1–5]. Scientific studies around the world have studied the landslide process in different approaches and methods such as: (i) Approaching river geomorphology is the study of river morphological changes over time and space. These changes can be about: size, shape, river morphology [1–2, 6]; (ii) Hydrolith approach to river dynamics is to analyze the mechanisms of landslides, sediment transport and sedimentation due to river flows, from which to develop simulation methods, to calculate riverbed changes [7–8].

The situation of research on riverbed changes in the country and internationally is popularly carried out according to the methods in basic research such as: analysis method of measured data [9], physical modeling method [10], empirical formula method [11–13] or mathematical modeling method [14–17].

Dong Thap province is located in the southwestern region of Vietnam and is one of the important cities in the Mekong Delta with area of about 3.376 km². Dong Thap province borders Cambodia and is divided into 12 districts and Cao Lanh city is the administrative center, has a favorable geographical position, bordering Tien river and Hau river - two

important rivers of the region [18–19]. The Tien River section flowing through Dong Thap province has a length of about 120 km, the river width varies from 450 m (An Long, Tam Nong) to 2,200 m (the beginning of Long Khanh and Hong Ngu district); Average depth from 10÷15 m. In recent years, changes in the banks of the Tien River, the section flowing through Dong Thap province have been quite complicated; the general trend is to increase the scale and extent. In addition to the main natural causes (flow dynamics, shoreline geology), socio-economic development activities also significantly affect the riverbank changes, typically sand mining along the riverbank in the locality [20]. Therefore, the study and assessment of sediment transport in the study area is necessary, making an important contribution to the management of water resources, environmental protection, and sustainable development of the Tien River area.

Actual data on measuring sediment content shows that the value of sediment content is not high, but due to the large amount of runoff, the total annual amount of suspended alluvium of the Tien and Hau rivers through two cross-sections at Tan Chau and Chau Doc stations is relatively large. Due to the flow 4-5 times greater than that of the Hau River and the higher silt content, the total amount of alluvium from the Tien River through the Tan Chau cross-section in the same periods is many times larger than that of the Hau River through the Chau Doc section. In the period 2009-2020, the total amount of sediment in the Tien and Hau rivers has the same rate of decline in proportion to the decrease in sediment content [21].

Commonly used methods to represent changes in river morphology as well as sediment transport under human impacts, hydro-hydraulic regimes, climate change and sea level rise by means of mathematical modeling, physical modeling, remote sensing technology and GIS [1–2]. In this study, software package for 2D modelling of hydrodynamics and sediment dynamics of the DHI was selected to simulate and evaluate the movement of sediment on the Tien River through Cao Lanh district, Dong Thap province to propose technologies to predict erosion and sedimentation.

The study objectives are evaluation of hydraulic regime and sediment transport in the key landslide area at Cao Lanh - Dong Thap, thereby clarifying the hydrodynamic causes of landslides in the area. The research method to achieve the goal is: Successfully applying a 2-D hydrodynamic model to simulate the hydraulic regime and the sediment transport regime for the Tien river section, Cao Lanh district, Dong Thap province.

2. Materials and Methods

2.1. Theoretical module Mike 21FM HD

Module Mike 21 FM simulates the evolution of change and water level based on the equation of continuity and the equation of momentum in two directions [22]:

Equation of momentum:

$$\frac{\partial h}{\partial t} + \frac{\partial h\bar{u}}{\partial x} + \frac{\partial h\bar{v}}{\partial y} = hS \tag{1}$$

O_x direction:

$$\begin{aligned} \frac{\partial h\bar{u}}{\partial t} + \frac{\partial h\bar{u}^2}{\partial x} + \frac{\partial h\bar{v}\bar{u}}{\partial y} = f\bar{v}h - gh \frac{\partial \eta}{\partial x} - \frac{h}{\rho_0} \frac{\partial p_a}{\partial x} - \\ \frac{gh^2}{2\rho_0} \frac{\partial \rho}{\partial x} + \frac{\tau_{sx}}{\rho_0} - \frac{\tau_{bx}}{\rho_0} - \frac{1}{\rho_0} \left(\frac{\partial s_{xx}}{\partial x} + \frac{\partial s_{xy}}{\partial y} \right) + \frac{\partial}{\partial x} (hT_{xx}) + \frac{\partial}{\partial y} (hT_{xy}) + hu_s S \end{aligned} \tag{2}$$

O_y direction:

$$\frac{\partial h\bar{v}}{\partial t} + \frac{\partial h\bar{u}\bar{v}}{\partial x} + \frac{\partial h\bar{v}^2}{\partial y} = -f\bar{u}h - gh \frac{\partial \eta}{\partial y} - \frac{h}{\rho_0} \frac{\partial p_a}{\partial y} - \tag{3}$$

$$\frac{gh^2}{2\rho_0} \frac{\partial \rho}{\partial y} + \frac{\tau_{sy}}{\rho_0} - \frac{\tau_{by}}{\rho_0} - \frac{1}{\rho_0} \left(\frac{\partial s_{yx}}{\partial x} + \frac{\partial s_{yy}}{\partial y} \right) + \frac{\partial}{\partial x} (hT_{xy}) + \frac{\partial}{\partial y} (hT_{yy}) + hv_s S$$

where t is the time (s); x, y are coordinates (m); η is the water level change (m); d is the height; h is the water depth (m); g is the gravity acceleration (m/s^2); $f = 2\Omega \sin\phi$ - Coriolis (s^{-1}); ρ_0 is the density of water (kg/m^3); p_a is the atmospheric pressure (Pa/m); S is the discharge (m^3/s); u_s, v_s is the velocity (m/s); \bar{u}, \bar{v} are the velocity average of flow depth (m/s); T_{ij} is the internal stress components, determined by the eddy viscosity formula based on the mean velocity with depth; τ_{sx}, τ_{sy} are the surface friction stress in the x and y directions (N/m^2); τ_{bx}, τ_{by} are the bottom friction stress in the x and y directions (N/m^2); A is the horizontal turbulence coefficient (m^2/s); $S_{xx}, S_{xy}, S_{yx}, S_{yy}$ are components of wave radiation stress on unit volume of water in x and y directions (N/m^2).

The process of performing the simulation model as shown in Figure 1.

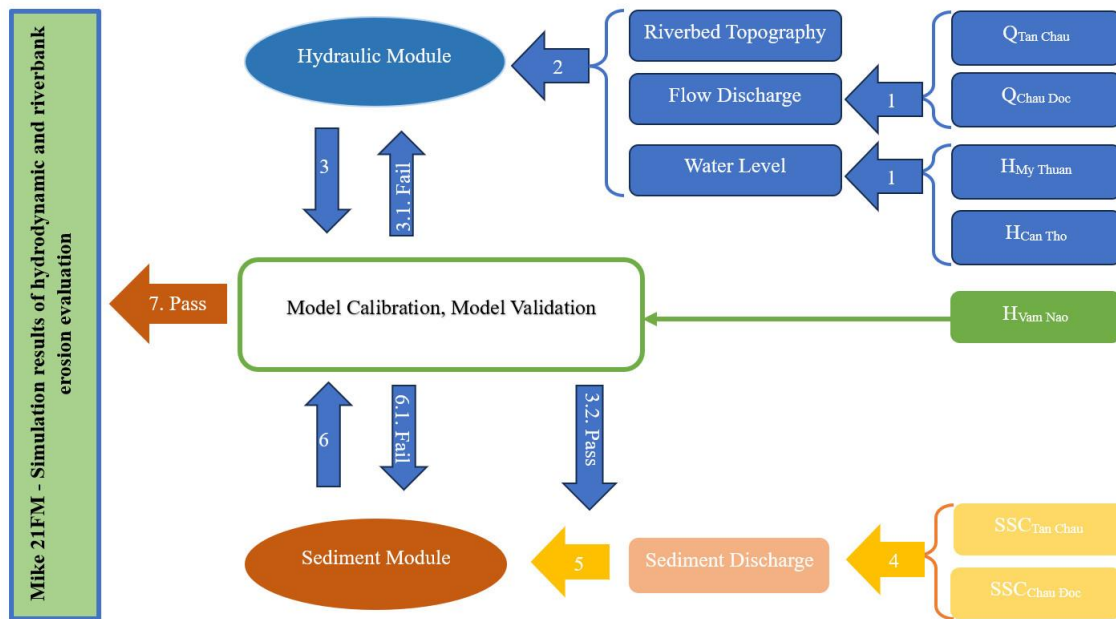


Figure 1. Flowchart of study structure [1–2].

2.2. Theoretical module MIKE 21FM-MT

The sediment transport module is set up based on the transport-diffusion equation [23]:

$$\frac{\partial \bar{c}}{\partial t} + u \frac{\partial \bar{c}}{\partial x} + v \frac{\partial \bar{c}}{\partial y} = \frac{1}{h} \frac{\partial}{\partial x} \left(hD_x \frac{\partial \bar{c}}{\partial x} \right) + \frac{1}{h} \frac{\partial}{\partial y} \left(hD_y \frac{\partial \bar{c}}{\partial y} \right) + Q_L C_L \frac{1}{h} - S \quad (4)$$

where t is time (s); x, y are coordinates (m); u, v are the depth-average velocity component in the direction x and y (m/s); h is the depth (m); \bar{c} is the average concentration of suspended sediment by depth (kg/m^3); D_x, D_y are the diffusion coefficient in the x, y directions (m^2/s); S is the term of the source of sediment due to erosion or accretion ($kg/m^3/s$); Q_L is the discharge rate per unit cross-sectional area ($m^3/s/m^2$); C_L is the concentration of suspended sediment at the inlet (kg/m^3).

Simulate bottom morphology: The sediment volume of the i^{th} grain class in the j^{th} bottom layer of the elements in the grid is updated after each time step. The volume of the bottom layer is updated according to the following equation:

$$m_{i,j}^{new} = m_{i,j}^{old} + (D_i - E_i)\Delta t + (T_{i,j-1} - T_{i,j}) \quad (5)$$

where m is the volume of sediment (kg/m^2); D is the amount of sediment ($kg/m^2/s$); E is the amount of erosion ($kg/m^2/s$); T is the amount of moving sediment of the bottom layer ($kg/m^2/s$); Δt is time step.

2.3. Data

2.3.1. Computational domain

The computational mesh built for the computational domain is a flexible mesh network, including 8.126 nodes with 134.644 elements, fully representing the areas in the riverbed as well as the riverbank. The maximum length of the element is 45 m and the minimum length is 5 m describing the riverbed and riverbank area [1–2].

The topographic database used in the construction of the grid for hydraulic calculations for the study area is processed from topographic survey data performed by the project with a resolution of 20m × 20m. River topographic data of 3 typical study areas are measured by echosounder with integrated GPS positioning, the file is exported as “.txt”, processed and cleaned into points by GIS tools (ArcGIS, Global Mapper, etc.) to include in the model for building elevation domain for the calculated area with detailed distance of 3-5m (Figures 2-3).

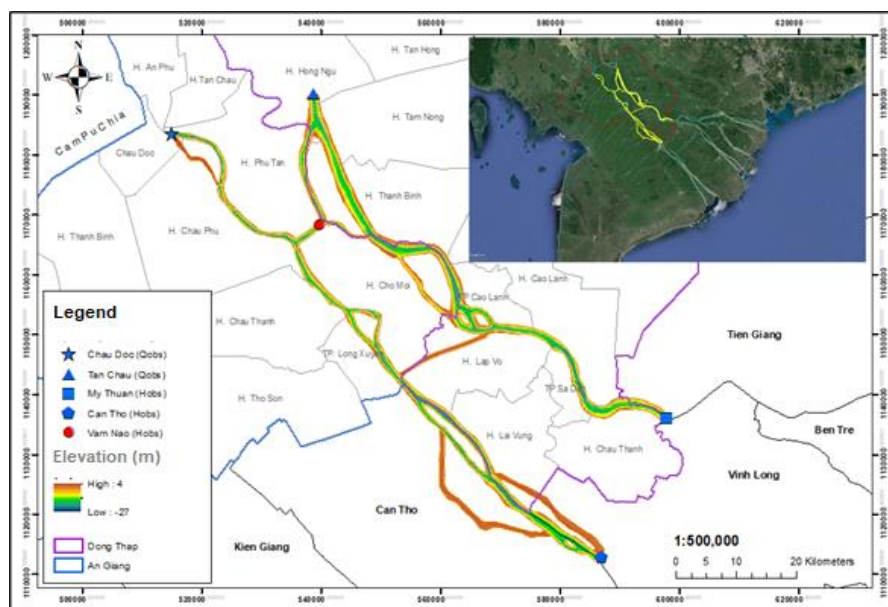


Figure 2. Domain study area.

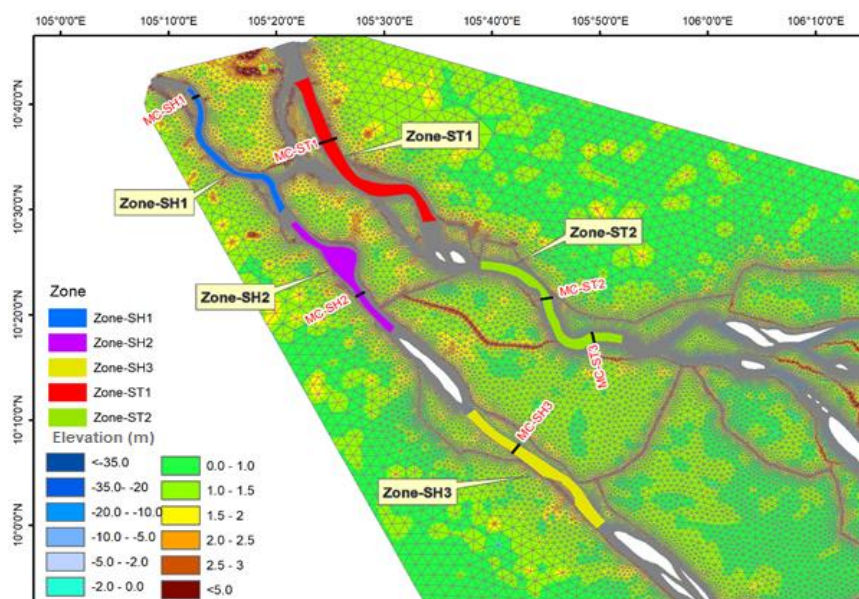


Figure 3. The location study area and calculation mesh.

2.3.2. Model setting

a) Boundary conditions

In this study, the team set up a 4-boundary domain, including 2 input boundaries to collect discharge and sediment data at Chau Doc hydrology station and Tan Chau hydrology station, 2 downstream boundaries to collect water level data at My Thuan hydrology station and Can Tho hydrology station. Select discharge and water level data at Vam Nao hydrology station to calibrate and verify the model [1–2].

Upstream boundary: Discharge margin taken at Tan Chau hydrological station and Chau Doc hydrology station, period data, from 00:00:00 01/01/2017–23/00/00 31/12/2019 (3 years). Sediment content margin (SSC) taken from Tan Chau station and Chau Doc station, day period data, from 01/01/2017–31/12/2019 (3 years).

Downstream boundary: Water level boundary taken at My Thuan hydrology station and Can Tho hydrology station, period data from 00:00:00 01/01/2017–23/00/00 31/12/2019 (3 years).

b) Modeling

The process, model testing is conducted after model calibration to check the reliability of the selected parameters with changed input factors:

- Hydraulic model calibration period: year 2000 and 2011.
- Hydraulic model verification period: 01/01/2018 to 31/12/2018.
- Sediment transportation model verification period: 01/01/2018 to 31/12/2018.
- Simulation and evaluation period: from 2017 to 2019.

The results of model correction will be shown in the hydrodynamic process including hydraulic factors such as: water level, velocity, and waves along with the sediment transport process such as the suspended sediment content in the flow. For the data of water level and suspended sediment will be adjusted in the dry season and verified in the flood season, while the flow velocity data due to lack of data should only be used for correction in the dry season.

3. Results and Discussion

In this study, flow measurement data, and sediment content (SSC) at Vam Nao hydrological station are used to calibrate and verify the model. These are two stations with good document quality, synchronous and long measurement data. The study uses solid measurement data in 2018 to calibrate and verify the model, calibrate in the dry season period (from January 2018 to June 2018) and verify during the flood season (from July 2018 to December 2018). For suspended sediment content, its evolution needs to be shown over a long time to be able to evaluate the reasonableness of the regularity, the study uses a continuous time series from January 2018 to December 2018 to calibrate and verify the model (Figures 4-5).

3.1. Calibration and validation of hydraulic model

Through the results of calculation of error indexes, the results of calibration and flow verification are good; NASH = 0.75-0.78 and the correlation coefficient is from 0.76-0.82. Therefore, it can be concluded that the model parameter set is stable and can be used for the setting and simulation step (Table 1).

Table 1. Calibration and verification results of the hydraulic model.

		R²	NASH
Calibration	2000	0.74	0.73
	2011	0.80	0.72
		R²	NASH
Validation	2018	0.78	0.76

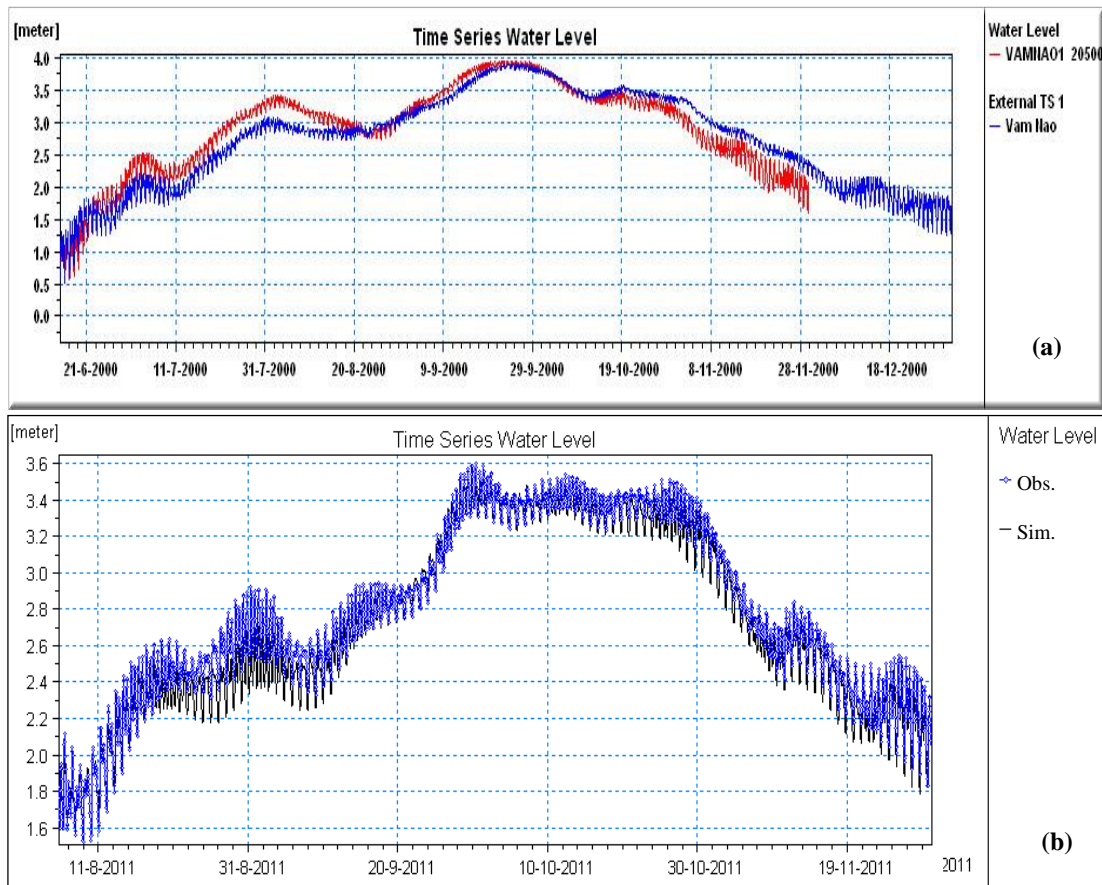


Figure 4. Results of calibration water level in Vam Nao station in 2000 and 2011.

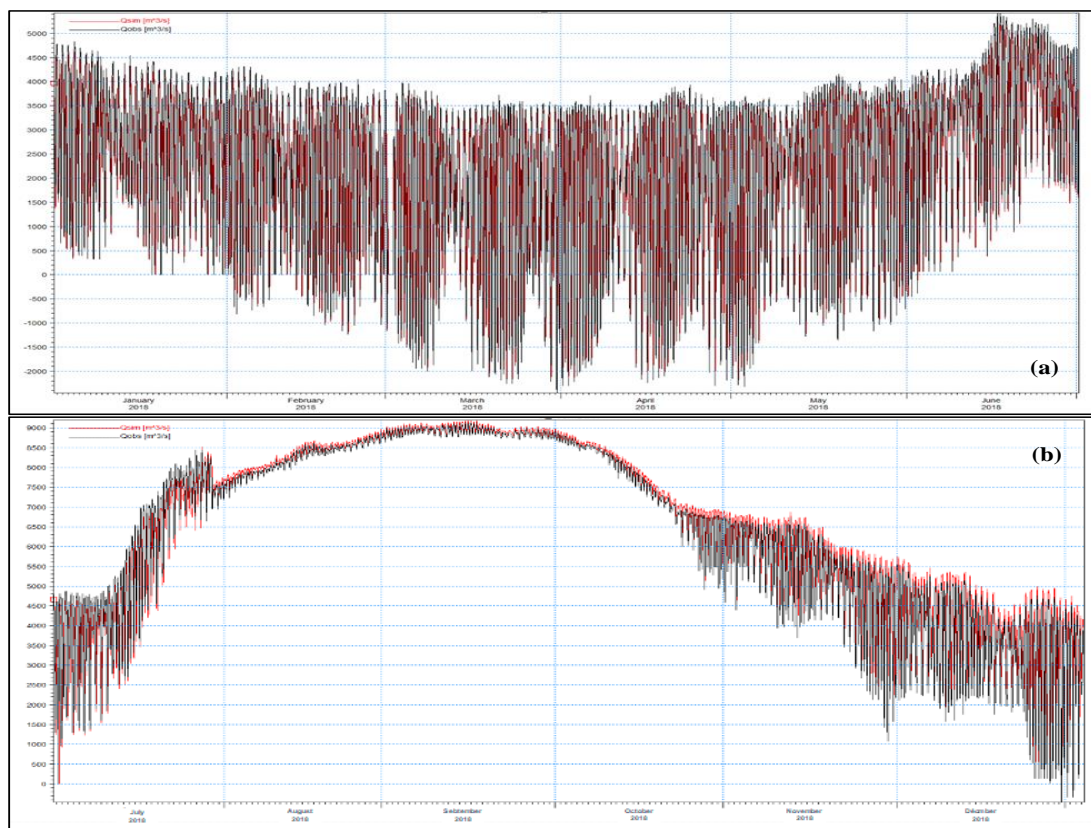


Figure 5. Results of verification discharge in Vam Nao station 2018.

3.2. Results of sediment transportation model calibration and verification

The results of calibration and verification show that the correlation index is relatively stable for the problem of sediment simulation - SSC and W_{bc} are 0.67 and 0.81 respectively, the Nash coefficient reaches a suitable value for the problem of sediment simulation - SSC's Nash is 0.67 and W_{bc} 's Nash is 0.77, especially the total error of the total amount reaches 6.54% - which is good (Figures 6-7 and Table 2).

From the total calculation data, it can also be seen that the seasonal change of sediment content is regular in accordance with the seasonal flow. Thus, the simulation results are good, showing that the model has high reliability.

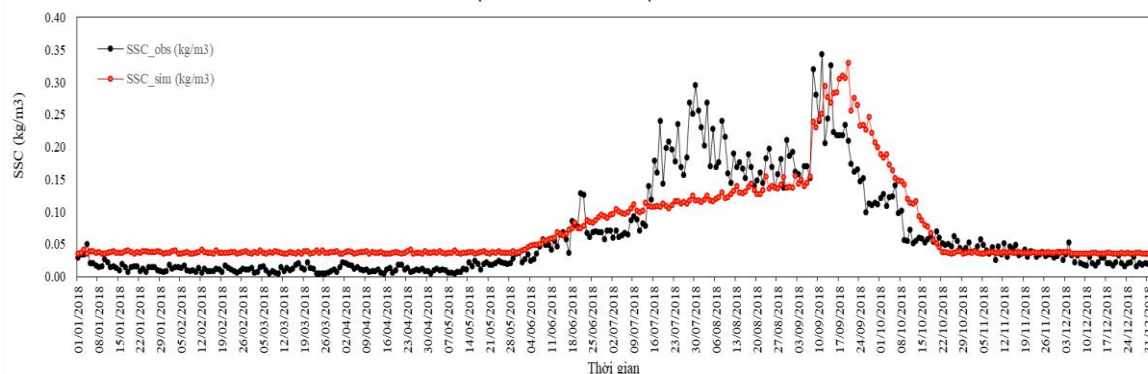


Figure 6. Results of calibration content of sediment (kg/m^3) in Vam Nao station.

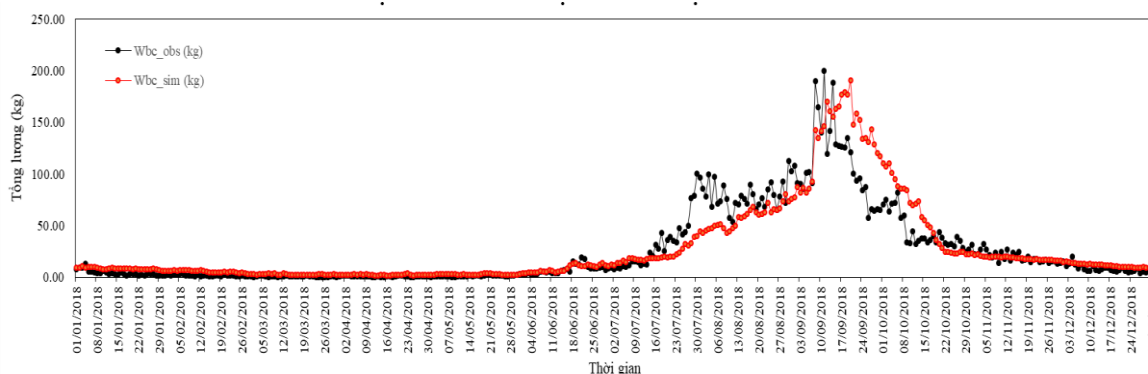


Figure 7. Results of calibration total amount of sediment (kg) in Vam Nao station.

Table 2. Results of calibration sediment in Vam Nao station.

Content of sediment in Vam Nao station	01/2018 to 12/2018		
	R^2	NASH	
	0.67	0.67	
Total amount of sediment in Vam Nao station	01/2018 to 12/2018		
	R^2	NASH	Total error
	0.81	0.77	6.54%

3.3. Simulation results of sedimentary changes

3.3.1. Water level and flow velocity

From the simulation results, it can be clearly seen that the difference between the largest and the lowest water level ($H_{\max}-H_{\min}$). This difference is also one of the causes of bank erosion in the area. In recent years, the landslide often occurs at the transition time between

the flood head and the dry season, when the water level recedes too deeply, causing the banks to collapse (Figures 8-10).

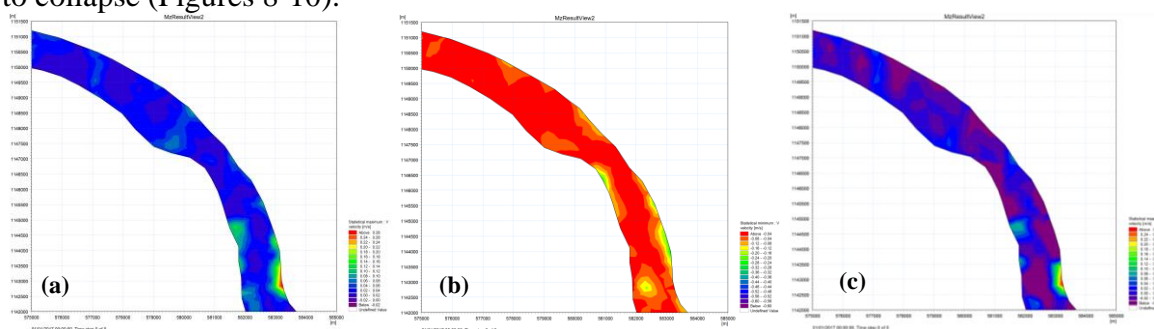


Figure 8. Calculation results of maximum (a), minimum (b), average (c) flow velocity in the study area.

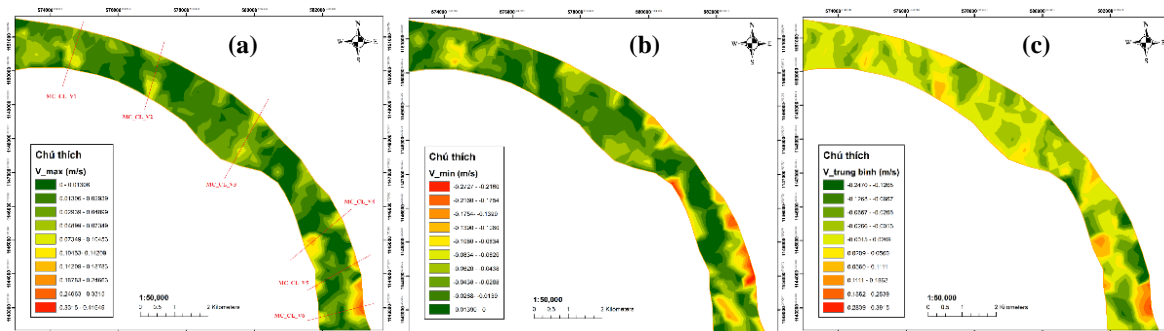


Figure 9. Map of maximum (a), minimum (b), average (c) flow velocity in the study area.

The variation of velocity is greatly influenced by the discharge regime from the headwaters and the ebb and flow of the tides. The location at Cao Lanh located on the Tien River has a higher input discharge, 80% compared to 20% of the Hau River, while the high tides at the estuaries remain unchanged, causing the tidal influence to increase, causing more or less influence on the flow rate, especially the amplitude $V_{max} - V_{min}$ in the direction from upstream to downstream.

Due to that reversible interaction, the flow direction on the Tien and Hau rivers changes with the seasons. Hydrodynamic simulation results show that, in the dry season, the river flows in two directions (both negative and positive); During the flood season, the current flows in only one direction from upstream to the sea.

In general, the main flow from upstream to downstream of the river section in Cao Lanh area tends to be concentrated on both banks, with the maximum velocity region appearing close to the shoreline, extending 7.0 km from the CL_V3 section to the CL_V6 section.

3.3.2. Simulation result sediment

The results of calculating the largest amount of displaced sediment are based on the results of the simulation of the sediment model from January 2017 to December 2019. The largest amount of displaced sediment is concentrated mainly on the right bank where there is a complex hydraulic regime - creating deep erosion holes (Figure 10).

The section of the Tien River flowing through Cao Lanh is a curved section with many pre-existing erosion holes - and most of them are displaced holes - creating a severe left bank erosion area. The largest amount of mud displaced varies from 0.91 kg/m^3 to 32.7 kg/m^3 .

At all sections, the largest amount of displaced sediment occurs on the right bank and ranges from 0.9 kg/m^3 to 2.7 kg/m^3 . The left bank area is an area of curved river, so the

amount of sediment removed is concentrated in this area. The research area at Cao Lanh is located under the sand mine, so the simulation process is quite affected by this problem.

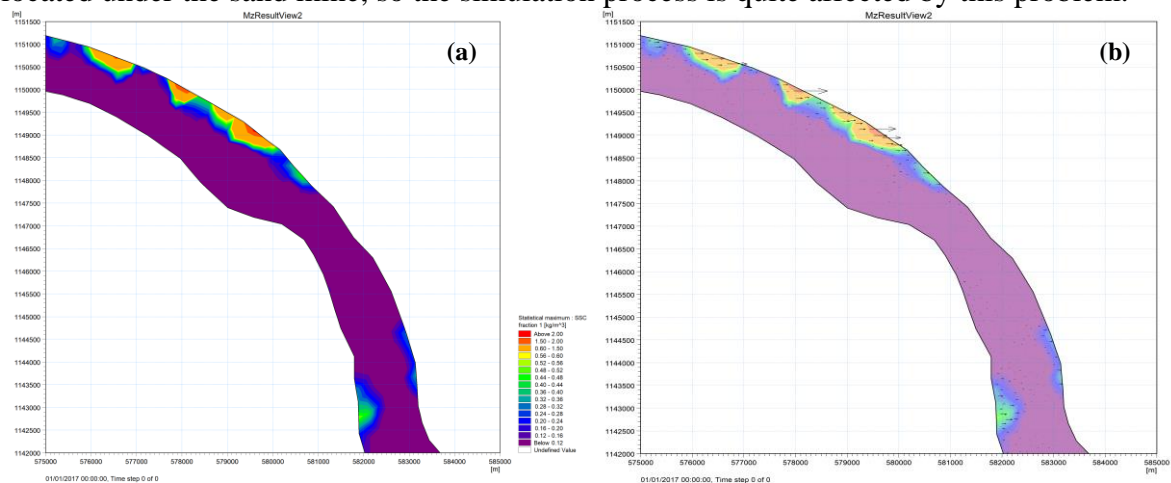


Figure 10. (a) Calculation results of the maximum concentration of sediment; (b) Direction of movement of the sediment.

3.4. Erosion trend in the study area

The simulation results show that, after 3 years, the total amount of sediment lost here and moved downstream is about $-218.7,106 \text{ m}^3$, the depth of erosion after 3 years is -233 cm , the average erosion speed is $-77.6 \text{ cm}/\text{year}$, where the deepest erosion can be up to -10.0 m (Figure 11).

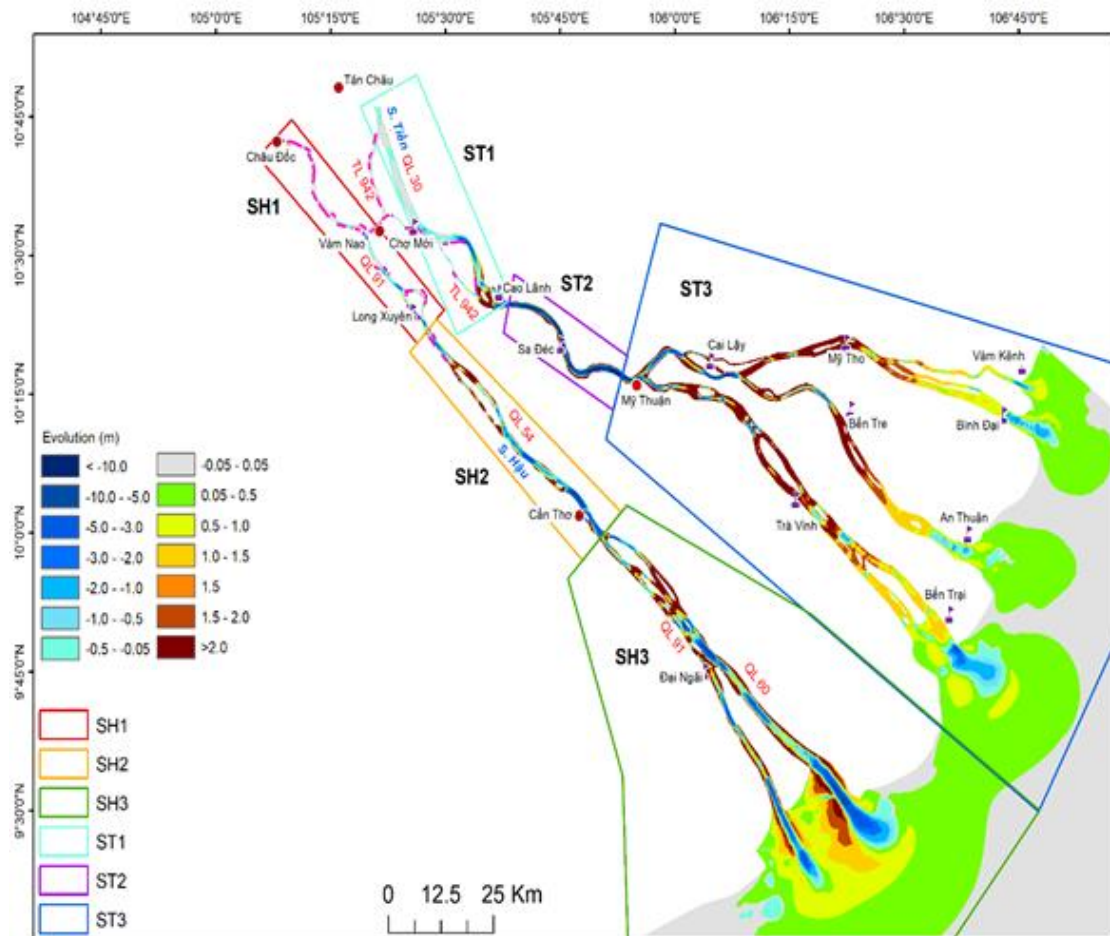


Figure 11. Morphological simulation results after 3 years (ST2 - area research).

Unlike the upstream area ST1, ST2 is considered as the middle area, so it can receive more sediments displaced from ST1, so the depth of erosion and loss of gradually decrease over time. However, this is an area with very high flow velocity, but it is curved, so the risk of landslides is great. This is an area where national highways QL30 and QL80 pass and in the future, it is necessary to have solutions to protect both sides of the river.

In general, the morphological characteristics of this area have a large degree of erosion and there is almost no large enough source of sediment to recover, the trend of deep erosion takes place and slows down over time. This is explained by the continuous deep erosion process, which increases the average wet section here, causing the flow velocity to decrease gradually, this area moves to a new equilibrium with decreasing phenomenon.

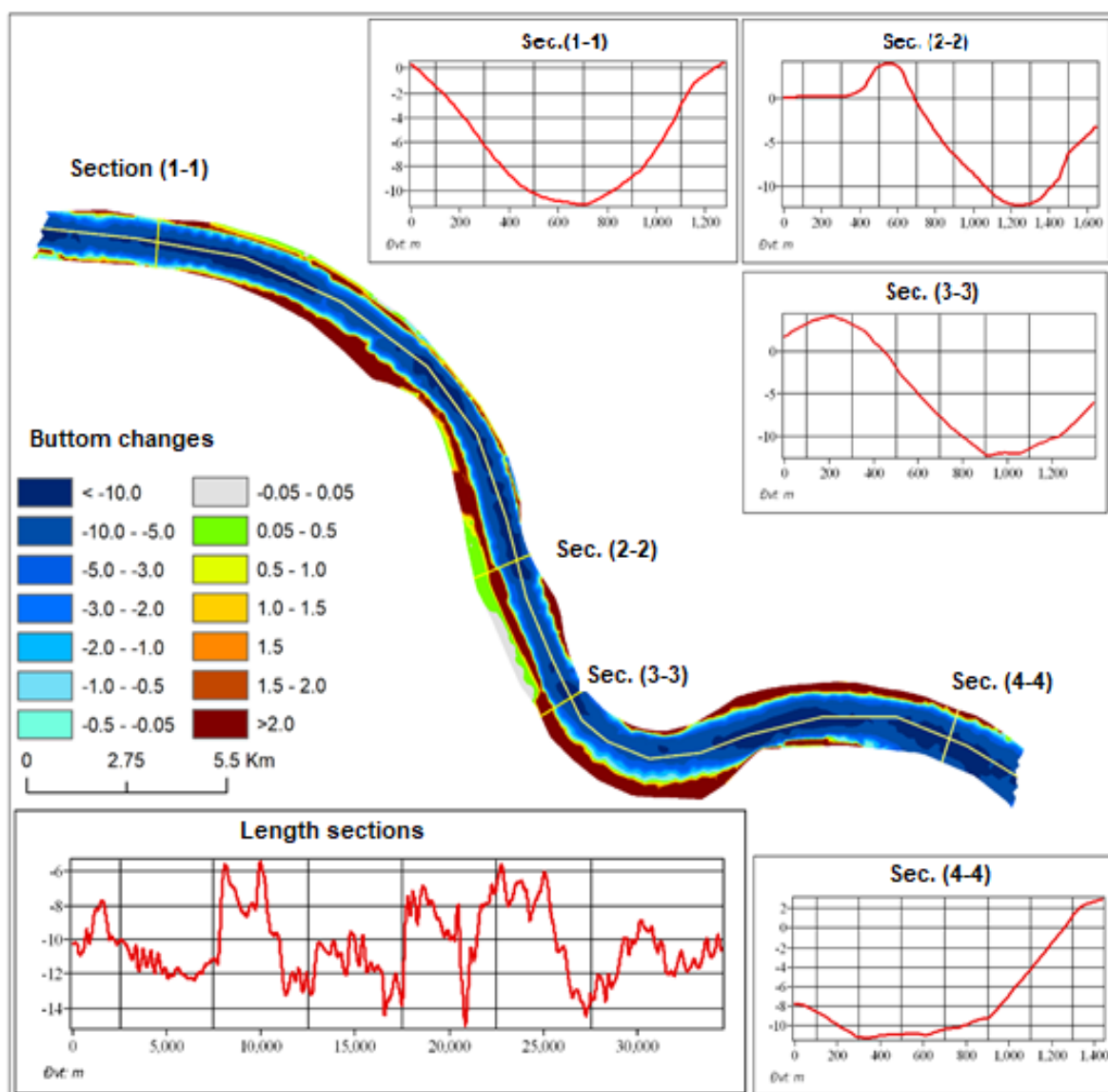


Figure 12. Morphological change of riverbed after 3 years.

The accumulation line of total sediment tends to go down, slow down over time and not be able to recover. The common feature of this area is that the accumulation line goes down sharply, due to the large flow rate, almost the amount of sediment moving from the upstream cannot settle here but is gradually carried out by the current towards the estuary. However, the simulation results show that, although the accumulation line goes down, it gradually decreases. Therefore, after many years, the ability to accumulate sediment here will gradually increase over time to re-establish a new balance (Figure 12).

4. Conclusion

By using mathematical modeling methods, specifically the Mike 21 FM model, the study calculated the sediment transport on the Tien River, passing through Cao Lanh district, Dong Thap province, thereby simulating the rate of erosion over a period of 3 years. The calculated results are highly reliable. The flow velocity in the river is unevenly distributed, at the bends that contribute to the increase in erosion, most evident at Sec. (2-2) and Sec. (3-3). The largest amount of sediment displaced ranged from 0.91 kg/m³ to 32.7 kg/m³. The total amount of sand moving is from the right bank and fluctuates from 0.9 kg/m³ to 2.7 kg/m³.

The trend of erosion in Cao Lanh district, Dong Thap province is shown as 12. The simulation results show that the total amount of sediment moving downstream is about -218,7106 m³, equivalent to 72.9 m³/year and the average erosion depth is -77.7 cm/year.

The results show that there is a certain suitability and sufficient reliability for the simulation of riverbed changes and can be used to calculate according to different input scenarios. The study area in Cao Lanh district tends to be dominated by erosion with accretion, which is consistent with the river topography. However, the limitation of the study does not consider the change of people's activities in the river and on the riverbank surface; does not consider the change of hydrogeological factors in the riverbank area; does not consider account the change of flow rate with hydrographic depth (3D); ... will cause certain errors in the landslide hazard index results.

In fact, the new study is just a simulation based on the model parameters that have been calibrated and tested in Vam Nao. Therefore, it is necessary to have an assessment with reality in the study area over a longer period to show the reality of the model results. This result will be improved in the next research.

Authors contribution statement: Research ideas, build scientific: N.T.K., C.T.V., Research methodology: N.T.K., C.T.V.; Data collection and processing: N.H.T., H.T.T.N.; Write the manuscript and correct the article: C.T.V., N.H.T.; Editing and finishing: C.T.V.

Acknowledgments: This article uses data, the result is the product of a project at the University of Natural Resources and Environment of Ho Chi Minh City, code CT.2023.06. In addition, the study inherits data from the project of the Ministry of Natural Resources and Environment, code: TNMT.2018.02.13. The authors gratefully acknowledge this support.

Competing interest statement: The authors declare no conflict of interest.

References

1. Son, N.T.; Duc, N.A. et al. Research to determine the cause of riverbank erosion and propose technology to warn and predict the level of riverbank erosion in some serious landslide areas in the Mekong Delta, Code: TNMT.2018.03.13. Project MONRE level, 2021.
2. Van, C.T. et al. Application of two-dimensional hydrodynamic model (MIKE 21FM) to simulate the sediment regime on Hau river, piloted in Long Xuyen city - An Giang province. *Sci. Technol. Dev. J.: Sci. Earth Environ.* **2021**, *5(SI2)*, 1–13.
3. Bravard, J.P.; Petit, F. Geomorphology of streams and rivers. *Encycl. Inland Waters* **2009**, 387–395. <https://doi.org/10.1016/B978-012370626-3.00043-0>.
4. Science and Technology Project at Ministry of Agriculture and Rural Development. Research on scientific and technological solutions to prevent sedimentation, stabilize flood drainage at Lai Giang estuary. National Key Laboratory of Rivers and Sea Dynamics, Vietnam Institute of Irrigation Science, 2008–2010.
5. State-level project: KC-08-29: Research and propose scientific and technological solutions to stabilize the riverbed downstream of Dong Nai and Saigon river systems for socio-economic development in the Southeast region. Southern Institute of Irrigation Science, 2005.

6. Reid, I.; Bathurst, J.C.; Carling, P.; Walling, D.E. (Eds): Applied fluvial geomorphology for river engineering and management, Chapter Sediment erosion, transport, and deposition. John Wiley and Sons, 1997, pp. 95-135.
7. Simon, A.; Collison, A.J.C. Quantifying the mechanical and hydrologic effects of riparian vegetation on streambank stability. *Earth Surf. Processes Landforms* **2002**, *27*, 527–546.
8. Fischenich, J.C. Channel erosion analysis and control. Proceedings of the Symposium on Headwaters Hydrology, American Water Resources Association, Bethesda Maryland, 1989, pp. 101–109.
9. Winterbottom, S.J.; Gilvear, D.J. A GIS-based approach to mapping probabilities of river bank erosion: regulated river Tummel, Scotland. *Regul. Rivers Res. Manage.* **2000**, *16*(2), 127–140. [https://doi.org/10.1002/\(SICI\)1099-1646\(200003/04\)16:2<127:AID-RRR573>3.0.CO;2-Q](https://doi.org/10.1002/(SICI)1099-1646(200003/04)16:2<127:AID-RRR573>3.0.CO;2-Q).
10. Blazejewski, R.; Pilarczyk, K.W.; Przedwojski, B. (Eds): River Training Techniques: Fundamentals, Design and Applications. Rotterdam; Brookfield, Vt., Balkema, **1995**, pp. 625.
11. Van, C.T.; Son, N.T.; Tuan, N.C. Research and experimental application of empirical formulas to calculate riverbank erosion in Tien River in Mekong Delta. *J. Environ. Sci. Eng. A* **2021**, *10*, 116–123. <https://doi.org/10.17265/2162-5298/2021.03.003>.
12. Te, V.T. et al. Research and forecast of sedimentation and erosion of the Dong Nai - Saigon river bed under the impact of the system of anti-flooding and environmental improvement works for Ho Chi Minh City area, Code: 21G/2009/HĐ-ĐHTL. Final report on state-level independent project, 2012.
13. Hung, L.M.; Ngoc, D.T.B. The empirical formula for calculating the bank erosion rate of the Tien river section in Thuong Phuoc area, Dong Thap province. *J. Agric. Rural Dev.* **2004**, *06*, 787–796.
14. Stephen, H.S.; Jia, Y. Simulation of sediment transport and channel morphology change in large river systems US-China workshop on advanced computational modelling in hydroscience & engineering. September 19-21, Oxford, Mississippi, USA, 2002.
15. Zuzana, A.; Mária, V.; Martin, J.; Michal, A.; Helena, H. Predicting the annual erosion rates on a small stream by the BANCS model. *Soil Water Res.* **2019**, *14*(4), 200–211. <https://doi.org/10.17221/58/2018-SWR>.
16. Hung, L.M., et al. Research on predicting erosion of the Mekong river bank. State-level science and technology projects. Southern Institute of Irrigation Science, 2001.
17. Hai, H.Q.; Trinh, V.T.M. Correlation between erosion - accretion in some areas of Tien and Hau river beds. *Earth Sci. J.* **2011**, *31*(1), 37–44.
18. Scott, S.H.; Jia, Y. Simulation of sediment transport and channel morphology change in large river systems US-China workshop on advanced computational modelling in hydroscience & engineering, September 19-21, Oxford, Mississippi, USA, 2002.
19. Final Report “Dong Thap province planning period 2021-2030, vision to 2050”, Dong Thap Province People’s Committee, 2022.
20. Ninh, L.V.; Giam, N.M. Climate characteristics of An Giang. *VN. J. Hydrometeorol.* **2017**, *648*, 18–26.
21. Hung, L.M. et al. Studying the influence of sand mining activities on changes in the channel of the Mekong River and proposing solutions to manage and plan reasonable exploitation, Code: 2010T/29. State-level independent scientific project, Southern Institute of Irrigation Science in the period, 2010–2013.
22. DHI. MIKE 21 & MIKE 3 Flow Model FM. Hydrodynamic Module. Scientific documentation, 2012.
23. DHI. MIKE 21 & MIKE 3 Flow Model FM. Hydrodynamic and Transport Module. Scientific documentation, 2012.

Research Article

Assessment of current water quality status in clam areas in Thai Binh Province and proposal for measures to improve efficiency

Nguyen Thao Truong Pham^{1*}, Phuong Minh Ta², Anh Minh Do³

¹ Institute of Ecology and Works protection, Thuyloi University;
thaonguyen22b@gmail.com

² School of International Education, Thuyloi University; phuongtm@tlu.edu.vn

³ Hanoi University of Natural Resources and Environment; dmanh@hunre.edu.vn

*Corresponding author: thaonguyen22b@gmail.com; Tel.: +84–967123798

Received: 05 July 2023; Accepted: 10 August 2023; Published: 25 September 2023

Abstract: This paper presents the results of water quality assessment of clam farming areas for 3 monitoring points in Tien Hai district, Thai Binh province. Using monitoring parameters including: Temperature, pH, Salinity, Alkalinity, N-NO₂⁻, N-NH₄⁺, H₂S, Coliform, Total Vibrio to assess water quality in clam culture area by using methods: The method of calculating the pollutant load due to domestic wastewater, the method of assessing the current state of the water environment based on national standards and the assessment method according to the water quality index (WQI). The results show that the monitoring points in the clam farming area of Thai Binh province: Temperature, pH and H₂S⁻ in the water are within the limits according to QCVN 10:2023/BTNMT; QCVN 02-19:2014/BNNPTNT and QCVN QCVN 08:2023/BTNMT. Salinity and alkalinity fluctuate greatly, the proportion of samples outside the permissible limits is 54.17% and 12.5%, respectively. N-NH₄⁺, N-NO₂⁻, have a high percentage of samples with values exceeding the permissible limit, ranging from 41.65 to 62.50% of the monitored samples. Coliform exceeded the limit from 2 to 256 times. The total Vibrio density was 20.83% of samples above the limit. The average water quality indicator on 3 monitoring locations has a percentage rating of Excellent: 20.83%, Good: 12.5%, Medium 12.5%, Bad: 37.5% and very bad: 16.67%. From the results of the assessment, this study suggests management measures, including improving water quality index used to zoning water quality, thus better managing clam areas; and technical measure which improves farming techniques to protect the aquatic environment of farmers.

Keywords: Clam; Thai Binh province; Water quality; WQI; Pollutant load.

1. Introduction

Clam is economic important aquatic species in Asia, especially in Malaysia, China, and Thailand [1]. However, the demand of aquaculture product [2] including of Asian Clam is increase rapidly, meanwhile environmental problems are one of the causes of clam mortality. In addition, the influence of microplastics and heavy metals is also the cause of quality deterioration of cultured clams [3]. Therefore, there have been studies focusing on this field, especially the issues mentioned above, but the monitoring and assessment of the environment is still limited [4].

In recent years, the coastal clam farming in Thai Binh has made strong progress and is always leading the northern provinces of our country in terms of area and annual clam production. Owing a 54-km stretch of coastline with various estuary systems flowing into the ocean, Thai Binh has a tidal flat area containing fertile sources of alluvium, therefore

making it for clam farming [5]. It is estimated by the Sub-Department of Fisheries - Department of Agriculture and Rural Development of Thai Binh that the province has developed 2,500 hectares for commercial clam farming in a total of nearly 3,200 hectares of intertidal clam farming area so far. Its trading production reached 122,500 tons in 2022, which accounted for 67.36% of the total aquaculture production. The revenue was worth over 2,400 billion VND, an increase of 321.28 billion VND in comparison to 2021, covering a proportion of 58.59% of the aquaculture value [6]. However, besides the achievements in production, there are also many difficulties faced by clam farmers, including problems of disease and environmental control.

The phenomenon of dead clam has often occurred in recent years, mass death on a large scale. Part of the reason is due to techniques and management methods such as raising too much density in some farming households. When clam density is too high, environmental quality deterioration or sudden change may lead to some death of cultured clams and when some of them die decomposing, rotting degrades the environment and kills others. According to a study [7] shows that the mass mortality of clams in the clam farms in Vietnam Tien Hai, Thai Binh usually occurs in most months of the year, however, in February to May every year, the density of dead clams is higher. The long dead time of each batch is about 20-30 days [8]. Therefore, the study objective is to assess the current state of water quality in clam areas in Thai Binh province and propose measures to improve efficiency.

2. Materials and Methods

2.1. Study area

Thai Binh is a coastal delta province, with 5 large estuaries flowing into the sea creating a large tidal area of about 25,000 ha, in which the highland and mid-tide areas are 7,000 ha, and the low-tidal areas 18,000 ha are very favorable for the development of saline and brackish aquaculture including clam farming [9]. For many years, farmers in Tien Hai district have invested in clam farming with an economic value of hundreds of billions of VND, contributing to improving the lives of fishermen. Tien Hai is a coastal district, located in the southeast of Thai Binh province, with a natural area of over 226 km², a population of over 23,000 people. With 23 km of coastline, Tien Hai has many advantages to develop a comprehensive marine economy in terms of exploitation, aquaculture, seafood processing and eco-tourism. In recent years, clam farming is Tien Hai's strength, in 2014, the total area

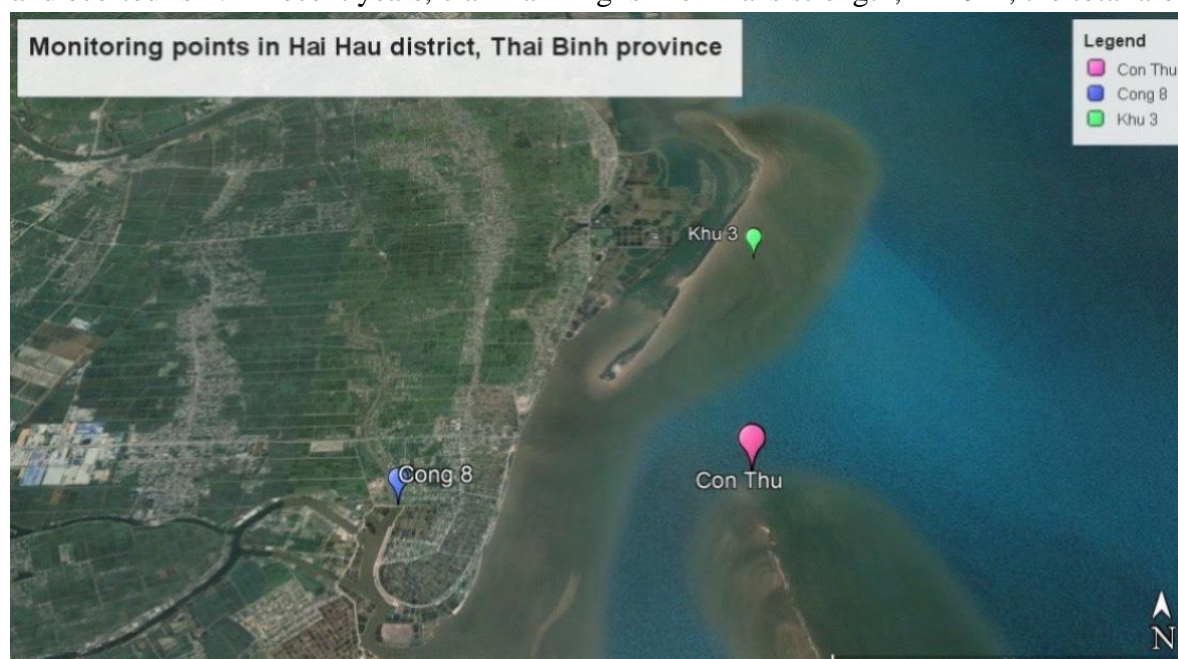


Figure 1. Location of the study area.

of clam farming in the whole district is about 2,370 ha, of which, nearly 2,000 ha of commercial clam culture and 374 ha of clam seed rearing. Clam farming in Tien Hai district has continuously developed in terms of area, productivity, output, economic efficiency and has become a profession that brings high income and great export value. Every year, the clam brings to Tien Hai hundreds of billions VND and creates more jobs for rural workers here. The warning time has a high risk of affecting the cultured clams such as heat wave, rain, and flood when factors such as salinity change greatly. The study area in Thai Binh was selected in Tien Hai district located in the sea gate (Figure 1).

2.1.2. Sampling

Three coastal sampling locations in Thai Binh province: Con Thu, Khu 3, Cong 8 with a frequency of 1 time/month. Water samples were collected into plastic bottles and kept cold and transferred to the laboratory for analysis of these parameters: Temperature, pH, Salinity, Alkalinity, N-NO₂⁻, N-NH₄⁺, H₂S, Coliform, total Vibrio. The monitoring period is from April to November 2022.

Sampling method according to (TCVN 5994:1995) “Water quality - Sampling - Guidance on sampling from natural lakes and man- made lakes” [10]. Preservation water samples according to (TCVN 6663-3:2016) “Water quality - Sampling - Part 3: Preservation and handling of water samples” [11]. Sampling time is at low tide in the month when the water is lowest in the day. This is the time when the water quality is at its worst.

2.2. Methods

2.2.1. Calculation of pollutant load due to domestic wastewater

In the study areas, clam culture wastewater is discharged directly into rivers, lakes and the sea, therefore, the potential load of pollutants due to domestic wastewater will in fact be calculated as the load of untreated wastewater.

To calculate the load of pollutants due to domestic wastewater of the area, based on the waste generation coefficient according to the following formula:

$$T = M \times H \tag{1}$$

where T is the contaminant load (kg/day); M is the number of people (people); H is the waste generation coefficient (g/person/day). H is taken based on calculations by the World Health Organization (WHO) calculated for many developing countries, the amount of pollutant released by each person daily into the environment for the case of primary treatment.

2.2.2. Monitoring method

The process of monitoring and data collection is shown in Figure 2.

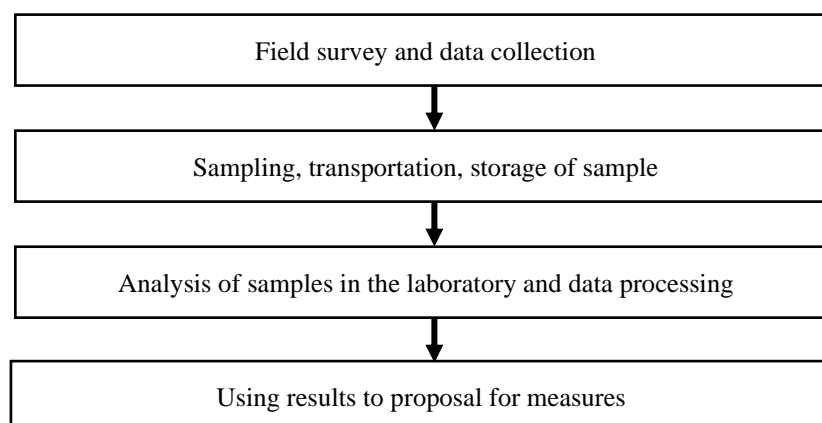


Figure 2. Flowchart of study structure.

Each monitoring parameter will use different analytical methods shown in Table 1.

Table 1. Parameter and analytical methods.

No	Parameter	Method	Location
1	Temperature,	Machine YSI Pro 1020	On-site
2	pH	Machine YSI Pro 1020	On-site
3	Salinity	Refractometer	On-site
4	Alkalinity	SMEWW 2320 B: 2011	Laboratory
5	N-NO ₂ ⁻	SMEWW 4500-NO2 B: 2017	Laboratory
6	N-NH ₄ ⁺	SMEWW 4500-NH3 F: 2017	Laboratory
7	H ₂ S ⁻	SMEWW 4500-S2- D:2017	Laboratory
8	Coliform	TCVN 6187-2:1996	Laboratory
9	Total Vibrio	Buller (2004)	Laboratory

2.2.2. The method of assessing the current state of the water environment is based on national standards

To assess the current state of water quality in the clam farming area for warning purposes, this study will rely on the issued national standards to evaluate each monitoring parameter. National standards applied for assessment include:

- National technical regulation on sea water quality (QCVN 10:2023/BTNMT) [12].
- National technical regulation on brackish water shrimp farming establishments - conditions to ensure veterinary hygiene, environmental protection, and food safety (QCVN 02-19:2014/BNNPTNT) [13].
- National technical regulation on surface water quality (QCVN 08:2023/BTNMT) [14].
- Procedures for quarantine of aquatic animals and aquatic animal products (TCN 101:1997) [15].

2.2.3. Index method WQI

Water Quality Index WQI is an index calculated from surface water quality monitoring parameters in Vietnam, used to provide a quantitative description of water quality and its use, expressed on a scale (Table 2). The study used the calculation of water quality index according to No. 1460/QD-TCMT dated November 12, 2019 [16].

Table 2. Levels of water quality assessment according to the WQI index.

WQI	Water quality	Color
91 - 100	Excellent: Good for domestic water supply	Blue
76 - 90	Good: Used for domestic water supply purposes but need to be treated appropriately	Green
51 - 75	Medium: Use for irrigation and other equivalent purposes	yellow
26 - 50	Bad: Used for navigation and other equivalent purposes	Orange
10 - 25	Very bad: Water is heavily polluted, need to be treated in the future	Red
< 10	Extremely: Water sources are polluted; water sources need to be remedied and treated	Brown

3. Results and discussion

3.1. Assessment of water quality in clam areas based on pollutant load

From formula (1), we have a table to calculate pollutant load of domestic wastewater in the clam farming area of Tien Hai district, Thai Binh province according to Table 3.

Table 3. Pollutant load due to domestic wastewater in the study area.

No.	Commune	Pollutant load (kg/day)					Grease
		TSS	COD	Nitrogen Total	Phosphorus Total	BOD ₅	
1	Nam Thinh	589.638	19.746	49.365	13.164	271.508	109.700
2	Dong Minh	905.365	30.319,2	75.798	20.213	416.889	168.440
	C _{max}	100		50	10	50	

Currently, domestic wastewater is not treated and discharged directly into rivers and sea, so the potential load of pollutants due to domestic wastewater will be calculated by: Amount of untreated wastewater. In Table 3, the pollutant load in all parameters because the wastewater of the 2 communes is very high, exceeding QCVN 40: 2021/BTNMT National Technical Regulation on industrial wastewater [17]. In which, Dong Minh commune has a higher coefficient than Nam Think commune because it has a larger population with TSS = 905,365 kg/day; COD = 30,319,2 kg/day; Nitrogen Total = 75,798 kg/day; Phosphorus Total = 20,213 kg/day; BOD₅ = 416,889 kg/day and grease = 168,440 kg/day.

From the calculation table of pollutant load due to domestic wastewater in the study area, we have the following chart:

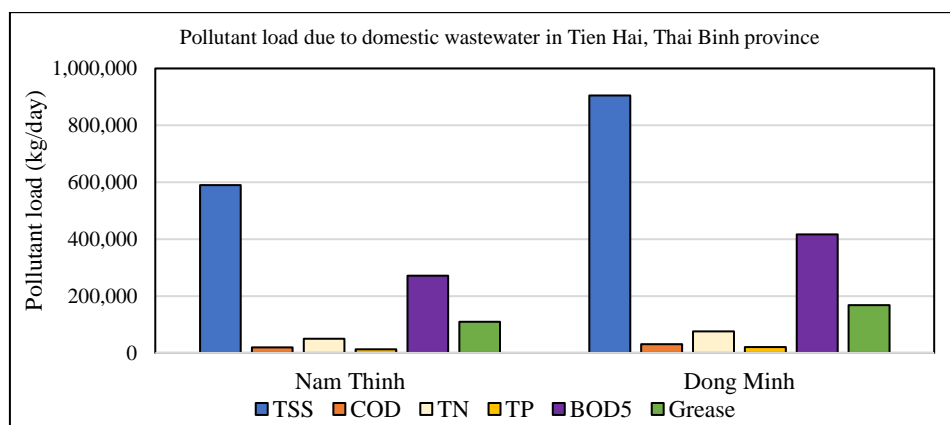


Figure 3. Pollutant load due to domestic wastewater in the study area.

Pollutant load varies due to different ranges of domestic wastewater in the study area. Particularly, Nam Think commune which has a smaller population, therefore, has a lower pollutant load (TSS = 589,638 kg/day; BOD₅ = 271,508 kg/day) in comparison to Dong Minh commune (TSS = 905,365 kg/day; BOD₅ = 416,889 kg/day).

3.2. Assessment of water quality in clam areas based on national standards

3.2.1. Group of basic water environment parameters

- The temperature: The water at the monitoring points in the clam culture area has an average temperature of 27.7°C. In November, the water has the lowest temperature at all monitoring points and the water in August has the highest temperature in the year (Figure 4). The water temperature at the monitoring points in general has a suitable value and has not affected the cultured clams. However, it is necessary to implement saving measures in the summer from July to September when the temperature reaches the highest and in the winter when the temperature drops. These extreme fluctuations will weaken the clams, causing mass mortality [18].

- The pH at the monitoring points has an average value of 7.82 (Figure 4). At the time of heavy rain [19], in June and October, the water has the lowest pH of the year (Con Thu = 6.99) and in August, the highest pH of the year (Khu 3 = 8.3) is approximately within the allowable limits (6.5-8.5), according to QCVN 10:2023/BTNMT. In general, the pH in farming areas in Nam Think and Dong Minh commune is in the appropriate range and does not change much.

- The average salinity of the water at the monitoring points is 9.1‰. The salinity here is often influenced by freshwater discharges from residential areas and craft villages, so there is a big fluctuation [20]. From May to October, at the time of heavy rain, the river water rises to the sea, so the salinity drops to the lowest (Khu 3 = 1‰), which is lower than the allowable limit, according to QCVN 10-MT:2015/ BTNMT. From November to April, it is the time of

little rain, so the salinity does not change significantly at the monitoring points. Particularly, at the point of Khu 3, the highest salinity of 26‰ is within the allowable limits (5-35) according to QCVN 10:2023/BTNMT (Figure 4).

- Alkalinity at monitoring points has an average value of 87.85 mg/l. In September and October, the value ranges from 44 to 74 mg/l. In particular, Cong 8 (September, October) and Khu 3 (October) record the values which are below the allowable range according to QCVN 02-19:2014/BTNNT. This happens due to the influence of fresh water and especially fresh water from the in-field drains. In the period of November - August, the alkalinity is relatively stable, within the allowable range (60-180 mg/l) according to QCVN 02-19:2014/BTNNT.

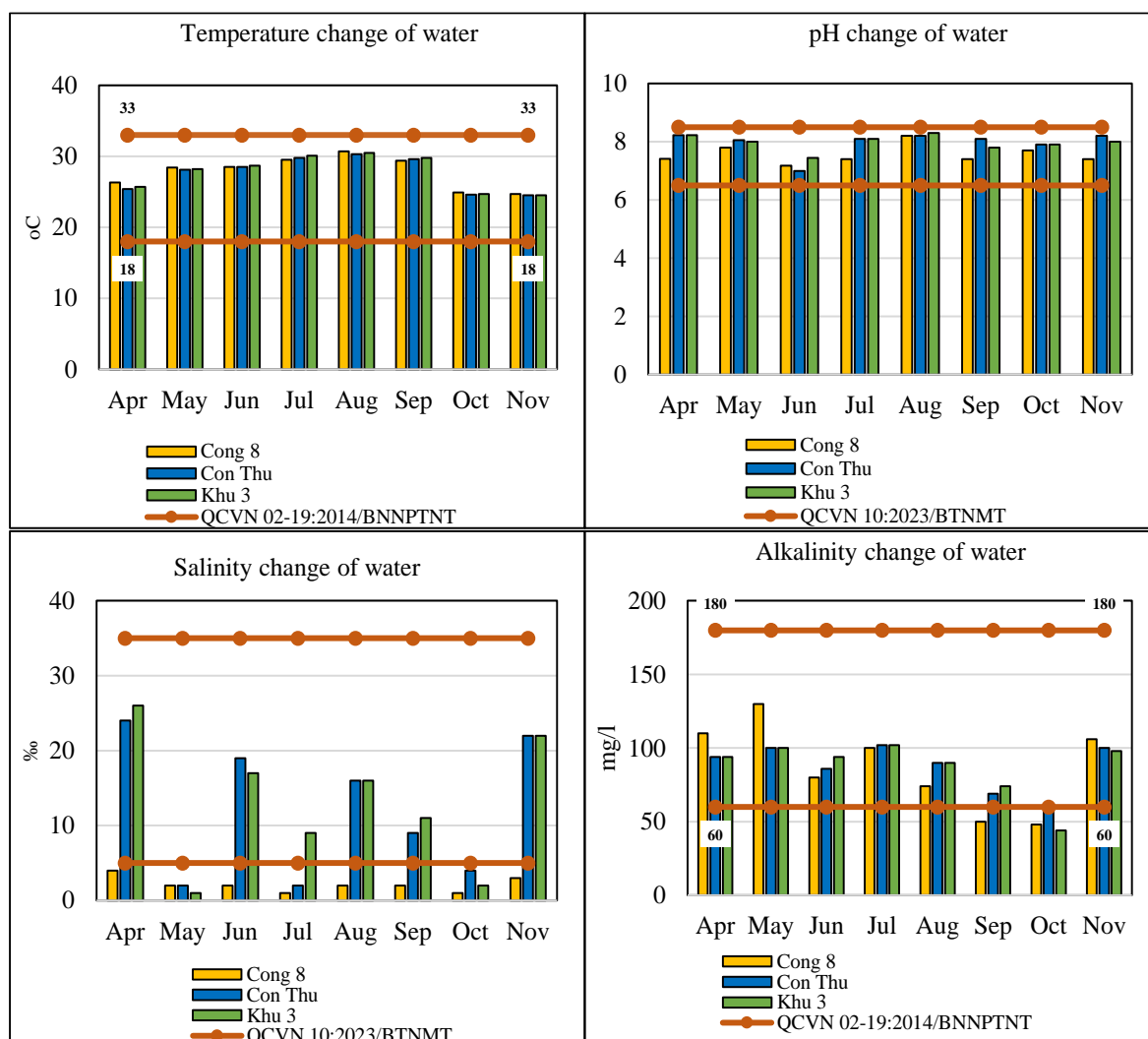


Figure 4. Changes in Temperature, pH, Salinity, Alkalinity of water clam areas 4-11/2022 in Tien Hai, Thai Binh province.

3.2.2. Nutritional parameter group

- The average concentration of $N-NH_4^+$ at the monitoring points is 0.359 mg/l (Figure 5). In which, from May to August, the concentration increased, exceeding the allowable limit according to QCVN 02-19:2014/BTNNT by 2.84 times (the highest in August at Cong 8 = 0.85 mg/l). The reason is that in the summer, the high temperature increases the decomposition of organic matter in the water, thereby increasing $N-NH_4^+$ and the impact of organic waste from the field. On the contrary, in September - April of the following year, the temperature decreases, leading to a decrease in the concentration of $N-NH_4^+$ within the allowable limit (< 0.03).

- The average nitrite ($N-NO_2^-$) content at the monitoring points is 0.053 mg/l (Figure 5). In which, from August to November, the $N-NO_2^-$ content is 2.3-2.5 times higher than the threshold of 0.05 mg/l according to QCVN 10:2023/BTNMT (the highest is in November at Cong 8 = 0.125 mg/l). In contrast, from April to July, the $N-NO_2^-$ concentration was low within the allowable range (the lowest was in July at Cong Lan 1 = 0.024 mg/l).

- Total sulfide (H_2S) in clam culture water has low value, average is 0.001 mg/l (Figure 5). There is no case with value higher than 0.05 mg/l according to QCVN 02-19:2014/BNNPTNT.

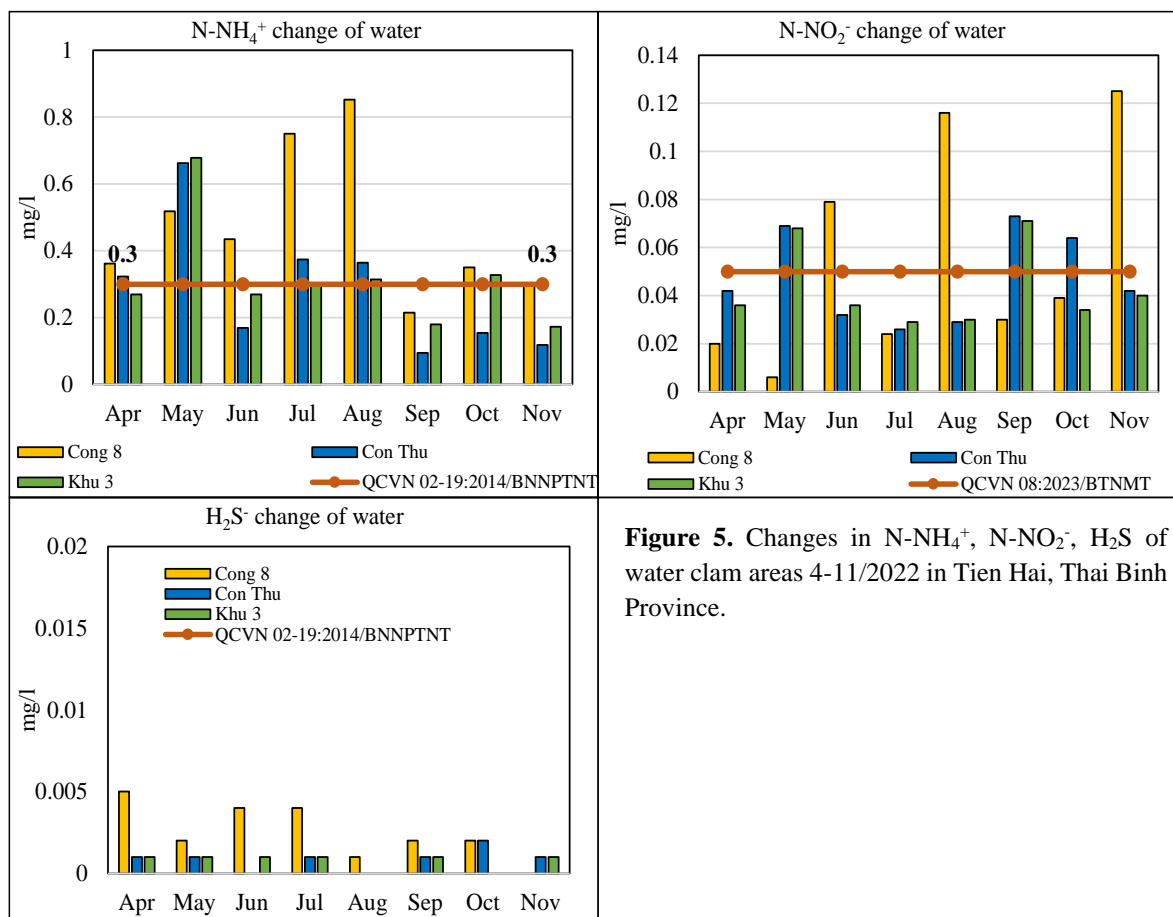


Figure 5. Changes in $N-NH_4^+$, $N-NO_2^-$, H_2S of water clam areas 4-11/2022 in Tien Hai, Thai Binh Province.

3.2.3. Density of Coliform, Vibrio total in water

- Total Coliform density in water of clam culture area has high value, average 51,633 (CFU/100 ml), at monitoring points in all months, Coliform density is higher than the allowable limit compared to QCVN 10:2023/BTNMT (the highest in July is 560 times higher) (Figure 6). High total Coliform density indicates that the culture water shows signs of contamination. This is a sign that the environment in the farming area is tending to be polluted, causing food insecurity.

- The total density of Vibrio at the monitoring points has an average concentration of 878 mg/l (Figure 6), the highest was in August at the monitoring point Ne (7,100 CFU/100 ml) exceeding the allowable limit 7.1 times according to TCN 101:1997 Quarantine process of aquatic animals and aquatic animal products. With a high concentration of Vibrio in water, there will be an increased risk of cultured molluscs being infected with bacterial pathogens that cause Vibrio spp.

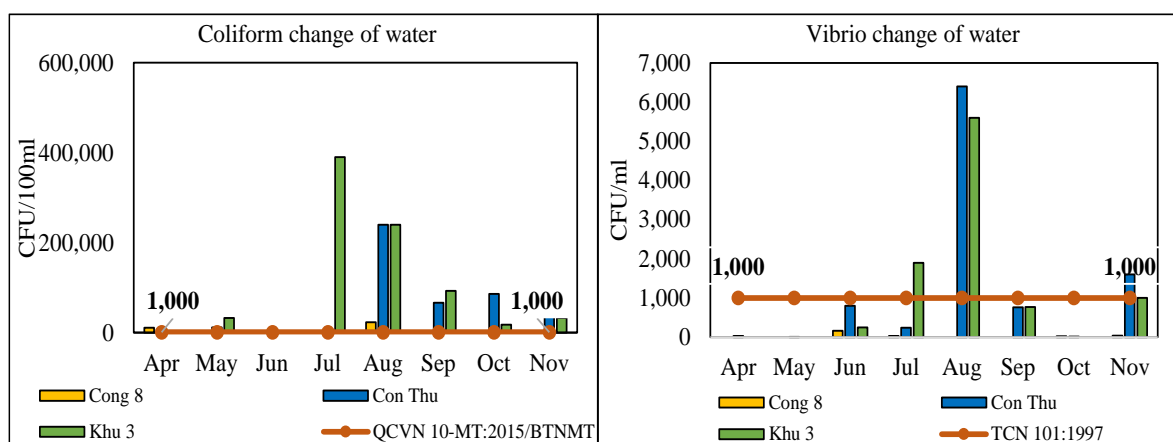


Figure 6. Change in Coliform, Vibrio of clam areas 4-11/2022 in Tien Hai, Thai Binh Province.

3.2.4. Overall rating according to the WQI index

The WQI index of the clam culture area is shown in Figure 7. At monitoring points with very bad WQI water quality index in May, August, and October. Excellent and good water quality occurs at Cong 8 in May, July, September, and October; at Con Thu in June and July; in Khu 3 in April and June. The rest of the other monitoring points have bad WQI for most of the month. The average water quality indicator on 3 monitoring locations has a percentage rating of excellent: 20.83%, good: 12.5%, medium 12.5%, bad: 37.5% and very bad: 16.67%.

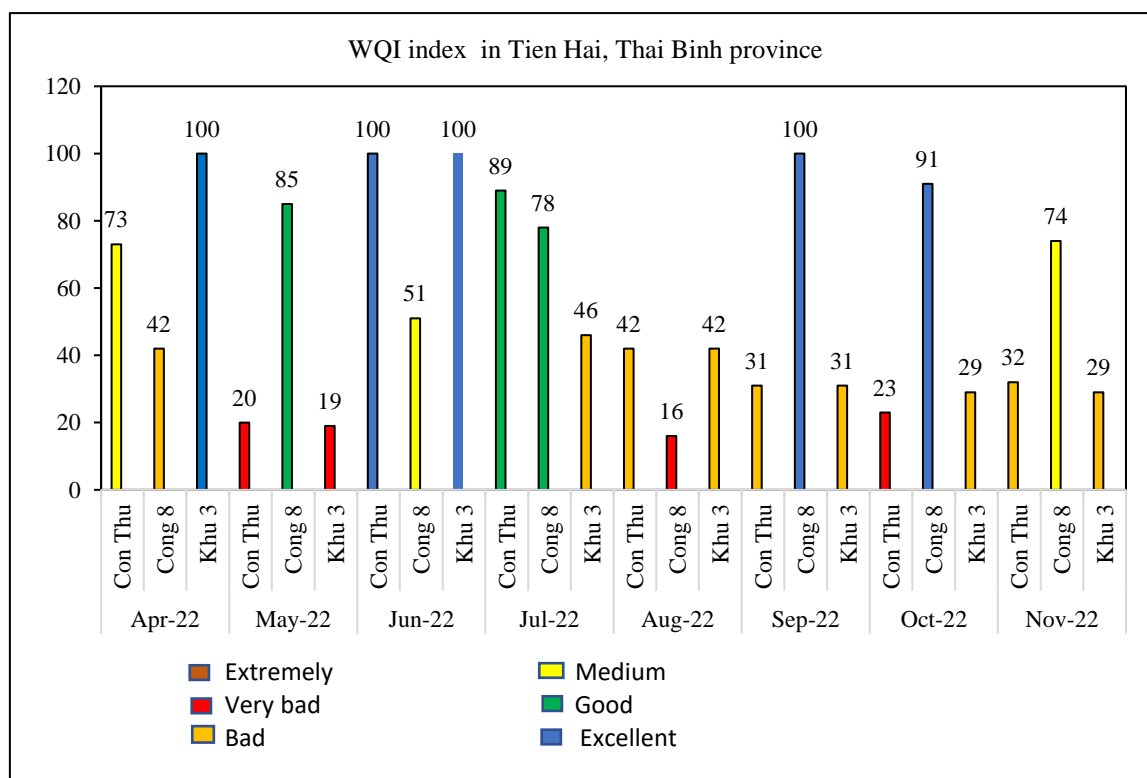


Figure 7. WQI index of water clam areas in Thai Binh province.

3.2.5. Proposed solutions

a) Management measures

- Strengthen the management, inspection, and assessment of the observance of the provisions of the law on environmental protection at clam farming establishments and households.

- Strengthen the inspection and technical guidance of farming, prevention of environmental pollution for organizations and individuals engaged in farming activities; strictly manage the supply of chemical materials on the market according to the State's regulations.

- Strengthening programs for monitoring, monitoring, and periodically warning about environmental and disease outbreaks in concentrated farming areas; monitoring water quality to forecast environmental developments as well as possible diseases, thereby taking timely solutions when problems occur.

- Instructing people to collect agricultural by-products, packages and tools containing chemicals used in production, farming, etc., for treatment at appropriate points in accordance with regulations; regularly take water samples periodically to check environmental factors and give advance recommendations to farming areas for farmers to proactively prevent.

- Building a model of community management in farming areas, focusing on discharging waste and infected wastewater in diseased ponds into the natural water environment, causing loss to farming communities in the area.

b) Technical measures

- At the time of high tide, to avoid sudden changes in salinity, the fisheries management agency should notify the irrigation management agency to coordinate the adjustment at the inland sluice point and the time to discharge water into the sea at the same time. high tide point. It is necessary to check the salinity in the water regularly, to handle it promptly.

- It is recommended that farmers notify management agencies promptly when detecting mass dead clams. It is necessary to monitor the progress and reduce the bacterial density such as: collecting garbage, dead clam carcasses, cleaning and disinfecting around the growing area... when the total density of *Vibrio* is high.

- To limit the influence of temperature on hot days that will make clams weak, farmers need to clean the rearing yard and stagnant water puddles. Clean cages, nets, remove garbage and dead clam carcasses to avoid environmental pollution, create ventilation, reduce coliform, and reduce food sources for clams, limit the influence of pathogenic bacteria at tide up and down.

- In the process of clam culture, people should pay attention to raising clams with low density, to avoid competition for food and increase the health of cultured clams. Inspect and harvest clam yards that have reached commercial size.

- According to the results of monitoring the farming area, from October to February next year, mass mortality of clams often occurs due to the influence of factors such as density of culture and the environment of the farming area with strong fluctuations in salinity, temperature, etc. Therefore, before entering the above time, farmers need to check, raise clams with low density, monitor the weather to take measures to protect cultured clams.

4. Conclusion

From the monitoring results, the water quality for clam culture in Tien Hai district, Thai Binh province is poor. Of which, 3/9 parameters are outside the allowable limits (temperature, pH, H₂S). Salinity and alkalinity have percentage of samples outside the permissible limits is 54.17% and 12.5%, respectively. N-NH₄⁺, N-NO₂⁻, total Coliform had a high percentage of samples with values exceeding the permissible limit. The total *Vibrio* density was 20.83% of samples above the limit. The average water quality indicator WQI on 3 monitoring locations has a percentage rating of excellent: 20.83%, good: 12.5%, medium 12.5%, bad: 37.5% and very bad: 16.67%. From there, it is necessary to have management and technical measures to limit the phenomenon of dead clams. From this study, in the future, the author proposes that there should be a common set of parameters to assess the quality of aquaculture environment and apply according to a common standard.

Authors contribution: Constructing research idea: N.T.T.P., M.P.T., A.M.D.; Select research methods: N.T.T.P., A.M.D.; Data collection: N.T.T.P., M.P.T., A.M.D.; Data processing: N.T.T.P., A.M.D.; Writing original draft preparation: N.T.T.P., M.P.T., A.M.D.; Writing review and editing: N.T.T.P., M.P.T., A.M.D.

Acknowledgments: The authors would like to thank the strong research group (Research of Organic Matter, ROOM), Environmental and Life Science Research Laboratory, Thuyloi University for their support during the research.

Conflicts of interest: The authors declare that this article was the work of the authors, has not been published elsewhere, has not been copied from previous research; there was no conflict of interest within the author group.

References

1. Chen, H.; Zha, J.; Liang, X.; Bu, J.; Wang, M. Sequencing and De Novo assembly of the sian Clam (*Corbicula fluminea*) transcriptome using the illumina GAllx method. *PLoS ONE* **2013**, *8*(11), e79516.
2. Zulhisyam, A.K.; Kabir, M.A.; Dawood, M.A.; Razab, M.K.A.A.; Ariff, N.S.N.A.; Sarkar, T.; Pati, S.; Edinur, H.A.; Mat, K.; Ismail, T.A. Effect of fish meal substitution with fermented soy pulp on growth performance, digestive enzyme, amino acid profile, and immune-related gene expression of African catfish (*Clarias gariepinus*). *Aquaculture* **2022**, *546*, 737418.
3. Sathish, M.N.; Jeyasanta, K.I.; Jamila, P. Monitoring of microplastics in the clam *Donax cuneatus* and its habitat in Tuticorin coast of Gulf of Mannar (GoM), India. *Environ. Pollute.* **2022**, *266*, 115219.
4. Nam, K.W.; Jeung, H.D.; Song, J.H.; Park, K.H.; Choi, K.S.; Park, K.I. High parasite burden increases the surfacing and mortality of the Manila clam (*Ruditapes philippinarum*) in intertidal sandy mudflats on the west coast of Korea during hot summer. *Parasites Vectors* **2018**, *11*, 42.
5. Thai Binh province web portal (thaibinh.gov.vn).
6. Thai Binh Statistics Office. Report on socio-economic situation of Thai Binh province in 2022, 2022.
7. Thuyet, D.B.; Dung, V.T. Current status of clam farming in some coastal provinces in the North and North Central, Vietnam. *J. Sci. Res. Dev.* **2013**, *7*, 972–980.
8. Thai Binh Department of Natural Resources and Environment. Report on the current state of the environment in Thai Binh province in the 2016-2020, 2020.
9. Thang, D.D.; Thai, H.T.; Hoa, V.V. Assessing the current situation and estimating the possibility of saline intrusion for the coastal area of Thai Binh province. *VN J. Hydrometeorol.* **2019**, *699*, 9–16.
10. QCVN 02-19:2014/BNNPTNT. National technical regulation on brackish water shrimp farming establishments - conditions to ensure veterinary hygiene, environmental protection and food safety, 2014. (In Vietnamese)
11. QCVN 08:2023/BTNMT. National technical regulation on Surface water quality, 2023. (In Vietnamese)
12. QCVN 10:2023/BTNMT. National technical regulation on marine water quality, 2023. (In Vietnamese)
13. QCVN 40:2021/BTNMT. National technical regulation on industrial wastewater, 2021. (In Vietnamese)
14. TCMT-Ministry TNMT. No. 1460/QĐ-TCMT QD-TCMT dated November 12, 2019 On the promulgation of Technical Guidelines for calculation and publication of Vietnam's water quality index (VN_WQI). TCMT, Ministry TNMT, 2019. (In Vietnamese)

15. TCN 101-1997. Procedures for quarantine of aquatic animals and aquatic animal products, 1997. (In Vietnamese)
16. TCVN 5994:1995. TCVN 5994:1995 (ISO 5667-4: 1987): Water quality-sampling-guidance on sampling from natural lakes and man-made lakes, 1995. (In Vietnamese)
17. TCVN 6663-3:2016. TCVN 6663-3:2016 (ISO 5667-3:2012) Water quality - Sampling - Part 3: Preservation and handling of water samples, 2016. (In Vietnamese)
18. Weber, K. Effect of temperature on the metabolic rate of diploid and triploid *Mercenaria mercenaria*. Fisheries and Aquatic Sciences. University of Florida, Florida. 2008.
19. Velez, C.; Figueira, E.; Soares, A.M.V.M.; Freitas, R. Native and introduced clams biochemical responses to salinity and pH changes. *Sci. Total. Environ.* **2016**, *566-567*, 260–268.
20. Shumway, S. A review of the effects of algal blooms on shellfish and aquaculture. *J. World Aquacult. Soc.* **2007**, *21*, 65–104.

Research Article

Residual and ecological risk assessment of Chlorpyrifos in coffee growing soil areas: A case study in Lam Ha district, Lam Dong province

Dang Viet Lam^{1,2*}, Vu Duc Toan³, Ta Minh Phuong⁴

¹ Chemical and Environmental Laboratory, Quality Assurance and Testing Center 1, Directorate for Standards and Quality, Ministry of Science and Technology; dangvietlam1980@gmail.com

² Graduate University of Science and Technology, Vietnam Academy of Science and Technology

³ ROOM Strong Research, Environmental and Life Science Research Laboratory, Thuyloi University; vuductoan@tlu.edu.vn

⁴ School of International Education Thuyloi University; phuongtm@tlu.edu.vn

*Corresponding author: dangvietlam1980@gmail.com; Tel.: +84-989655589

Received: 08 July 2023; Accepted: 12 August 2023; Published: 25 September 2023

Abstract: This study was conducted to investigate the residual of Chlorpyrifos (CPF) in coffee growing soil at Lam Ha district, Lam Dong province. Fifteen soil samples were collected from coffee intensive gardens in the Phi To, Nam Ha, Me Linh and Dong Thanh communes of Lam Ha district during the February 2023. The physico-chemical properties of the samples were analyzed such as pH, organic carbon, moisture content and mechanical composition of the soil while CPF was analyzed by gas chromatography-mass spectrometry. Soil samples with pH ranged from 3.48-4.45, moisture content 28.2-33.8% and OC 2.3-3.4%. Chlorpyrifos concentration of soil samples ranged from not detected to 954 µg/kg. The ecological risk of chlorpyrifos residual in soil was evaluated by using the risk quotient (RQ). The results of this study will be used to propose solutions to reduce pollution.

Keywords: Chlorpyrifos; Pesticides in soil; Soil pollutions; Risk assessment.

1. Introduction

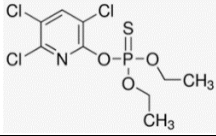
Chlorpyrifos (CPF), also known as Chlorpyrifos Ethyl or O,O-Diethyl O-(3,5,6-trichloropyridin-2-yl) phosphorothioate, is a chemical that belongs to the organophosphorus group is widely used to control pests and diseases. CPF persists for a long time in the environment, has the high bioaccumulation potential, affects the nervous system of humans and other animals [1–3].

CPF is considered as class 2 of hazardous to humans by the World Health Organization. In the United Kingdom, the use of CPF was banned from April 2016. From 2020, CPF was banned throughout the European Union and August 18, 2021, the U.S. Environmental Protection Agency (EPA) announced a ban on the use of CPF on food crops in the United States [4–6]. Due to its high toxicity and adverse effects on the environment, according to Circular 10/2020/TT-BNNPTNT, effective from October 25, 2020: pesticides containing CPF will not be produced or imported, only sold used until February 12, 2021.

In the world, there are many studies on residual as well as risk assessment of CPF in soil, water and in agricultural products. Typical pesticide residue studies include Determination of Chlorpyrifos Residues in Lettuce [7], pesticide contamination in soil of intensive horticulture [8] and pesticide residues in orchard soil [9]. In addition, studies on the

ecological risk of pesticides have been conducted in Ethiopia [10], USA [11], Nepal [12–13] and Iran [14] which have provided important information for future.

Table 1. Physical chemical properties of CPF.

Structure	
Chemical name	O,O-diethyl-O-(3,5,6-trichloro-2-pyridyl) phosphorothioate
Molecular Weight (g/mol)	350.6
Empirical and Structural Formula	C ₉ H ₁₁ Cl ₃ NO ₃ PS
CAS Registry Number	2921-88-2
Melting point (°C)	41.5-42.5
Vapor pressure (mmHg)	2.03E-05 at 25°C
Density (g/mL)	1.51 at 21°C
Solubility in water (g/L) at 25°C	1.12
Partition coefficient (n-octanol and water)	log K _{ow} = 5.1

There are very few studies on the residual of pesticides in the soil as well as no research on CPF contamination in the coffee growing soil in Viet Nam. Evaluation of total DDT residues in soil at the plant protection chemical warehouse in Nam Dan, Nghe An [15], residues of pyrethroid pesticides in soil, water, and watercress in Vinh Long [16] and validation of analytical procedures for chemicals such as CPF and carbosulfan in broccoli [17] as well as CPF in soil [18] are among the outstanding studies on the residual of pesticides in Viet Nam.

Lam Ha district is located in the northwest of Lam Dong province, with an altitude of 800-1000 m above sea level, the average annual temperature is about 21-22°C. Lam Ha area is mainly red soil, alluvial soil, and gray soil suitable for industrial crops such as coffee, pepper, vegetables, flowers, and fruit trees. In 2019 and 2020, Lam Ha has a coffee growing area ranking second in Lam Dong province. The plan by 2025 Lam Dong has about 170,000 ha and the output is from 530,000 to 550,000 tons/year with 5 large-scale specialty coffee growing areas: Di Linh, Lam Ha, Bao Lam, Duc Trong, Da Lat city and Lac Duong district.

Lam Ha district is the area with the strongest crop restructuring in Lam Dong province, with a mixture of industrial plants, vegetables, flowers and fruit trees, so the trade in using pesticides is very diverse for many different crops. The transfer of crops also leads farmers to have a habit of using pesticides for short-term plants in combination with coffee plants to prevent pests and diseases. Therefore, the amount and frequency of use of pesticides in Lam Ha will lead to a higher risk of pollution than other coffee farming areas of Lam Dong province.

According to the habit, pesticides are often purchased and stored at warehouses. State agencies only manage at companies and agents that trade in pesticides, but have not fully controlled the situation of using them in warehouses of farmers. Therefore, there are a number of pesticides that have been banned from use, but still in large quantities in households.

The main objectives of the study include: (1) Analysis of physicochemical properties, mechanical composition of soil samples; (2) Analysis of CPF concentration of soil samples; (iii) Evaluate ecological risk of CPF.

2. Materials and methods

2.1. Research plan

To achieve these objectives, previous studies on the residues and pollution of CPF were investigated. Soil samples were collected and analyzed for physicochemical properties and

CPF concentration to assess ecological risk. This study also aims to make recommendations to reduce the risk of environmental pollution. The details of the research plan are shown in Figure 1.

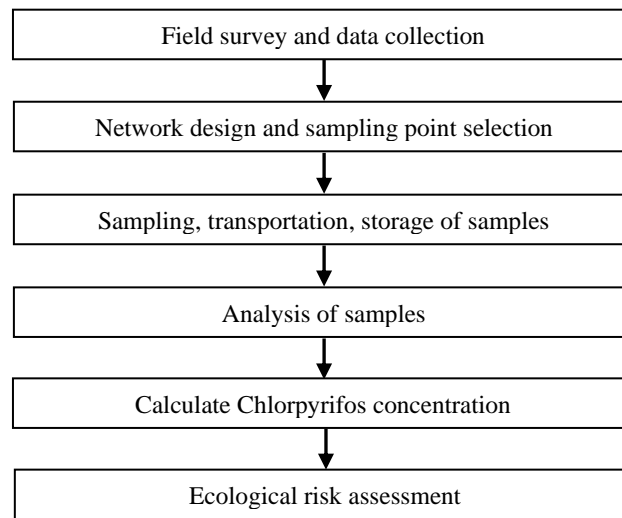


Figure 1. Research diagram.

2.2. Study area

Fifteen soil samples were taken in communes with intensive coffee growing areas of Lam Ha district, namely Dong Thanh, Me Linh, Nam Ha and Phi To at locations as shown in Figure 2. Based on the situation of pests and diseases and the habits of farmers, the sampling time is selected as 3 times per year including February, November (dry season) and June (rainy season).

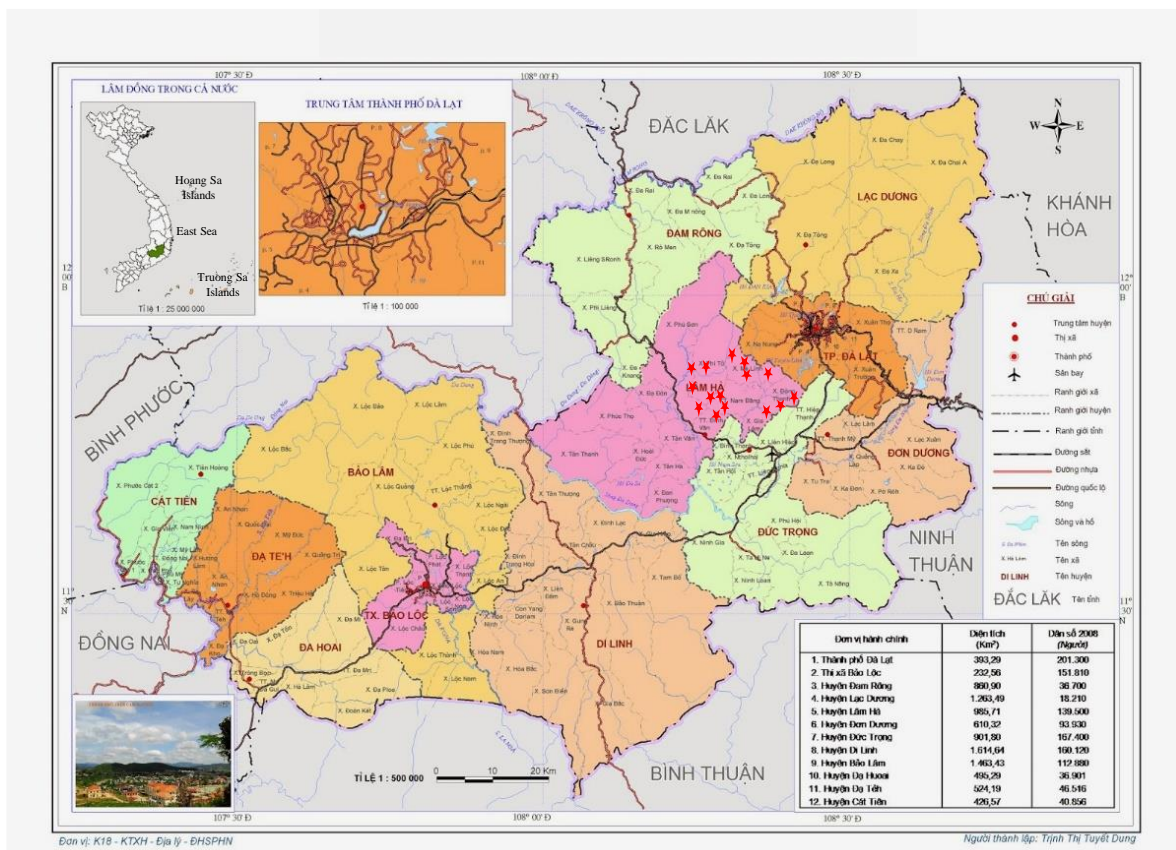


Figure 2. Sampling locations in Lam Ha district.

2.3. Sampling methods

Samples were taken according to the depth from 0-15 cm at the canopy point of the coffee tree to assess the level of retention in the environment of CPF. For square or rectangular gardens, the soil sample is taken diagonally: 1 point is the intersection of 2 diagonals and the remaining 4 points are located on 2 diagonals but about 2-3 rows of coffee trees from the outside. For irregularly shaped gardens, soil samples were taken in a zigzag pattern to ensure representative samples. The number of samples depends on the area of the garden.

At a garden, take 1 bulk sample including at least 5 sub-samples but not more than 10 sub-samples. After removing stones, gravel, roots and leaves, each subsample was taken about 0.5-1 kg, mixed well, and then used the method of quartering to reduce it to about 1kg, put in a dedicated clean nylon bag. Record the sample information and then transfer it to the laboratory for analysis.

2.4. Analysis methods

The pH is determined according to Vietnamese standards TCVN 5979:2021 by soaking the dried, finely crushed samples with a volume of KCl solution at a ratio of 1:5, shaking for about 1 hour and soaking for 1-3 hours, then measure pH at $20 \pm 2^\circ\text{C}$.

Soil moisture is determined according to TCVN 4048:2011 by calculating the percentage of water vapor lost when soil samples are dried at 105°C to constant weight.

Organic Carbon is determined according to TCVN 8941:2011 by oxidation with potassium bichromate solution in concentrated sulfuric acid. Titrate excess potassium dichromate with Fe(II) salt solution. Calculate the result from the weight of the test sample, the concentration of Fe(II) salt solution, the titration volume of the blank and samples.

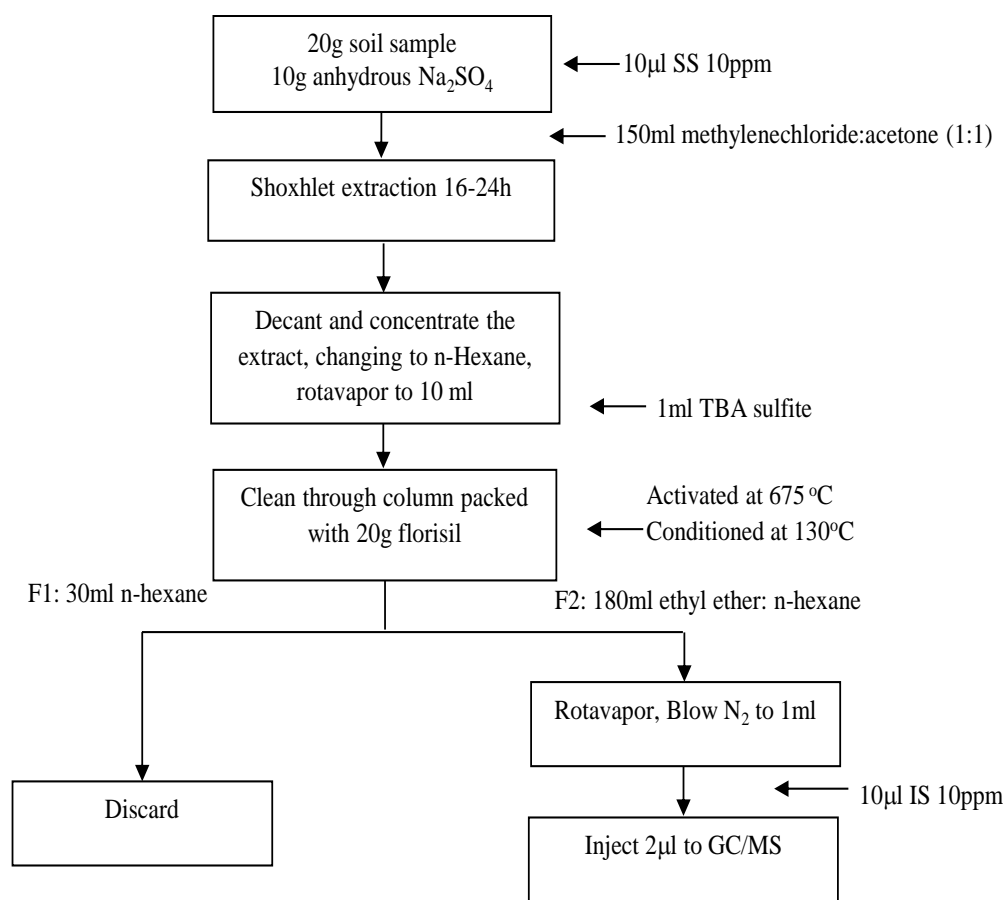


Figure 3. Schematic diagram of analysis of CPF in soil samples.

The mechanical composition of the soil was tested according to Vietnamese standard TCVN 8567:2010. This method uses a mixture of sodium hexamethaphosphate (NaPO₃)₆ and sodium carbonate Na₂CO₃ solutions to separate the grain levels of soil samples. Determine the composition of sand by sieve and the composition of limon and clay by pipette. Mechanical composition according to the international system includes 4 levels: Coarse sand (2-0.2 mm), Fine sand (0.2-0.02 mm), Limon (0.02-0.002 mm) and clay (< 0.002 mm).

Analytical methods for concentration of CPF in the soil are: US EPA method 3540C for extraction, US EPA method 3620C for cleanup and US EPA method 8270D for analysis [17–18]. The Schematic diagram for analysis of CPF concentration is depicted in Figure 3. Soil samples were dried, finely crushed and then shoxlet extracted with a mixture of dichloromethane: acetone solvents with a ratio of 1:1 in volume for 16-24 hours. Collect the extract and evaporate to about 10ml and then transfer to n-Hexane solvent. Add TBA sulfite solution to remove S²⁻ in the sample. Clean through a Florisil column containing an anhydrous NaSO₄ layer, rinse the column with n-hexane, and then elute with an ethyl ether:n-hexane solvent mixture. Collect the eluate, blow in N₂ stream to final volume 1ml and analyze on GC-MS instrument. The GC-MS operating conditions are shown in Table 2 [19–20]. CPF concentration is calculated from the results of the calibration curve and the soil sample in ug/kg.

Table 2. Operating conditions of GC/MS equipment for the analysis of CPF.

GC conditions	Capillary column: DB5-MS (30m × 0.32mm × 1µm) Program temperature: 70°C to 150°C [25°C/min] → 280°C [7°C/min, 4 minutes] Carrier gas: He (99.999%) Sample pump port temperature: 250°C Sample injection time: 1 minute Column flow rate: 1.7ml/min Sample pump mode: split flow Sample injection volume: 2µl Control mode: linear velocity Line split ratio: 10
MS conditions	Interface temperature: 280°C Potential for ionization: 70eV Observation mode: Ion selection (SIM)

2.5. Method validation

Repeat the analysis 7-10 times with a sample containing CPF concentration of 3-5 times the estimated limit of detection to calculate the limit of detection (LOD) and the limit of quantification (LOQ). Two analysts performed in parallel to calculate repeatability and reproducibility. Add standards at three levels of concentration: low, medium, and high to calculate the recovery yield. From the results of the repeatability, reproducibility and recovery calculate the uncertainty of the method applied in the laboratory. The method validation results for the determination of CPF in the laboratory were: LOD 1 µg/kg, LOQ 3 µg/kg and uncertainty 11.86%.

2.6. Risk assessment

In this study, the risk quotient (RQ) is used and calculated according to the following formula [13, 23]:

$$RQ = C / PNEC \tag{1}$$

where C is the concentration of the pollutant analyzed in the sample; PNEC is the concentration value predicted to have no effect on the organism.

$$PNEC = NOEC / AF \tag{2}$$

where NOEC is the concentration with no effect observed; AF is the rating factor.

Evaluate the levels of risk obtained according to the range of values of the RQ: (1) $RQ < 0.01$: very low risk; (2) $0.01 \leq RQ < 0.1$: low risk; (3) $0.1 \leq RQ < 1$: moderate risk; (4) $RQ \geq 1$: high risk.

3. Results and discussion

3.1. Physicochemical properties of the soil

The soil samples for intensive coffee cultivation in 4 communes of Lam Ha district are acidic, in which Phi To commune has the lowest pH values in the range of 3.48-3.54, Nam Ha and Me Linh communes have similar pH values in the range 3.72-4.45 and 3.96-4.28, respectively. Dong Thanh commune has the highest pH in the range of 4.25-4.33. It is necessary to increase to neutral pH such as lime powder application because the most suitable pH range for coffee growing soil from 4.5-6.0 [24].

The moisture content of 15 soil samples is not much different, ranging from 28.2-33.8%, suitable for plants to grow. The organic carbon concentrations are in the range of 2.3-3.6%. Some samples with low OC% need improvement plans such as in Phi To and Nam Ha communes because the optimal conditions for coffee to grow at an OC% are equal to or greater than 2.5% [24].

All 15 soil samples are mixed clay with clay content of 39.67-66.86. The soil samples in Phi To and Me Linh communes are clay-rich soils with the percentage of mechanical components not much different with the percentages of coarse sand, fine sand, limon and clay in the range of 2.75-2.92, 8.97-11.64, 21.26-22.75 and 62.90-66.86 while in Nam Ha and Dong Thanh communes there is a relatively large difference in percentage of limon and clay. The percentages of coarse sand, fine sand, limon and clay in the soil ranged from 2.49-2.93, 12.58-19.11, 22.83-39.06 and 39.67-61.00, respectively.

3.2. CPF concentration of soil samples

From the weight of the soil sample, the final solvent volume, the mass spectrum in the sample and the standard curve, we can calculate the concentration of CPF with the unit of $\mu\text{g}/\text{kg}$. CPF concentrations of 15 soil samples in 4 communes of Thanh Ha district are presented in Table 3.

Table 3. CPF concentration of soil samples.

Sample	location	Number of Sample	CPF concentration ($\mu\text{g}/\text{kg}$)		
			Min	Average	Max
Phi To communes		3	Not detected	31.7	65.7
Nam Ha communes		5	Not detected	75.5	175
Me Linh communes		4	389	543	954
Dong Thanh communes		3	422	593	821

From CPF concentration of fifteen soil samples in Lam Ha district, we found that Phi To and Nam Ha communes have lower CPF levels than the other two communes, Me Linh and Dong Thanh. Soil samples in Phi To commune had the lowest CPF concentration with 1 sample not detected and maximum concentration was $65.7 \mu\text{g}/\text{kg}$. Nam Ha Commune had 2 samples without CPF detected, the average concentration is twice as high as that of Phi To commune and the maximum concentration is $175 \mu\text{g}/\text{kg}$. The CPF concentrations of soil samples in Me Linh and Dong Thanh communes ranged from 389 to $954 \mu\text{g}/\text{kg}$, higher than previous research results.

Although CPF has been banned in Vietnam since February 2021, some pesticide suppliers and farmers continue to trade and use it illegally. The main source of CPF in soil

samples can be from pesticides used to control pests and diseases at the beginning of the rainy season every year or can be remained from sprays before. Therefore, it is necessary to continue monitoring to evaluate the residual of CPF comprehensively.

CPF concentration is compared with result of previous studies in Table 4. The results obtained from this study were uneven: Some samples did not detect CPF but some samples were very high. These were substantially higher than a study of rice grow land at the Mekong Delta and studies at Nepal and Iran in 2021. This CPF result was lower than studies at Malaysia in 2010.

Table 4. CPF concentration ($\mu\text{g}/\text{kg}$).

Sample Locations	Type of sample	Year of sampling	CPF concentration ($\mu\text{g}/\text{kg}$)	Reference
Lam Ha	Soil	2023	Not detected - 954	This study
Mekong Delta	Land	2019	3.51-291	PhD thesis summary
Nepal	Soil	2021	32.5 - 177	Bhandari, G. [13]
Iran	Soil	2021	240-510	Arani, M.H. [14]
Malaysia	Land	2010	20 - 2240	Tahir, N.M. [25]

3.3. Risk assessment

With AF equal to 10 and NOEC equal to 65 ($\mu\text{g}/\text{kg}$) [23], risk index RQ were calculated in Table 5.

Table 5. Risk assessment.

Sample name	CPF concentration ($\mu\text{g}/\text{kg}$)	RQ	Risk assessment
Phito communes	Not detected-65.7	<1.0-10.1	Moderate- high risk
Nam Ha communes	Not detected-175	<1.0-26.9	Moderate- high risk
Me Linh communes	389-954	59.8-146.8	High risk
Dong Thanh communes	422-821	64.9-126.3	High risk

The results of the RQ index show that the ecological risk impact of CPF contamination in coffee soils in Lam Ha district is moderate to high and requires mitigation measures. The order of the communes with the risk from moderate to high in this study is Phi To, Nam Ha, Dong Thanh, and Me Linh, respectively. Soil samples detected with CPF are all moderate-highly toxic. Ecotoxicological information on pesticides and degradation products is not always available and should be incorporated in risk assessments. Furthermore, the ecotoxicity of the degradation product of CPF is higher than that of CPF itself. Higher level risk assessment methods to improve assessment risk should also be considered for a better understanding of pesticides.

4. Conclusion

The physicochemical parameters, mechanical composition and CPF concentration in 15 samples of coffee growing soil in Lam Ha were archived. CPF residual ranged from not detected to 954 $\mu\text{g}/\text{kg}$. This study assesses the ecological risk of CPF in soil based on the RQ risk quotient method, result showed all moderate-highly toxic. Due to the limited number of studies on risk assessment in Vietnam on CPF and other pesticides, it is necessary to promote studies in this direction using assessment methods such as: RQ risk quotient method, CR

cancer risk index method, distribution modeling method, matrix method to provide more information for authorities to manage the use of pesticides in agriculture and forestry. Further studies need to be carried out on a large scale with an increased number of samples and type of pesticides to get a comprehensive view of the status of pollution and ecological risks of pesticides in coffee growing soil in Lam Ha district.

Authors contribution: Constructing research idea: D.V.L., V.D.T.; Select research methods: D.V.L., V.D.T.; Data collection: D.V.L., V.D.T.; Data processing: D.V.L., V.D.T.; Writing original draft preparation: D.V.L.; Writing review and editing: D.V.L., V.D.T., T.M.P.

Acknowledgments: The authors would like to thank the Chemical and environmental laboratory, Quality assurance and testing center 1 and ROOM strong research, Thuyloi University for their support during the research.

Conflicts of interest: The authors declare that this article was the work of the authors, has not been published elsewhere, has not been copied from previous research; there was no conflict of interest within the author group.

References

1. Chlorpyrifos, Pubchem. Online available: <https://pubchem.ncbi.nlm.nih.gov/compound/Chlorpyrifos>.
2. Nallapaneni, A.; Pope, C.N. Chlorpyrifos. *Encyclopedia of Toxicology* (2nd Edition), 2005, pp. 583–585.
3. Koshlukova, S.E.; Reed, N.R. Chlorpyrifos. *Encyclopedia of Toxicology* (3rd Edition). 2014, pp. 930–934.
4. Wołejko, E.; Łozowicka, B.; Jabłońska-Trypuć, A.; Pietruszyńska, M.; Wydro, U. Chlorpyrifos Occurrence and Toxicological Risk Assessment: A Review. *Int. J. Environ. Res. Public Health*. **2022**, 19(19), 12209. <https://doi.org/10.3390/ijerph191912209>.
5. Solomon, K.R.; Williams, W.M.; Makay, D.; Purday, J.; Gidding, J.M.; Giesy, J.P. Properties and uses of Chlorpyrifos in the United States. *Ecological Risk Assessment for Chlorpyrifos in Terrestrial and Aquatic Systems in the United States*. **2014**, 231, 13–34. https://doi.org/10.1007/978-3-319-03865-0_2.
6. Sud, D.; Kumar, J.; Bansal, P. Toxicity, natural and induced degradation of Chlorpyrifos. *J. Chil. Chem. Soc.* **2020**, 65(2), 4807–4816. <http://dx.doi.org/10.4067/S0717-97072020000204807>.
7. Mai, S.; Ninga, E.; Cara, M.; Mukaj, M. Determination of Chlorpyrifos Residues in Lettuce by GC MS/MS. *Proceeding of the 4th Global Virtual Conference*, April 18–22, 2016. *Agriculture, Forestry, and Fisheries*, 2016, pp. 285–287.
8. Gonçalves, C.; Alpendurada, M.F. Assessment of pesticide contamination in soil samples from an intensive horticulture area, using ultrasonic extraction and gas chromatography-mass spectrometry. *Talanta* **2005**, 65(5), 1179–1189.
9. Redondo, M.J.; Ruiz, M.J.; Boluda, R.; Font, G. Persistence of pesticide residues in orchard soil. *Sci. Total Environ.* **1994**, 156(3), 199–205.
10. Merga, L.B.; Mengistie, A.A.; Alemu, M.T.; den Brink, P.J.V. Biological and chemical monitoring of the ecological risks of pesticides in Lake Ziway, Ethiopia. *Chemosphere* **2021**, 266, 129214.
11. Gibson, J.E.; Peterson, R.K.; Shurdut, B.A. Human exposure and risk from indoor use of Chlorpyrifos. *Environ. Health Perspect.* **1998**, 106(6), 303–306.
12. Bhandari, G.; Atreya, K.; Scheepers, P.T.J.; Geissen, V. Concentration and distribution of pesticide residues in soil: Non-dietary human health risk assessment. *Chemosphere* **2020**, 253, 126594.

13. Bhandari, G.; Atreya, K.; Vašíčková, J.; Yang, X.; Geissen, V. Ecological risk assessment of pesticide residues in soils from vegetable production areas: A case study in S- Nepal. *Chemosphere* **2021**, *788*, 147921.
14. Arani, M.H.; Kermani, M.; Kalantary, R.R.; Jaafarzadeh, N.; Arani, S.B. Pesticides residues determination and probabilistic health risk assessment in the soil and cantaloupe by Monte Carlo simulation: A case study in Kashan and Aran-Bidgol, Iran. *Ecotoxicol. Environ. Saf.* **2023**, *263*, 115229.
15. Viet, T.Q.; Dung, D.T.; Ha, N.T.T.; Son, N.T. Preliminary assessment of environmental risks due to residues of pesticides in Nam Linh commune, Nam Dan district, Nghe An province. *VN J. Agric. Sci.* **2016**, *14(12)*, 1956–1963.
16. Nga, B.T.; Viet, L.Q. Current status of pesticide production and storage in soil and water on nasturtium officinale in Thuan An commune, Binh Minh district, Vinh Long province. *Sci. J. Can Tho Uni.* **2010**, *14*, 278–287.
17. Vu, L.D.; Nhan, T.V. Validation of the analytical method for residues of the pesticides chlorpyrifos and carbosulfan in broccoli by coupled chromatography-mass spectrometry (GC-MS/MS) combined with Quechers sample processing technique. *J. Sci. Technol. Ind. Univ. HCMC.* **2020**, *44*, 45–52.
18. Tat, T.Q.; Vien, D.M. Determination of analytical procedures for the active ingredient chlorpyrifos ethyl from soil. *VNU J. Sci.: Nat. Sci. Technol.* **2017**, *33(2S)*, 156–161.
19. Falaki, F. Sample preparation techniques for Gas chromatography. IntechOpen, 2019. doi:10.5772/intechopen.84259.
20. Tadeo, J.L.; Pérez, R.A.; Albero, B.; García-Valcárcel, A.I.; Sánchez-Brunete, C. Review of sample preparation techniques for the analysis of pesticide residues in soil. *J. AOAC Int.* **2012**, *95(5)*, 1258–1271.
21. Yifan Wang, Y.; Shen, L.; Gong, Z.; Pan, J.; Zheng, X.; Xue, J. Analytical methods to analyze pesticides and herbicides. *Water Environ. Res.* **2019**, *91(10)*, 1009–1024.
22. Online available: <http://www.epa.gov>.
23. Lan, P.T.N.; Hong, P.T.; Toan, V.D.; Lan, N.T.P. Textbook of soil pollution and treatment measures. Bach Khoa Publishing House. 2023.
24. Online available: <http://khuyennong.lamdong.gov.vn/ky-thuat-trong-trot/ki-thuat-trong-cay2/302-quy-trinh-k-thu-t-can-h-tac-cay-ca-phe-che>
25. Tahir, N.M.; Soon, K.H.; Ariffin, M.M.; Suratman, S. Chlorpyrifos and Malathion residues in Soils of a Terengganu golf course: a case study. *Malaysian J. Anal. Sci.* **2010**, *14(2)*, 82–87.

Table of content

- 1** Kim, T.T.; Diem, P.T.M.; Huy, N.D.Q.; Tai, P.A.; Phung, N.K.; Phung, N.K.; Bay, N.T. A riverbank failure model: A case study for the segment of Tien River flowing through Sadec, Vietnam. *J. Hydro-Meteorol.* **2023**, *16*, 1–22.
- 23** Duong, N.H.; Huyen, N.T.; Son, P.V.; Viet, T.T.; Ha, N.D. Proposed procedure of survey and model application for forecasting flow landslide susceptibility and hazards – A case study in Tam Chung commune, Thanh Hoa Province. *J. Hydro-Meteorol.* **2023**, *16*, 23–37.
- 38** Kim, T.T.; Huy, D.N.; Huy, N.D.Q.; Phuoc, N.V.; Phung, N.K.; Bay, N.T. The barotropic simulation of coastal current in Soc Trang derived from a hydraulic model in curvilinear coordinates. *J. Hydro-Meteorol.* **2023**, *16*, 38–55.
- 56** Lang, T.T.; Tan, L.V.; Tu, T.T.K.; Tuan, N.V. Evaluation of the current status of wastewater management and treatment from super-intensive whiteleg (*Penaeus vannamei*) shrimp ponds in Ben Tre Province. *J. Hydro-Meteorol.* **2023**, *16*, 56–64.
- 65** Phong, D.H. Flood risk assessment from high tide based on principal component analysis (PCA) of Sentinel-1 satellite images sequence for Ho Chi Minh City. *J. Hydro-Meteorol.* **2023**, *16*, 65–76.
- 77** Khanh, N.T.; Tuan, N.H.; Nu, H.T.T.; Van, C.T. Application of 2D hydro-dynamic model to simulate the suspended sediment on the Tien river, Cao Lanh district, Dong Thap Province. *J. Hydro-Meteorol.* **2023**, *16*, 77–88.
- 89** Thao, N.T.P.; Minh, T.P.; Anh, M.D. Assessment of current water quality status in clam areas in Thai Binh Province and proposal for measures to improve efficiency. *J. Hydro-Meteorol.* **2023**, *16*, 89–99.
- 100** Lam, D.V.; Toan, V.D.; Phuong, T.M. Residual and ecological risk assessment of Chlorpyrifos in coffee growing soil areas: A case study in Lam Ha district, Lam Dong Province. *J. Hydro-Meteorol.* **2023**, *16*, 100–108.